THE UNIVERSITY OF
WARWICK

TOWARDS THE NANOSCALE:
ELECTROCATALYSTS AND THEIR SUPPORTS

HOLLIE VICTORIA PATTEN

A thesis submitted for the degree of Doctor of Philosophy

Department of Chemistry

September 2011

TABLE OF CONTENTS

LIST OF FIGURES

LIST OF TABLES

ACKNOWLEDGEMENTS

First and foremost thank you to my supervisors Prof. Pat Unwin and Prof. Julie Macpherson, for giving me this opportunity. Thank you for your encouragement, enthusiasm and your immense amount of knowledge which has enabled this project to move forward. Thank you to Dr. Andy Wain and his colleagues at the National Physical Laboratory for funding this project and giving me an insight into the world outside of academia.

Thank you to all members of the Electrochemistry and Interfaces Group, both past and present for helping to make this a great experience. A special thank you to Dr. Stanley Lai for your support, particularly throughout the writing of this thesis.

Dr. Laura Hutton. You are an amazing friend. I have thoroughly enjoyed all of the times we have spent together, and I'm sure there will be many more. Thank you for everything.

Finally, a huge thank you to my friends, Jonathan and my family, Mum, Dad, Katie and Alisha-Mai. Thank you for all of your patience, encouragement and continued support, it is very much appreciated. Mum and Dad, I cannot thank you enough for everything that you have done for me, without you both I could not have come this far. Thank you!

DECLARATION

The work contained within this thesis is entirely original and my own work, except where acknowledged. I confirm that this thesis has not been submitted for a degree at another university. The micro-Raman mapping in Chapter 4 was carried out in conjunction with James Iacobini. The simulations in Chapter 4 and Chapter 5 were created and ran by Katherine E. Meadows and Dr. Michael Snowden, respectively. SECCM employed in Chapter 5 was performed in conjunction with Dr. Stanley Lai.

Part of this thesis has been published as detailed below:

Hollie V. Patten, Edgar Ventosa, Alvaro Colina, Virginia Ruiz, Jesús López-Palacios, Andrew J. Wain, Stanley C. S. Lai, Julie V. Macpherson and Patrick R. Unwin, *Influence of Ultrathin Poly-(3,4-Ethylenedioxythiophene) (PEDOT) Film Supports on the Electrodeposition and Electrocatalytic Activity of Discrete Platinum Nanoparticles J. Solid State Electrochemistry* DOI: 10.1007/s10008-011-1446-0

Additional articles comprising of work from this thesis are in preparation as detailed below:

Hollie V. Patten, Katherine E. Meadows, James G. Iacobini, Dario Battistel, Kim M. McKelvey, Mark E. Newton, Julie V Macpherson, Patrick R. Unwin, *Quantitative Determination of the Electron Transfer Activity of polycrystalline Boron Doped Diamond using Intermittent Contact - Scanning Electrochemical Microscopy (IC-SECM)*

Hollie V. Patten, Stanley C. S. Lai, Michael E, Snowden, Mark E. Newton Julie V. Macpherson, Patrick R. Unwin, *Scanning Electrochemical Cell Microscopy (SECCM): Application to Electrochemical Processes at polycrystalline Boron Doped Diamond (pBDD)*

Hollie V. Patten, Stanley C. S. Lai, Andrew J. Wain, Julie V. Macpherson, Patrick R. Unwin Polycrystalline Boron Doped Diamond (pBDD) Rotating Disk Electrode (RDE):Fabrication, Characterisation and Functionalisation

ABSTRACT

Electrocatalysts and their support materials used for fuel cell (FC) technology remain at the forefront of research in this field. Typically FC electrocatalysts are comprised of Pt nanoparticles (NPs) supported by carbon. Improvement of both the efficiency and the durability of the materials is required to increase the overall FC performance. To achieve these goals requires a fundamental understanding of electrocatalysis at composite materials and the exploration of alternative materials. These aspects are explored in this thesis. Highly oriented pyrolytic graphite (HOPG) and poly-(3,4-ethylenedioxythiophene) PEDOT-coated HOPG were used as support materials for the electrodeposition of Pt NPs. The NPs were characterised using atomic force microscopy (AFM) which showed that by applying an ultra-thin layer (*ca.* 2 nm) of PEDOT, a conducting polymer (CP), onto HOPG, there was less tendency for NP aggregation, with no preferential deposition, i.e. at step edges, and also smaller particles were formed. PEDOT-coated HOPG as the support material for Pt NPs showed a significant enhancement of electroactivity for methanol oxidation, by an order of magnitude, compared with similarly prepared NPs on native HOPG. An alternative support material; explored in this thesis, was polycrystalline boron doped diamond (pBDD), owing to its stability in harsh environments, analogous to FCs. During growth, boron uptake varies across the exposed surface of pBDD, leading to a heterogeneous substrate with typical grain sizes of 5-40 μm. Two new scanned probed techniques; intermittent contact - scanning electrochemical microscopy (IC-SECM) and scanning electrochemical cell microscopy (SECCM) were employed to investigate the impact of this heterogeneity on the local electrochemical properties. Maps using IC-SECM revealed that the entire surface was active, but that areas with higher boron concentration were more electroactive. Grain boundaries showed no enhanced activity. The maps were successfully correlated to the boron dopant density using micro-Raman mapping and field emission scanning electron microscopy (FE-SEM). Similarly, SECCM maps also proved that the entire surface is electrochemically active with the heterogeneities relating to boron content. For data obtained by both techniques finite element simulations (FEM) were employed to extract values for the standard rate constant, k^0. With knowledge of the fundamental properties of pBDD, the successful fabrication of a pBDD rotating disk electrode (RDE) is reported which is fully characterised. By functionalisation of pBDD with Pt NPs, the oxygen reduction reaction (ORR) has been studied and compared with a bulk Pt RDE. These preliminary studies show potential for gaining insight into the kinetics of the ORR.

ABBREVIATIONS

AFC	alkaline fuel cell
AFM	atomic force microscopy
CE	counter electrode
CHP	co-generation of heat and power
CP	conducting polymer
CV	cyclic voltammetry
CVD	chemical vapour deposition
ET	electron transfer
FC	fuel cell
FEM	finite element model
FE-SEM	field emission-scanning electron microscopy
GDL	gas diffusion layer
HER	hydrogen evolution reaction
HOPG	highly oriented pyrolytic graphite
HPHT	high pressure high temperature
IC-SECM	intermittent contact - scanning electrochemical microscopy
LSV	linear sweep voltammetry
MCFC	molten carbonate fuel cell
MWCVD	microwave plasma chemical vapour deposition
NP	nanoparticle
ORR	oxygen reduction reaction
pBDD	polycrystalline boron doped diamond
PEMFC	proton exchange membrane fuel cell
PVD	physical vapour deposition
QRE	quasi-reference electrode

RDE	rotating disk electrode
RE	reference electrode
SCE	saturated calomel electrode
SECCM	scanning electrochemical cell microscopy
SECM	scanning electrochemical microscopy
SECM-AFM	combined SECM with atomic force microscopy
SG-TC	substrate generation - tip collection
SICM	scanning ion conductance microscopy
SIMS	secondary ion mass spectrometry
SMCM	scanning miropipette contact method
SOFC	solid oxide fuel cell
SPIP	scanning probe imaging processor
TEM	transmission electron microscopy
TM-AFM	tapping mode atomic force microscopy
UME	ultramicroelectrode
WE	working electrode

GLOSSARY OF TERMS

A	electrode area
c_i, c*	concentration
D_i or D	diffusion coefficient
E	potential
$E^{0'}$	standard electrode potential
F	Faraday's constant
i_{AC}	alternating current
i_{DC}	mean conductance current
i_L	levich current
i_{lim}	limiting current
ip	peak current
k^0	standard rate constant
k_b	heterogeneous rate constant for reduction
k_{exc}	self exchange rate constant
k_f	heterogeneous rate constant for oxidation
m_h	meniscus height
m_w	mensicus contact diameter
n	number of electrons
$\mathbf{n}.N_m$	flux
R	gas constant
r_p	inner radius
T	temperature
t_w	central segment thickness
u_i	ionic mobility

V	electric field
v	scan rate
z_i	charge of species
α	transfer coefficient
ΔE_p	peak to peak separation
η	overpotential
θ	semi-angle
ν	kinematic viscosity
ω	angular rotation speed

CHAPTER 1

INTRODUCTION

ABSTRACT

This thesis is concerned with the fabrication and analysis of metal nanoparticles on various support materials to elucidate electrocatalytic processes, primarily associated with fuel cells, ultimately with high spatial resolution. This Chapter provides rationale for this work covering; an overview of fuel cells with focus on the proton exchange membrane fuel cell and its related issues, exploring the materials used in this thesis as electrocatalyst support materials and high resolution electrochemical imaging techniques available. Finally, a brief outline of the project aims is given.

1.1 Fuel Cells

A decline in the availability of fossil fuels has lead to the development of alternative means of energy. One of these alternatives is the use of fuel cells (FCs) which directly convert chemical energy into electrical energy. The use of FCs was first demonstrated in the 1830's when William Grove passed hydrogen and oxygen gas over a platinum catalyst to generate an electrical current.[1] There are a number of types of FCs including solid oxide, alkaline, molten carbonate, phosphoric acid, direct methanol and the proton exchange membrane fuel cell (PEMFC).[2-17]

The alkaline fuel cell (AFC)[2,3] is extremely susceptible to contamination due to progressive carbonation of the electrolyte unless the highest purity gases are employed. The solid oxide fuel cell (SOFC)[4-6] and molten carbonate fuel cell (MCFC)[17] both require high operating temperatures, typically 500 °C being the lowest.[18] However, these high operating temperatures do offer an additional advantage that steam can be channelled into turbines. This creates the co-generation of heat and power (CHP), making these likely candidates for large-scale energy production, and unsuitable for mobile applications. The direct methanol fuel cell (DMFC)[13-16] requires a large amount of Pt to catalyse the reaction but does operate at much lower temperatures (60°C - 80°C) based on the proton exchange membrane fuel cell (PEMFC) which also operates at lower temperature ranges.[7-11] Hydrogen-based fuel cells are an extremely attractive method for producing electrical energy particularly as the main reaction product is water. They are the most likely cell to become widely used, particularly in the transportation industry; however there are still many developments needed

through research to increase the efficiency and durability, as well as issues in hydrogen production and storage.[18] Electrocatalytic processes in the PEMFC were the main focus of this work and this type of cell is considered further in the next section.

1.2 Proton Exchange Membrane Fuel Cells (PEMFCs)

The PEMFC was initially developed by General Electric in the 1960's by Thomas Grubb and Leonard Neidrach.[19] This technology was utilised by NASA on some of the first manned space missions such as the Gemini program.[20] However due to technical issues the space missions began to use batteries which delayed the development of PEMFC technology until around ten years later when the oil crisis led to a renewed interest into alternative energy sources research. Ballard Power Systems then began the rapid development which showed promising result for use on a commercial basis.[21]

The PEMFC is made up of a variety of components, to enable chemical energy to be turned into electrical energy, the most important of which are the anode, cathode and a proton conducting membrane (Figure 1.1). This section will describe each of these components and their role in the PEMFC.

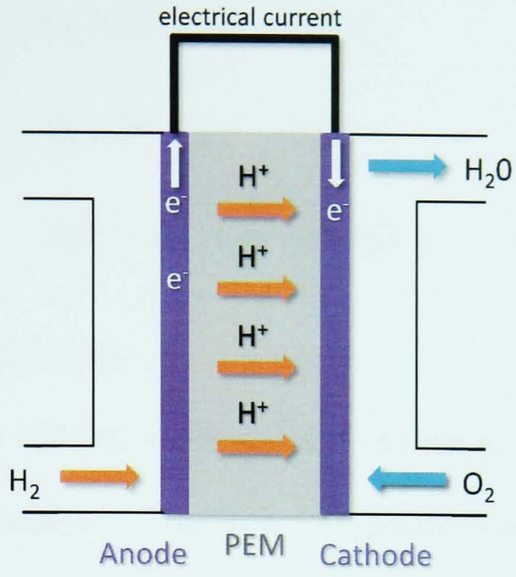

Figure 1.1: A schematic representation of a working PEMFC

Hydrogen gas is let into the FC and is driven through the gas diffusion layer (GDL) towards the anode. Here, the hydrogen becomes adsorbed onto the electrocatalyst, where it is split into protons and electrons (Equation 1.1).

$$H_2 \rightarrow 2H^+ + 2e^- \qquad (1.1)$$

A proton conducting membrane allows the protons to pass through whilst the electrons are forced via an external circuit. At the cathode (situated on the other side of the proton conducting membrane) the protons that have travelled through the membrane and the electrons from the external circuit are recombined with oxygen (brought into the FC via air). The oxygen reduction reaction can proceed via a four electron transfer process, where water is formed (Equation 1.2), or indirectly via a two electron transfer process, where hydrogen peroxide is formed (Equation 1.3), which can reduce further to water (Equation 1.4).

$$O_2 + 4H^+ + 4e^- \rightarrow 2H_2O \quad (1.2)$$

$$O_2 + 2H^+ + 2e^- \rightarrow H_2O_2 \quad (1.3)$$

$$H_2O_2 + 2H^+ + 2e^- \rightarrow 2H_2O \quad (1.4)$$

GAS DIFFUSION LAYER (GDL)

The gases used in the PEMFC are forced through the gas diffusion layer (GDL) before reaching the catalyst. The GDL is typically made of carbon paper or woven cloth, which are hydrophilic, and so are treated with hydrophobic Teflon (see Figure 1.2). Having a mixture of hydrophobic and hydrophilic materials is essential for effective water management.[22] Enough water needs to be removed from the gas to prevent flooding, while some water should remain for conductivity.[23] Flooding would lead to a build up of water at the cathode hence blocking electrochemical activity.[24] However, if too much water was removed at this stage there will not be enough present in the system to ionise the groups in the electrolyte, preventing protons from flowing. Achieving the balance between hydrophilicity and hydrophobicity is crucial in providing a suitable GDL.[23,24]

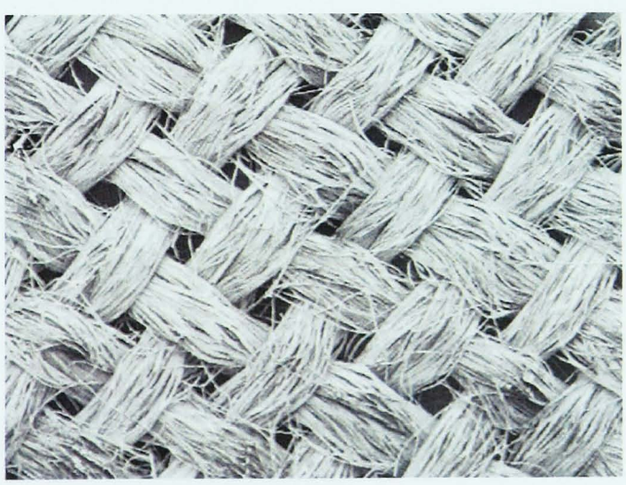

Figure 1.2 Scanning electron micrograph of a gas diffusion layer (GDL) showing Teflon treated carbon cloth[25]

MEMBRANE

The membrane in a PEMFC is used as a solid electrolyte, which is able to conduct ions (protons) between the electrodes but is electronically insulating to prevent short-circuiting within the fuel cell. Furthermore, the membrane should prevent cross-over of reactant species, as this would directly impact the cell efficiency. Nafion™ (sulphonated tetrafluoroethylene copolymer), a derivative of PTFE developed by DuPont, is the most common membrane used in a PEMFC (structure shown in Figure 1.3). Nafion™ is a cation exchange membrane, where the PTFE is the hydrophobic backbone and the sulphonic acid side chains are hydrophilic. When the side chains are hydrated the membrane can conduct protons while remaining electronically insulating, due to the repelling nature towards electrons.

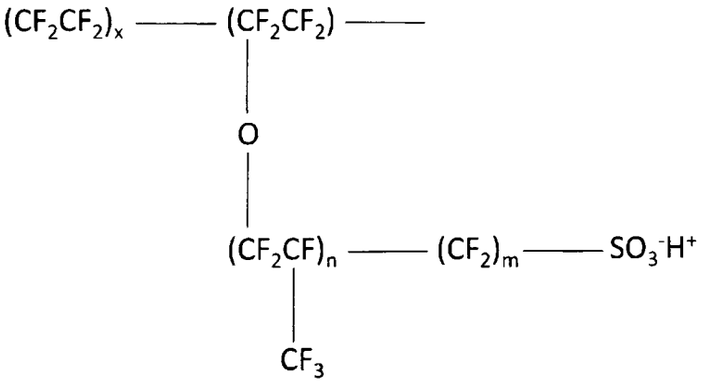

Figure 1.3 Structure of Nafion® adapted from Ref. 20

1.2.1 ELECTROCATALYSTS AND THEIR SUPPORT MATERIALS

Ever since PEMFCs have been used to create power, much research and development has been carried out on the electrocatalyst and their support materials. This aspect is the main focus of this thesis. The most commonly used

support material and catalyst for both the anode and the cathode is carbon decorated with Pt nanoparticles. However, a number of issues remain with regard to employing these materials in the FC, such as catalyst degradation, corrosion of the carbon support, flooding of the catalyst material, as a result of reactions occurring there, and poisoning of the catalyst.[11,26-30] Also, research continues to investigate low loading of the catalyst to achieve cost effectiveness.[31-33]

Employing carbon as a support material does have some disadvantages due to the FC presenting a highly corrosive environment. The carbon is exposed to relatively high temperatures, high potentials, low pH, areas with a high oxygen content, as well as a high water content.[34] Some of these conditions result in carbon oxidation catalysed by the electrocatalyst and hence corrosion[34-36] (Equations 1.5 and 1.6).

$$C + H_2O \rightarrow CO_2 + 2H^+ + 2e^- \quad (1.5)$$

$$C + H_2O \rightarrow H_2 + CO \quad (1.6)$$

Carbon oxidation can occur at potentials more positive than 0.2 V, much lower than potentials in the FC environment, especially at the cathode.[37] Pt itself, when employed as the electrocatalyst, is known to contribute to carbon corrosion.[35,38,39] Consequently, localised corrosion could lead to dislodging of catalyst particles, causing a loss of electrical contact and decrease in the amount of active catalyst.[40] Typically, carbon black is used for the catalyst support, decorated with precious metal catalyst which, theoretically, ensures a high surface area of catalyst without power loss, keeping FCs cost effective. Carbon black supports such as Vulcan XC72 (manufactured by Cobat) is produced by heating carbon in

an inert, oxygen-free, atmosphere[41]. This produces a high surface area with spherical particles (<50 nm in diameter). The carbon black can be further treated chemically or with steam to produce a microstructure (*ca.* 20-30 μm in diameter) containing pores which are ideal for catalyst deposition.[41] Figure 1.4 shows a transmission electron micrograph (TEM) image of Vulcan XC-72 decorated with Pt NPs.

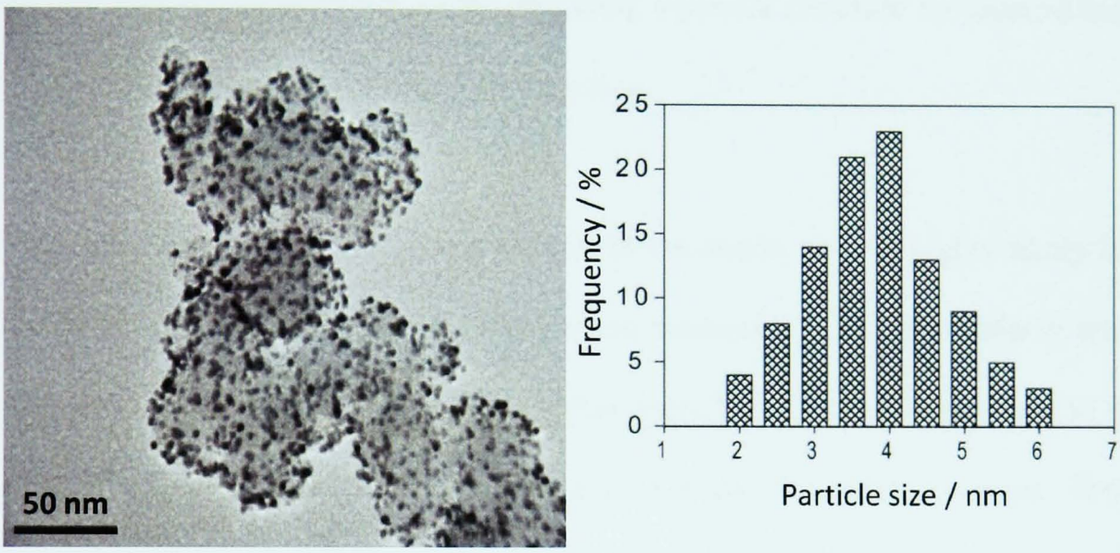

Figure 1.4 TEM of Vulcan XC-72 decorated with Pt nanoparticles with a histogram to show the size distribution. Image taken and adapted from Ref. 42

The catalyst support materials employed in this thesis are both allotropes of carbon: highly oriented pyrolytic graphite (HOPG); and polycrystalline boron doped diamond (pBDD). Both HOPG and pBDD have advantageous properties when employed as carbon supports for studying electrocatalysis. The properties and use of these materials as electrodes are explored further in Section 1.3 and Section 1.4.

The literature provides a vast array of other forms of carbon that have been employed as fuel cell electrocatalyst supports, including nitrogen modified carbon,[43] carbon nanotubes,[44] tungsten carbide[45] and carbon nanohorns.[46] All of these materials strive to achieve the same overall result, namely higher electroactivity over prolonged periods using minimal amounts of Pt. This can be by means of the nanoparticles adhering better, susceptible to less corrosion, promoting the formation of smaller nanoparticles and hence a larger catalytic surface area to volume ratio, or by providing a porous structure for nanoparticles to be evenly spread and avoiding aggregation.

Fuel cell efficiency may be compromised at the anode, as it is highly likely that the hydrogen gas will contain some carbon monoxide (CO), particularly when this is produced by the reforming of other fuels.[47] CO adsorbs strongly to the surface of the Pt nanoparticles, blocking sites for the HOR to occur, hence poisoning the catalyst.[48,49] At the cathode, where the oxygen reduction reaction (ORR) occurs there are two main issues to address. Firstly, if the ORR produces water (Equation 1.2) (the desired product) this has to be effectively removed to prevent flooding. However, depending on the reaction conditions, the ORR could lead to the formation of hydrogen peroxide through a two-electron process (Equation 1.3). This does not directly decrease the fuel cell efficiency (2 electrons rather than 4), but H_2O_2 is also a strong oxidiser and can lead to membrane and support corrosion.

Mainly as a result of catalyst poisoning effects, many researchers have focused their efforts around the investigation of Pt-based alloys for the precious metal at the anode. Many alloy materials have been employed in research including Ru,

Ni, Fe, V, Mo and Co to name a few.[50-53] Pt-Ru remains the most promising of the alloys. Alloys are thought to enhance the CO tolerance by two different mechanisms: a bi-functional mechanism and an electronic effect.[52,54] The bi-functional mechanism works by a surface reaction occurring between the CO adsorbed on the Pt and oxygenated species produced from the neighbouring alloy oxide. The electronic effect arises from an energy shift of the Pt electronic states which produces weakening of the platinum and CO interaction.[52,54] When employing Pt alloys at the cathode, the enhancement towards the reduction of oxygen has been attributed to surface roughening when employing Cr as the alloy[55] or from the shortening of the interatomic distance between Pt-Pt.[56,57]

In addition to employing alloys as an avenue to prevent or reduce catalyst poisoning, many researchers have started to use nanoparticles coated with conducting polymer materials which have been shown to enhance the electroactivity compared with native Pt.[58,59] Conducting polymers (CPs) employed include polyaniline and poly-(3,4-ethylenedioxythiophene) (PEDOT).[44,60-63] CPs have been shown to not only improve the adherence of nanoparticles to the support but also impart synergetic effects.[64,65]

1.3 Highly Oriented Pyrolytic Graphite (HOPG)

Graphite is amongst the common allotropes of carbon and it is particularly useful as an electrode material due to its high electrical conductivity and other unique properties, including its lamellar structure.

1.3.1 STRUCTURE

Kish graphite was first used an electrode before highly oriented pyrolytic graphite (HOPG). It was produced as a by-product of the steel making process.[66] However, graphite obtained in this process contained many impurities and it was difficult to produce a thickness of over a mm. Therefore, was not practical for use on many applications. Consequently, HOPG became preferable as an electrode material, discussed further in Section 1.3.2. This form of graphite has a lamellar structure, where the forces are much stronger within the lateral plane (sp^2 carbon), where covalent bonding exists, than between the planes, held together by Van der Waals forces (Figure 1.5a). An alternative feature of HOPG is that a fresh and renewable surface can be easily obtained by cleaving the top layers from the bulk material. The surface of HOPG consists mainly of a basal plane (the area where there are no step edges), interspersed by edge planes (where step edges are present), as shown schematically in Figure 1.5b.

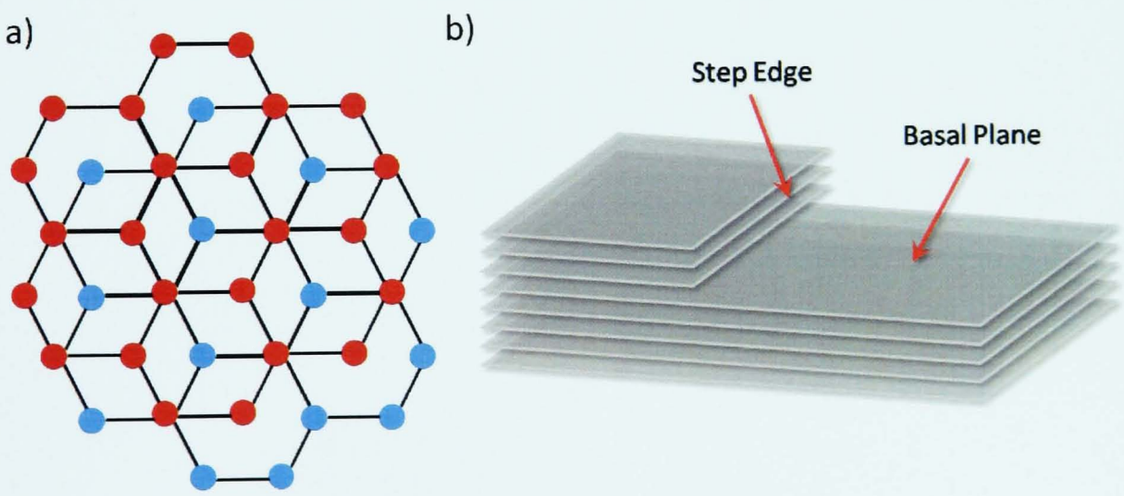

Figure 1.5: Schematics to show a) arrangement of carbon atoms on HOPG (•) represents the lower layer and (•) represents the upper layers and b) the structure of HOPG with both the basal and edge plane

There are a variety of HOPG grades commercially available to purchase including ZYA, SPI-1 and SPI-2 (Aztech Trading, UK, on behalf of SPI Supplies). These gradings of HOPG possess different properties including varied sizes of polycrystals (10 mm for the highest quality), different surface roughness (0.2-0.3 nm and steps of several to dozens of atomic layers) and a range of step densities, which is also dependent on the cleavage method.[67] Figure 1.6 demonstrates the typical range of step densities for the various grades of HOPG, showing tapping mode atomic force microscopy (TM-AFM) images.[68]. In general, the higher the quality of HOPG, ZYA being the highest, the larger the polycrystals, which results in a decrease in roughness and step density.[69] An exception is ZYH material, which appears rough to the eye, but shows a lower step density than, say, SPI-1 grade.[68]

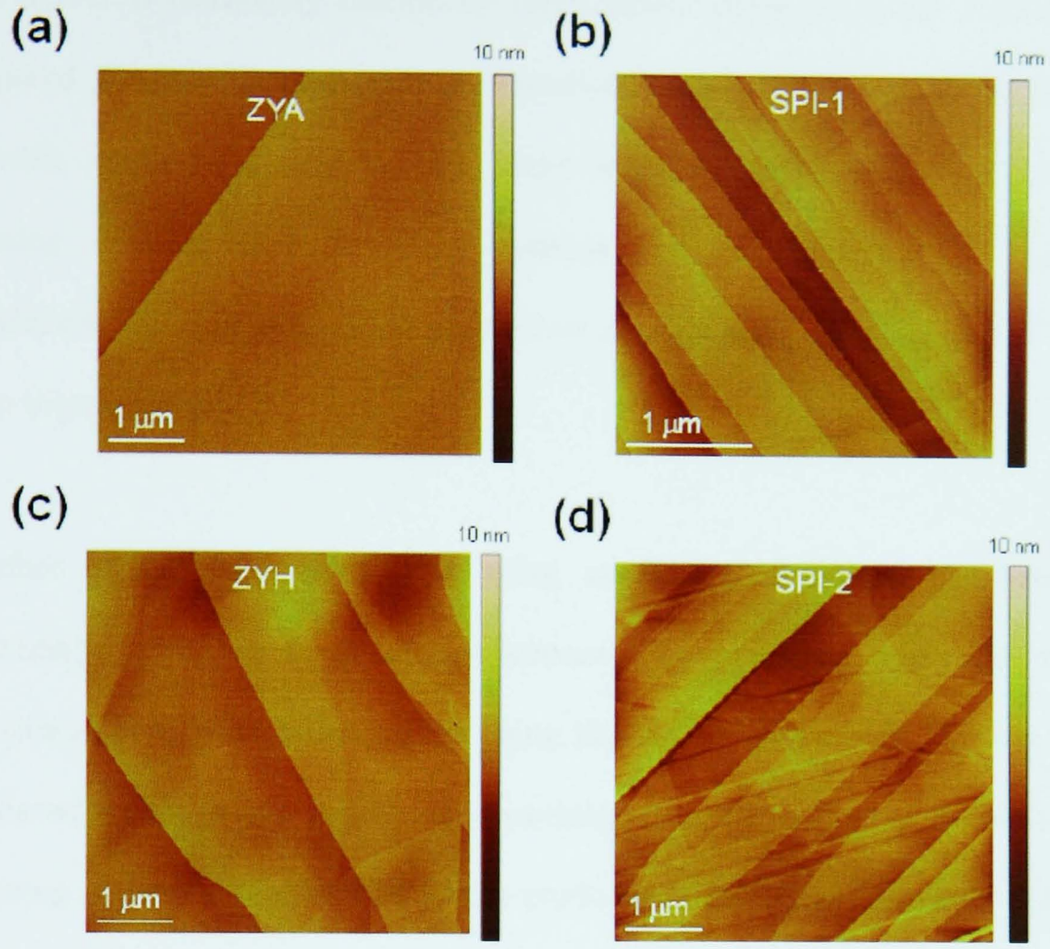

Figure 1.6 Tapping mode atomic force microscopy images (TM-AFM) images of the different grades of freshly cleaved HOPG a) ZYA b) SPI-1 c) ZYH d) SPI-1[268]

1.3.2 As an Electrode Material

The first synthetic graphite was reported by E. A. Acheson in 1891, made by carborundum or silicon carbide. However, it was not until the 1960's that graphite was actually used extensively as an electrode material. In comparison to other carbon materials, such as glassy carbon, HOPG provides a well defined surface to work with. HOPG conducts electrons across the plane (sp^2 bonded carbon) by electron movement through the conjugated π-system, while conductance between planes occurs through electron tunnelling. This means the conductivity is direction dependent.

As HOPG is reasonably chemically inert, functionalisation of the material is required for several applications. Functionalisation can be optimised for a specific application, allowing for many widespread applications, including sensing devices, electroanalytical systems and electrocatalysis.[70-74] Likely candidates for functionalisation are various nanoparticles,[75-78] polymers[79,80] and also biomolecules.[81,82]

Surface modification of HOPG using conducting polymers has become extremely promising for many applications. For example, micro and nano structures have been formed when using HOPG and polypyrrole.[83] This was achieved by using the HOPG as a working electrode and as a template for forming hydrogen nanobubbles before producing a polypyrrole nonporous film. This study also demonstrates the ability to easily control the size of the templates and hence the size of the CP HOPG structures formed. Other conducting polymers have been used in combination with HOPG for fuel cell applications, explored in more detail in Section 1.3.3.

A further use of HOPG is for intercalation, a process where for this form of graphite, an ion or molecule may be inserted between the layers. A particular application explored in literature is utilising HOPG as the anode in lithium ion batteries. [84,85] HOPG can be employed because of its relatively low cost, good potential cycling ability and also because it has the ability to produce very high currents.[86] The role of the HOPG is to store the lithium ions, however degradation of the material may occur where the basal plane develops fine cracks and blisters, observed using *in situ* AFM.[87] Perchloric acid has also been demonstrated as a good intercalating species[88] and the mechanism of this

intercalation or insertion was elucidated using electrochemical AFM, where a quantitative estimate of the interlayer spacing was found.[89] Although intercalation may be useful, in some cases the intercalation compounds initially formed will oxidise the carbon to form graphite oxides,[90,91] demonstrated by Raman spectroscopy which showed lattice damage as a consequence.[92]

Although HOPG has been used as an electrode material for many years, there are still many conflicting arguments relating to the electroactive sites i.e. what is the relative electrochemical activity on the basal plane or the edge plane? Many studies have been conducted reporting that the basal plane possesses slow electron transfer kinetics (or that it is completely inert) compared with the edge plane for classical outer and inner sphere electron transfer mediators[93,94] with many of these studies using cyclic voltammetry[95-99] (macro scale electrochemistry) which would probe both the basal and edge plane of the HOPG simultaneously. The standard rate constant, k^0, has previously been reported[100] as 1 x 10^{-9} cm s^{-1} at the basal plane and a much larger k^0 of 0.022 cm s^{-1} at the edge plane of HOPG.[100] To fully elucidate the rate of electron transfer at each site on the HOPG, electrochemistry at higher resolution has provided new arguments. Using electrochemical imaging techniques such as the scanning micropipette contact method (SMCM)[101] or the combined technique scanning electrochemical microscopy-atomic force microscopy (SECM-AFM),[102] allows for localised regions of the sample to be investigated. Many of these studies provide evidence that both the basal[101] and the edge plane are active but with slightly enhanced activity at the edge plane.[102] Enhanced activity at step edges provides an explanation for the preferential deposition of nanoparticles at step

sites.[72,103,104] However, co-ordination and nucleus stabilisation effects are naturally more important at step edges.

1.3.3 Electrocatalyst Support Materials

HOPG can be employed as the carbon support material for electrocatalyst investigations. Nanoparticles of precious metal can be deposited onto the substrate before performing electrochemical measurements. Both particle size effects[74,105-108] and subsequent morphology[109,110] play a role in electrocatalysis. Pt nanoparticles can be electrodeposited,[76,78] chemically deposited[74] or preformed particles can be used.[70] These methods of deposition can produce narrow size distributions,[74] excellent for fundamental electrocatalyst characterisation, or sometimes the deposition procedure will result in nanoparticle aggregation. Aggregation of particles will inevitably lead to a loss in surface area, hence a loss of sites for electrocatalysis to occur.

Pt electrocatalysts have been dispersed on HOPG and scanning electrochemical microscopy (SECM) employed to determine the activity of particle clusters towards the hydrogen evolution reaction (HER). However, from this study, higher resolution imaging of the electroactivity should be sought to fully investigate the electroactivity of particles.[111]

As mentioned above Pt alloys have become a favourable catalyst as they reduce poisoning effects for a number of electrochemical reactions. Studies have reported sequential electrodeposition to prepare PtMo and PtRuMo particles onto activated carbon (preventing preferential deposition at the step edges) to

investigate methanol oxidation. An enhanced activity was seen for the PtRuMo compared with the PtRu or Pt alone.[112] Higher activity and durability towards methanol oxidation was also observed by nitrogen doping HOPG modified with Pt nanoparticles.[43,113] In addition to the electrocatalytic enhancement, Pt nanoparticles deposited were observed to be smaller in diameter and more disperse due to this nitrogen doping,[43,113] and consequently the particle sizes may have been the cause for electrocatalytic enhancement. One further study that observed an enhancement towards methanol oxidation served to demonstrate the advantages of employing HOPG modified with PtRu alloy.[73]

Conducting polymers, including poly(3,4-ethylenedioxythiophene) (PEDOT) have been electrodeposited onto HOPG.[80] This procedure usually takes place from organic solvents, but electrodeposition from an aqueous solution results in a PEDOT film without contaminants present. With conditions optimised, molecularly thin films can be produced (*ca.* 2 nm in height).[80] These films can then form a support for metal nanoparticle deposition.

Melanin, complex biopolymers, existing in living organisms, can be deposited onto HOPG forming films which are able to trap Fe complexes and other metallic cations by simple immersion. When Fe is trapped by the Melanin it becomes electrocatalytically active for the hydrogen peroxide electroreduction.[114]

1.4 Polycrystalline Boron Doped Diamond (pBDD)

1.4.1 Structure

Diamond is an allotrope of carbon where the atoms are arranged tetrahedrally forming a face centred cubic lattice (Figure 1.7a). It is well known that intrinsic (undoped) diamond is an electrical insulator; however certain forms of doping can cause the material to conduct, thus enabling its use as an electrode material.

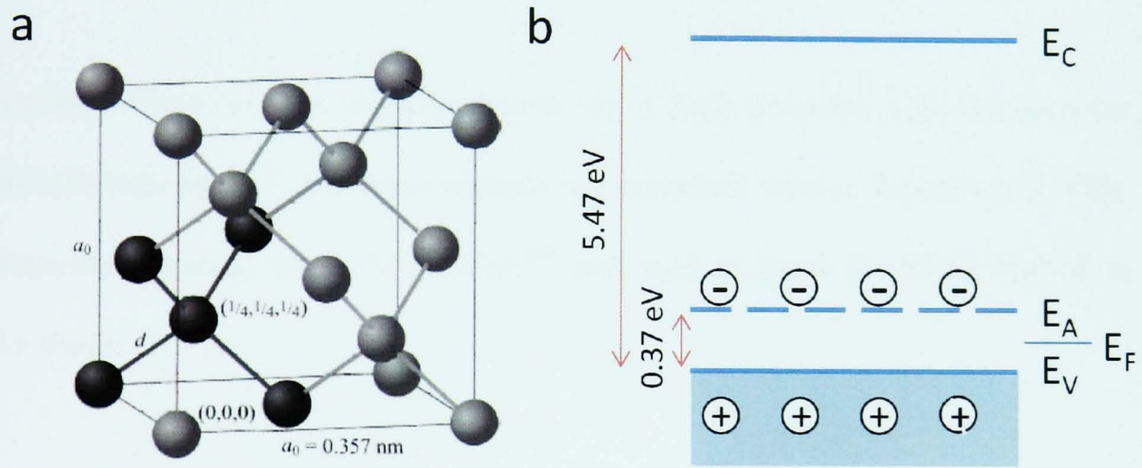

Figure 1.7 a) Image representing the carbon atom arrangement in diamond b) Schematic diagram of the energy levels of a p-type semiconductor. E_C, E_V, E_A and E_F represent the conduction band, valence band, acceptor level and fermi level respectively (not drawn to scale)

Undoped diamond is a wide bandgap semiconductor with a gap of 5.47 eV at 300 K[115] however by doping this with an n-type dopant, where the charge carriers are electrons, or p-type dopant, where the charge carriers are holes, the diamond can become electrically conducting. Typical n-type and p-type dopants are nitrogen and boron respectively. The research in this thesis is concerned with boron doped diamond and therefore the focus throughout the rest of this section will be concerned with this material. The addition of boron into the crystal lattice

creates an acceptor level 0.37 eV above the valence band,[116] schematically presented in Figure 1.7b. Electrons can be promoted from the valence band to the acceptor level leaving a positive-charge behind, referred to as holes, which are considered as mobile.[117] As the concentration of boron is increased, this acceptor level becomes a band which thickens towards the valence band. As the boron concentration is increased from 5 x 10^{16} to 8 x 10^{20} cm^{-3}, different conduction mechanisms arise in the form of valence band conduction, hopping conduction and metallic conduction (which is further discussed in Chapter 4).[118]

Synthetic diamond was initially grown via a high pressure high temperature (HPHT) technique[119] and more recently via chemical vapour deposition (CVD). Microwave plasma CVD (MWCVD)[120] was used to grow the BDD studied in this thesis.

MWCVD has advantages over other methods, including high growth rates, enabled because of the high MW powers that can be employed. A further advantage is that 'clean' diamond can be produced, or diamond with low amounts of unintended impurities, such as amorphous carbon.[121] This high quality is of particular importance when employing diamond as an electrode material, as discussed in more detail in Section 1.4.2. Another advantage of using MWCVD is that the substrate, thereby can be negatively biased, causing carbon containing ions to accelerate towards the substrate increasing the nucleation rate and also allowing samples of a specific orientation to be prepared.

To create boron doped diamond a variety of gases are introduced during the growth process; including H_2, a carbon containing gas (to produce a methyl

radical) and a boron containing gas usually in the form of B_2H_6. In MWCVD the MW power is coupled into the chamber, usually via a quartz window, in order to create a discharge. This discharge couples energy into the gas phase electrons which, through collisions, transfers the energy to the surrounding gas molecules. This process eventually leads to diamond deposition on the plasma immersed substrate.[122] The substrate is held at a temperature above 700 ^{0}C to prevent amorphous carbon from forming during the growth process. One of the first MW-CVD reactors reported was the 'NIRIM-type' (Figure 1.8a) in the early 1980s[123] and in the late 1980s the 'ASTEX-type' (Figure 1.8) reactor was commercialised by Applied Science and Technology Ltd, where particularly high rates of growth were reported, in excess of 10 μm h^{-1}. The chemistry involved in growing synthetic diamond can be challenging especially to produce high quality diamond at fast growth rates. Therefore, research continues in this area to constantly strive for improved diamond quality and growth parameters.[124-126]

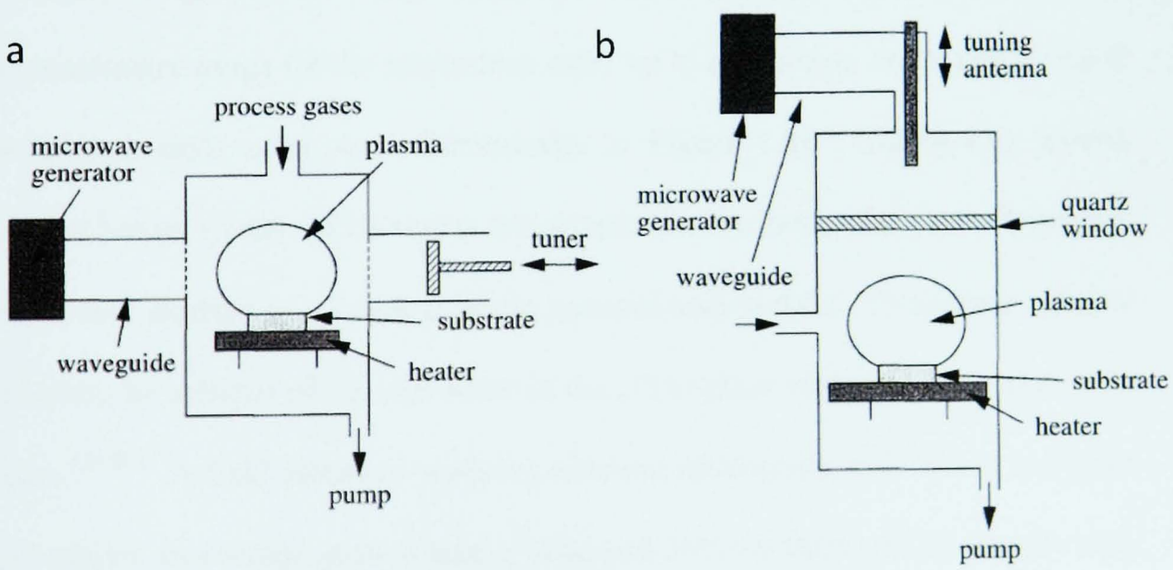

Figure 1.8 Schematic for a microwave plasma chemical vapour deposition (MW-CVD) reactor a) 'NIRIM-type' b) 'ASTEX-type'[122]

Boron is readily incorporated into the diamond lattice during the growth process, but to obtain polycrystalline boron doped diamond a non-diamond substrate is often used i.e Ti, Mo, W and Si. Polycrystalline material is obtained, where certain crystal orientations grow at different rates, eventually leading to a substrate where the grains are pushed together, with continuous growth in the upwards direction, forming a continuous layer of polycrystalline diamond.[127]

1.4.2 BDD AS AN ELECTRODE MATERIAL

Diamond was first used as an electrode material in 1983, in which Zn ions were implanted into natural diamond to make it conducting. The resulting electrode showed reduced background currents and a wider potential window than glassy carbon.[128] However, it wasn't until 1993 that pBDD was first reported as a possible electrode material.[129]

During CVD growth the sample becomes thicker and grain sizes increase from the nanometre range (at the nucleation side) up to the micron range (observed at the growth side) as shown schematically in Figure 1.9a. During this growth process boron uptake varies across the sample mainly due to the crystallographic plane, thus leading to a heterogeneous material and surface. Preferential uptake of boron, by a factor of 10, can occur in the (111) plane compared with the (100) plane.[130-132] A field emission scanning electron micrograph (FE-SEM) in Figure 1.9b shows an average growth side of a lapped 500 μm thick pBDD sample with grain sizes of 5-40 μm. The contrast can be related to conductivity. The dark areas are more conducting showing where more boron has been incorporated.

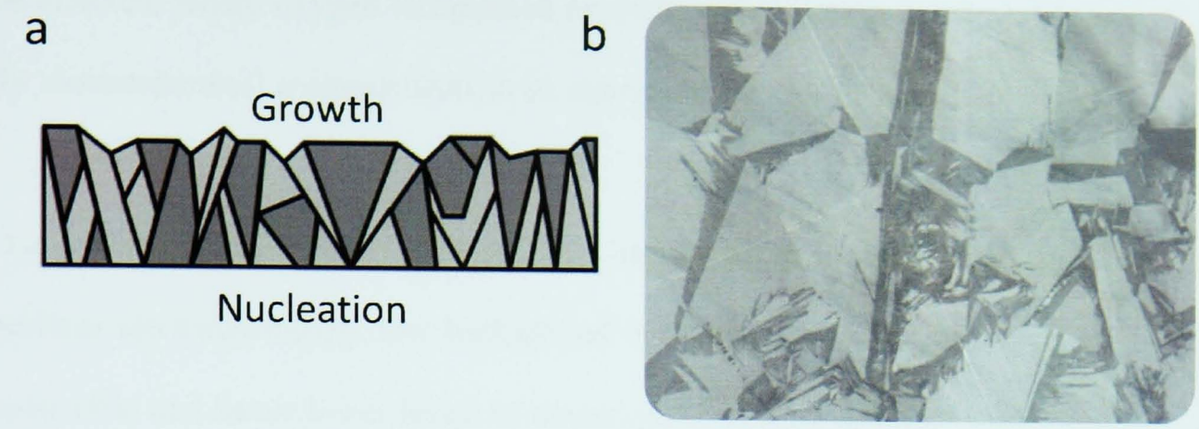

Figure 1.9 a) Schematic showing the side view of an as grown pBDD sample133 b) Field Emission Scanning Electron Micrograph (FE-SEM) showing a top view of a polished pBDD sample

A number of other factors must also be considered when using pBDD as an electrode, including: the thickness of the sample; size of the grain; the surface termination of the sample; and whether to work with a polished or unpolished substrate. The concentration of boron plays a major role in the observed electrochemistry of pBDD. As mentioned previously, when the concentration of boron is $\geq 3 \times 10^{20}$ atoms cm^{-3} the electrode will possess metal-like conductivity, giving metal-like electrochemical behaviour.[134]

Diamond grown via CVD has a hydrogen-terminated surface, however this may be modified to oxygen-terminated relatively easily using several different methods including oxygen plasma, anodic biasing and boiling the sample in acid. From an electrochemical viewpoint oxygen-termination has several advantages over hydrogen-termination. Hydrogen-termination has been shown to slowly oxidise in air over long periods of time,[135,136] as well as degrading when the substrate is anodically biased,[137] whereas oxygen terminated samples are much more stable under these conditions. Also, the hydrophobicity of the sample can

be affected, where oxygen termination provides a hydrophilic substrate[138] ideal for electrochemical measurements in an aqueous solution (for example).

Oxygen-terminated pBDD provides the basis for an excellent substrate to perform electrochemistry; low background currents give an improved signal to noise ratio and hence lower levels of detection, compared with a Pt electrode.[137] pBDD also has a wider potential window, allowing a wider range of reactions to be observed. The background currents and potential window are also an indication of the quality of diamond. For example, if sp^2 carbon has been incorporated during growth then larger background currents and a smaller potential range will be seen.[137] These impurities also impact the electron transfer kinetics.[139] A good indication of the quality of the diamond can be determined with Raman spectroscopy (see Chapter 2). The typical diamond peak (or zone centre optical phonon) is seen at 1332.5 cm^{-1} and when impurities, in particular graphitic or amorphous carbon, are present additional peaks are observed at *ca.* 1350-1580 cm^{-1}.[140,141]

pBDD electrodes can be made using thin films or with thicker samples (*ca.* 500 μm) which can be used as grown or lapped to create smooth surfaces. This is of particular importance if the electrode needs to be characterised with atomic force microscopy (AFM), for example. Thicker samples are more easily manipulated into a variety of electrochemical set-ups. For example, macro electrodes can be fabricated which have a well known geometry and therefore a well defined electrochemical response in a variety of redox media.[142] This also enables a direct comparison with other commercially available metallic electrodes.

The responses of many pBDD electrodes, with varying boron concentrations, have been tested in a range of simple outer and inner sphere redox couples.[143-146] In all investigations, closer to reversible behaviour was observed for heavily doped samples in the metallic region, compared with semiconducting diamond, when performing cyclic voltammetric (CV) experiments.[147,148] However, even with an electrode doped with boron in the metallic regime a few issues remain when probing outer sphere redox mediators with a standard electrode potential ($E^{0'}$) very far negative of the flatband potential, far in the depletion region. One such mediator is $Ru(NH_3)_6^{3+/+2}$.[117]

The majority of literature where pBDD has been used as an electrode material investigates the average electrochemical response of the entire surface (macro response), but as mentioned above, pBDD presents a heterogeneous surface due to its polycrystalline nature and the variation in boron content. Imaging techniques have been employed to investigate this heterogeneity (at the micron scale). Electrochemical imaging (SECM) has been used, in particular, to determine where the main electrochemical sites may be. There are examples, and some debate, about whether this activity is at grain boundaries or for select grains only, or whether the entire surface is active.[133,149-151] Scanning electrochemical microscopy (SECM) is a common electrochemical imaging method. Some examples of SECM images of pBDD can be seen in Figure 1.10. These illustrate that the redox activity of pBDD is heterogeneous, but the spatial resolution is not sufficient to correlate these heterogeneities at the microscale. A goal of this thesis is to greatly improve the spatial resolution of electrochemical imaging so that electrochemical activity can be correlated with structure properties for the first time.

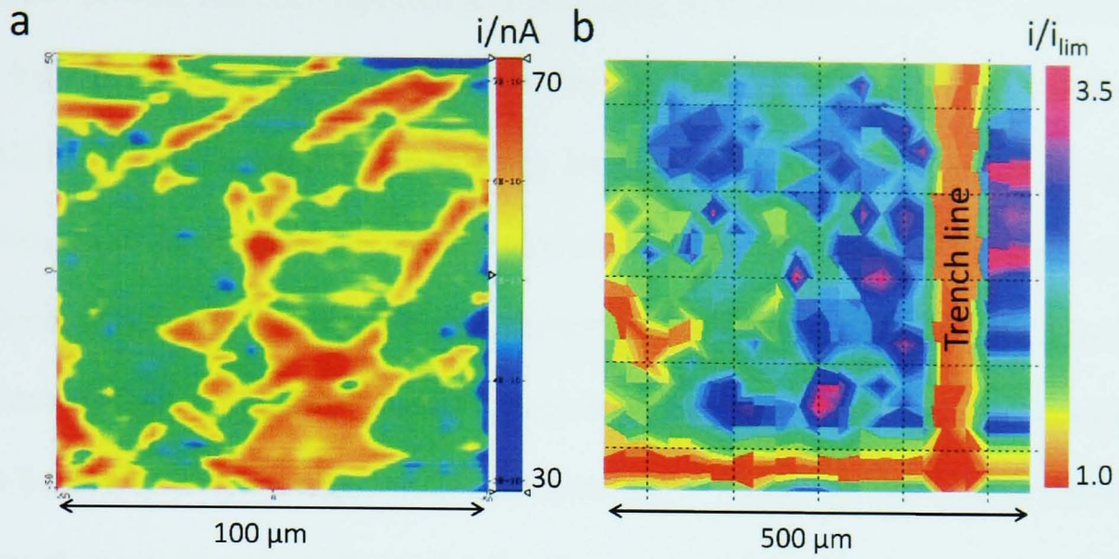

Figure 1.10 a) 100 x 100 µm SECM image of pBDD taken using feedback mode with 1 mM $Ru(NH_3)_6^{3+}$ in bulk solution[151] b)500 x 500 µm substrate-generation tip collection mode SECM (SG-TC SECM) image showing the reduction of 5 mM $Ru(NH_3)_6^{3+}$ (in bulk solution) when the substrate was held at -0.3 V and the Pt UME held at 0 V to collect $Ru(NH_3)_6^{2+}$

1.4.3 Employment as an Electrocatalyst Support Material

Boron doped diamond is an excellent choice as an electrocatalyst support material for many reasons. One major advantage over other carbon materials is that it can withstand the typically harsh environments, including low pH and high potentials, where other carbon supports such as glassy carbon or carbon powder would be oxidised or degrade very quickly. pBDD is also preferable, as it is inert for many electrocatalytic reactions thus producing minimal, interfering background currents when studying the intrinsic properties of deposited catalysts. The substrate can be modified readily with various catalytic nanoparticles. The deposition procedure of such nanoparticles has considered chemical deposition and electrodeposition, with a higher density of particles deposited via electrodeposition.[152]

pBDD powder has been reported as a promising form of diamond,[153-156] enabling a high density of dispersed nanoparticles to be deposited across the sample. pBDD powder is created by coating insulating diamond with boron doped diamond using MWCVD.[154] In one study, increasing the growth of BDD caused fusion of particles and, when electrochemically tested with a simple outer sphere redox mediator, using CV, resistive behaviour was observed. This was thought to be due to poor particle-particle connectivity.[154] Although this pBDD power was shown to be potentially useful, the electrodeposition of Pt nanoparticles onto pBDD films have also been explored. The study revealed that NPs adhered better to the (111) facet than any other, after electrocatalytic reactions were performed on the substrate.[157] Thus, although a pBDD powder has been utilised, a powder with preferential crystal orientation may be more suitable for functionalising with NPs.[157]

In addition to powders, carbon paper has been coated with nanocrystalline pBDD, before modification with NPs. These particles were shown to have a good electrical contact with the substrate where a Pt oxide stripping peak could be observed from CV measurements and the surface area of these particles was determined via the hydrogen adsorption peak.[158]

Many electrocatalytic studies employing BDD as a support material are those investigating methanol oxidation, where diamond acts as the anode.[153] The powdered form of pBDD when modified with Pt showed similar activity towards methanol oxidation to Pt on a graphite powdered support.[156] Other studies where Pt-RuO_2 or Pt RuO_2-O_2 were deposited via the sol gel method were shown to be more promising than just Pt alone as an increase towards both methanol and

ethanol oxidation was observed.[159] Similar results were obtained when the material was modified with Pt-SnO_2 and Pt-Ta_2O_5.[160] The reasons for this enhanced activity, compared to Pt alone, was attributed to either the promotion of CO oxidation or by facilitating the desorption of weakly adsorbed CO from the Pt.[159] A further study that showed a good response towards the oxidation of methanol employed a diamond film with incorporated Pt particles.[161] The films were grown using CVD and the particles were actually added during the growth process, such that larger particles (100 - 500 nm in diameter) were deposited at the grain boundaries and smaller ones (10 - 50 nm in diameter) on the surface of the grains, as shown in a contact mode AFM image (Figure 1.11a). However, a drawback of this method, especially for use in a fuel cell environment, is that graphitic carbon is also present in the Pt/BDD substrate, a feature shown in the Raman spectra. This was attributed to the sp^2 carbon forming between the Pt particles and the diamond during growth.[161]

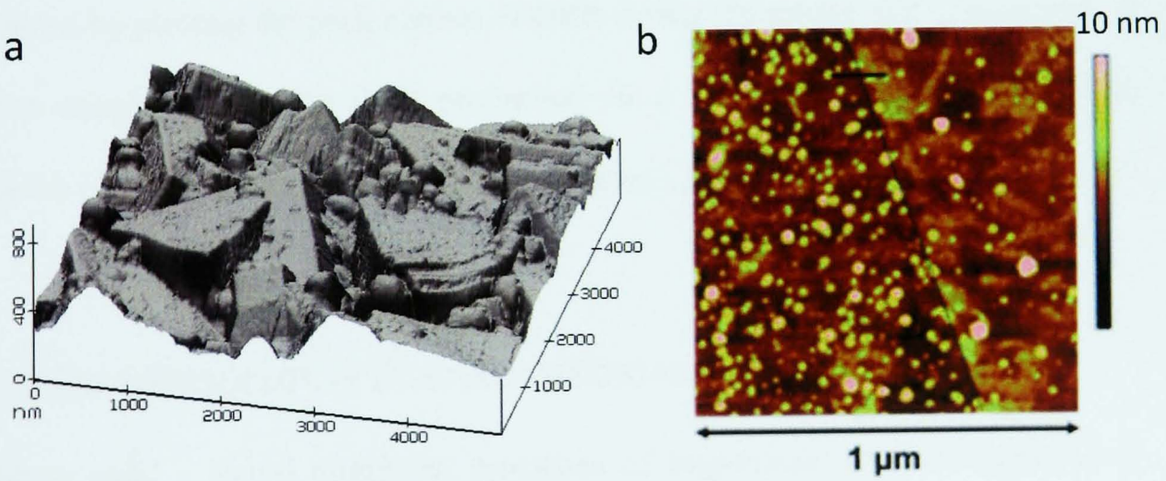

Figure 1.11 a) Contact Mode AFM height image of a BDD thin film deposited with Pt[161] b) Tapping Mode AFM image of Pt nanoparticles electrodeposited onto a 500 µm thick pBDD substrate[142]

The other main reaction investigated is where BDD is employed as the cathode, for studies of the ORR. The effect of diamond surface termination on this reaction has been discussed.[162] Oxygen terminated pBDD, modified with electrodeposited Pt NPs (Figure 1.11b), showed excellent characteristics as a quantitative electrochemical sensor for the ORR, whereas the pBDD alone showed no evidence for ORR in the potential region *ca.* -0.5 V to 1.0 V (vs. SCE).[142] In a separate study, both hydrogen- terminated and oxygen- terminated BDD modified with Au showed higher catalytic activity than a bare Au electrode towards the ORR.[163] Additionally, an enhancement of activity was seen for bi-metallic electrodes, compared with bare Au. In this case, Au was sputtered directly onto the pBDD before Pt was deposited on top of this.[164].

A further study using either Pd NP or Au NP modification of BDD showed that Pd was actually more promising towards the ORR, with higher activity seen in basic media than on Au NPs. In both cases, some mechanistic information was gained by plotting the peak current of ORR versus the square root of scan rate. It was concluded that the ORR proceeded via a four electron transfer pathway, hence reducing directly to water (see Equation 1.2).

1.5 High Resolution Electrochemical Imaging Techniques

Many solid – liquid interfacial processes of importance are heterogeneous in nature and involve electron transfer events at microscopic and smaller structures. For example, fuel cell catalysis occurs at active nanoparticles.[165,166] In order to visualise and quantify these processes, high resolution electrical and electrochemical imaging techniques are required.

1.5.1 Scanning Electrochemical Microscopy (SECM)

The most commonly employed electrochemical imaging technique to-date is the scanning electrochemical microscope (SECM). SECM was first described by Bard *et al.* in 1989[167]. SECM has been used for a variety of applications including studying homogeneous and heterogeneous electron transfer reactions,[168,169] high resolution imaging of chemical reactivity, topography of various interfaces and for micro-fabrication. In addition, SECM has been a useful tool for the optimisation of electrocatalyst composition, whereby arrays of varying composition can be rapidly screened.[165,170]

SECM employs an ultramicroelectrode (UME) as the tip, i.e. an electrode with at least one dimension in the micrometer or smaller regime. Typically, a potential is applied to the UME (with respect to the reference electrode) and a current is measured as the tip is scanned, in a solution containing an electroactive species, whilst being close to the surface of interest. The surface perturbs the electrochemical response of the tip which then provides information about the sample reactivity (and topography). Spatial resolution of SECM is limited by the size of the tip and the minimum current that can be accurately measured. To achieve sub-micron resolution using SECM is challenging, due to the difficulties in producing sub-micron electrodes of characterisable geometry, and the fact that in conventional use there is no feedback in SECM which controls the tip sample separation, hence tip-crash is likely.

A number of methods have been described for the fabrication of sub-micron and nanometre-sized electrodes. In particular, the manufacture of Pt electrodes with

dimensions in the range of ten nanometres to several micrometres has been described.[171] To produce such electrodes, a Pt wire was etched to a sharp point by placing it in a saturated sodium nitrate solution and applying an alternating voltage between the wire and the Pt coil surrounding it. The electrode was then insulated by electrodepositing an insulating paint which retracted from sharp features (the tip in this case) upon heat curing. There are a number of materials that UMEs can be fabricated from, although metals, in particular Pt, are the most common.

Conventional SECM methodologies have been adapted and improved.[172,173] one of the approaches involved a non-optical shear-force-based detection scheme that enabled the tip-to–sample distance in SECM to be controlled.[174] The technique was tested and allowed imaging of both the topography and conductivity of an array of Pt-band microelectrodes. This type of imaging was successful, as the appearance of shear forces between the tip (a 10 μm diameter Pt disk electrode and surrounding glass sheath of > 100 μm) and the sample surface were measured using two piezoelectric plates. One of these plates was used to stimulate the tip, whilst the other monitored the amplitude of the tip oscillation. The spatial resolution that was attained in this work was limited by the dimensions of the Pt electrode therefore further work employed smaller tip dimensions where the Pt-disk nanoelectrodes were reported to have a 450 nm radius.[175] These were used as scanning probes for high resolution SECM.[176] The Pt nanoelectrodes were able to be positioned accurately for both tip-approach experiments and SECM imaging.

1.5.2 Combined Scanning Electrochemical Microscopy with Atomic Force Microscopy (SECM-AFM)

There have been a variety of ways proposed to overcome the difficulties imaging with sub-micron electrodes (i.e. tip crash due to no feedback) such as combining SECM with other techniques, which act to control the tip-substrate separation. Using SECM and AFM in combination[177-180] allows both the surface topography and the electrochemical activity to be monitored independently. This can be achieved by using scanning probes which can act as both electrochemical sensors and force sensing probes, via an AFM component. Combined SECM-AFM has enabled imaging under fluids, providing topographical and electrochemical measurements.[102,181-183] The combined technique can be used in tapping mode which enables the imaging of soft sample surfaces, such as biological specimens. This was made use of for the imaging of enzyme activity.[184] Another application of using SECM-AFM is the imaging of diffusion through single nanoscale pores.[185] The porous system used was a polycarbonate membrane, with 100 nm diameter pores. An SECM-AFM probe enabled the imaging of diffusion within the nanopores which were filled with a redox active electrolyte solution.

SECM-AFM probes were initially hand fabricated using a Pt wire as the starting material which was bent, etched (to form the tip) and flattened to form the cantilever (AFM) and finally insulated. This technique worked well but suffered from irreproducibility between tips. By moving to batch micro fabrication processes, a range of electrode geometries can be integrated within the AFM tip including triangles, rings and disks.[180,186,187]

Burt *et al.* built on previous work which showed how a metal nanowire could be formed at the apex of an AFM tip by using bundles of single-walled carbon nanotubes as a template. They were able to modify the nanowire by coating it with a conformal insulator, poly(oxyphenylene), and cutting off the end using focussed ion beam to produce a nanoelectrode.[179] The fabricated probe was measured to be approximately 400 nm in diameter with the central Au nanowire measuring approximately 80 nm. FE-SEM and TEM images were able to reveal this information. The work carried out is significant as it may enable electrochemical heterogeneity in the nanoscale range to be studied.

1.5.3 Scanning Microcapillary Methods

Research has been carried out using a microcapillary as an electrochemical cell;[188-190] here the resolution of the electrochemical measurement is controlled by the inner diameter of the capillary. The surface is the working electrode and a reference electrode placed in the solution filled capillary completes the circuit. Most of the early experiments were applied to corrosion systems.[190,191] For example, Suter and Böhni's research investigated pit initiation on steels using larger microcapillaries (filled with electrolyte), ranging from 1 to 1000 μm in diameter, as the microcell.[190] They discovered that MnS inclusions present in the stainless steel which acted as nucleation sites for pitting corrosion were dissolved in chloride free solutions; even though stable pit growth occurs in the presence of chlorides. The technique allowed them to distinguish between active and inactive inclusions.[190] Later work, based on the microcapillary method showed that they were able to investigate the kinetics of surface areas activated by tribocorrosion properties.[192] Another study looked at the corrosion behaviour of PVD-coated

magnesium alloys which made use of the electrochemical microprobe. It was used to determine the properties of both the intact and the damaged coating-substrate compound.[193]

Böhni *et al.* later developed a capillary-based droplet cell which contained three electrodes.[194] This technique was shown to work well down to the micrometer range; however limitations to the system included an immobile electrolyte solution.

The capillary method was improved by the concept of a scanning droplet cell[195] however the handling of two capillaries simultaneously was complex. Therefore, the concept of employing a theta capillary was investigated. One barrel would act as an inlet and the other as an outlet, where the electrolyte solution could flow through the system and thus be changed when needed.[189]

More recently the scanning micropipette contact method (SMCM)[101] was developed at Warwick. Rather than focussing on processes related to corrosion and passivation,[192] it was used for the investigation of electrochemical processes involving solution redox couples.[101] Highly oriented pyrolytic graphite (HOPG) was one of the materials examined, determining that the basal plane of HOPG is highly electroactive, contrary to previous belief.[46,47]

1.5.4 Other High Resolution Imaging Methods

Two additional recently developed high resolution imaging techniques have not been addressed thus far. These are intermittent contact scanning electrochemical

microscopy (IC-SECM)[196] and scanning electrochemical cell microscopy (SECCM),[197] which are techniques that have greatly enhanced the capabilities of SECM and SMCM, respectively.

IC-SECM differs from conventional SECM in that the UME is physically oscillated with a small amplitude in the direction normal to the substrate surface. On approach to a substrate this oscillation becomes damped when the end of the tip just makes contact with the sample. This damping is utilised for feedback, enabling the tip to be 'in contact' with the substrate following the surface contours. IC-SECM has proven to be a useful tool for the visualisation and quantification of mass transport through porous membranes such as dentine.[198] IC-SECM is described in more detail in Chapter 4.

SECCM employs a theta capillary which can be filled with electrolyte and / or redox mediator. This can be used as an electrochemical cell in small, localised regions, where the effective size of electrode is governed by the dimensions of the meniscus formed. This technique is described in more detail in Chapter 5.

1.6 Aims and Objectives

There are still many issues remaining which negatively impact FC technology and performance, as highlighted herein. Much research remains to be carried out, particularly regarding the materials used for both the electrocatalyst and the support. FCs are promising for widespread commercial applications but fundamental research in this field is needed to elucidate basic electrocatalytic

processes, leading to the rational design and optimisation of electrocatalysts and support.

After Chapter 2, which details the experimental methods, the role of the electrocatalyst supporting material is explored in Chapter 3. Pt nanoparticles are electrodeposited onto bare HOPG and polymer coated HOPG. The NPs are fully characterised via atomic force microscopy (AFM) and electrochemical techniques, to ensure accurate size measurements and their dispersion on each support. The electroactivity towards both methanol oxidation and formic acid oxidation are explored in relation to the role of the support materials.

Chapter 4 and Chapter 5 present work on the micron scale instead of the macro scale. These chapters employ new imaging methodologies to explore fundamental properties of boron doped diamond before use as an electrocatalyst support material (Chapter 6). Intermittent-contact scanning electrochemical microscopy (IC-SECM) and scanning electrochemical cell microscopy (SECCM) have, for the first time, enabled inherent grain structure, present in pBDD, to be directly linked with regions of high or low electrochemical activity. The rate of electron transfer of different mediators is determined with use of finite element simulations. The merits of these methods compared to alternative electrochemical imaging methods are explained and fully illustrated.

After the determination of the fundamental properties of pBDD, this material was then employed to fabricate a novel pBDD rotating disk electrode (RDE). The RDE was fully characterised using cyclic voltammetry (CV), with the capability of using the RDE in elevated temperatures demonstrated. This electrode was

then modified with Pt nanoparticles via electrodeposition. The oxygen reduction reaction (ORR) was investigated as a proof of principle for this electrode material as shown in Chapter 6.

Finally, some concluding remarks and directions for future work are highlighted in Chapter 7, which also serves as a summary of the work carried out.

1.7 REFERENCES

(1) Grove, W. *The London and Edinburgh Philosophical Magazine and Journal of Science* **1839**, *14*, 127.

(2) Bidault, F.; Brett, D. J. L.; Middleton, P. H.; Brandon, N. P. *J. Power Sources* **2009**, *187*, 39.

(3) Merle, G.; Wessling, M.; Nijmeijer, K. *J. Membr. Sci.* **2011**, *377*, 1.

(4) Tsipis, E.; Kharton, V. *J. Solid State Electrochem.* **2008**, *12*, 1367.

(5) Sun, C.; Hui, R.; Roller, J. *J. Solid State Electrochem.* **2010**, *14*, 1125.

(6) Michael C, T. *J. Power Sources* **2010**, *195*, 4570.

(7) Litster, S.; McLean, G. *J. Power Sources* **2004**, *130*, 61.

(8) Shao, Y.; Yin, G.; Wang, Z.; Gao, Y. *J. Power Sources* **2007**, *167*, 235.

(9) de Bruijn, F. A.; Dam, V. A. T.; Janssen, G. J. M. *Fuel Cells* **2008**, *8*, 3.

(10) Yu, X.; Ye, S. *J. Power Sources* **2007**, *172*, 133.

(11) Yu, X.; Ye, S. *J. Power Sources* **2007**, *172*, 145.

(12) Sammes, N.; Bove, R.; Stahl, K. *Current Opinion in Solid State and Materials Science* **2004**, *8*, 372.

(13) Basri, S.; Kamarudin, S. K.; Daud, W. R. W.; Yaakub, Z. *Int. J. Hydrogen Energy* **2010**, *35*, 7957.

(14) Antolini, E.; Lopes, T.; Gonzalez, E. R. *J. Alloys Compd.* **2008**, *461*, 253.

(15) DeLuca, N. W.; Elabd, Y. A. *Journal of Polymer Science Part B: Polymer Physics* **2006**, *44*, 2201.

(16) Liu, H.; Song, C.; Zhang, L.; Zhang, J.; Wang, H.; Wilkinson, D. P. *J. Power Sources* **2006**, *155*, 95.

(17) Andrew L, D. *Current Opinion in Solid State and Materials Science* **2004**, *8*, 379.

(18) Carrette, L.; Friedrich, K. A.; Stimming, U. *ChemPhysChem* **2000**, *1*, 162.

(19) Fishlock, D. *New Scientist Magazine* **1963**, 367.

(20) Costamagna, P.; Srinivasan, S. *J. Power Sources* **2001**, *102*, 242.

(21) *http://www.ballard.com/about-ballard/ Accessed 24-09-11 at 17.51.*

(22) Park, S.; Lee, J.-W.; Popov, B. N. *J. Power Sources* **2008**, *177*, 457.

(23) Lee, W. k.; Shimpalee, S.; Van Zee, J. W. *J. Electrochem. Soc.* **2003**, *150*, A341.

(24) Lin, G.; Van Nguyen, T. *J. Electrochem. Soc.* **2005**, *152*, A1942.

(25) Oedegaard, A.; Hebling, C.; Schmitz, A.; Møller-Holst, S.; Tunold, R. *J. Power Sources* **2004**, *127*, 187.

(26) Ji, M.; Wei, Z. *Energies* **2009**, *2*, 1057.

(27) Zhang, S.; Yuan, X.-Z.; Hin, J. N. C.; Wang, H.; Friedrich, K. A.; Schulze, M. *J. Power Sources* **2009**, *194*, 588.

(28) Ohyagi, S.; Matsuda, T.; Iseki, Y.; Sasaki, T.; Kaito, C. *J. Power Sources* **2011**, *196*, 3743.

(29) Dai, W.; Wang, H.; Yuan, X.-Z.; Martin, J. J.; Yang, D.; Qiao, J.; Ma, J. *Int. J. Hydrogen Energy* **2009**, *34*, 9461.

(30) Yousfi-Steiner, N.; Moçotéguy, P.; Candusso, D.; Hissel, D.; Hernandez, A.; Aslanides, A. *J. Power Sources* **2008**, *183*, 260.

(31) Mougenot, M.; Caillard, A.; Brault, P.; Baranton, S.; Coutanceau, C. *Int. J. Hydrogen Energy* **2011**, *36*, 8429.

(32) Woo, S.; Kim, I.; Lee, J. K.; Bong, S.; Lee, J.; Kim, H. *Electrochim. Acta* **2011**, *56*, 3036.

(33) Esmaeilifar, A.; Rowshanzamir, S.; Eikani, M. H.; Ghazanfari, E. *Energy* **2010**, *35*, 3941.

(34) Stevens, D. A.; Hicks, M. T.; Haugen, G. M.; Dahn, J. R. *J. Electrochem. Soc.* **2005**, *152*, A2309.

(35) Roen, L. M.; Paik, C. H.; Jarvi, T. D. *Electrochem. Solid-State Lett.* **2004**, *7*, A19.

(36) Kinoshita, K.; Bett, J. A. S. *Carbon* **1974**, *12*, 525.

(37) Eastwood, B. J.; Christensen, P. A.; Armstrong, R. D.; Bates, N. R. *J. Solid State Electrochem.* **1999**, *3*, 179.

(38) Beom, W.-J.; Kalubarme, R. S.; Yun, K.-S.; Park, C.-J. *Appl. Surf. Sci.* **2011**, *257*, 9694.

(39) Siroma, Z.; Ishii, K.; Yasuda, K.; Miyazaki, Y.; Inaba, M.; Tasaka, A. *Electrochem. Commun.* **2005**, *7*, 1153.

(40) Maillard, F.; Bonnefont, A.; Micoud, F. *Electrochem. Commun.* **2011**, *13*, 1109.

(41) Andrew L, D. *J. Power Sources* **2006**, *156*, 128.

(42) Liu, Z.; Gan, L. M.; Hong, L.; Chen, W.; Lee, J. Y. *J. Power Sources* **2005**, *139*, 73.

(43) Zhou, Y.; Neyerlin, K.; Olson, T. S.; Pylypenko, S.; Bult, J.; Dinh, H. N.; Gennett, T.; Shao, Z.; O'Hayre, R. *Energy & Environmental Science* **2010**, *3*, 1437.

(44) Selvaraj, V.; Alagar, M. *Electrochem. Commun.* **2007**, *9*, 1145.

(45) Cui, G.; Shen, P. K.; Meng, H.; Zhao, J.; Wu, G. *J. Power Sources* **2011**, *196*, 6125.

(46) Brandão, L.; Passeira, C.; Mirabile Gattia, D.; Mendes, A. *J. Mater. Sci.* **2011**, *46*, 7198.

(47) Yan, W.-M.; Chu, H.-S.; Lu, M.-X.; Weng, F.-B.; Jung, G.-B.; Lee, C.-Y. *J. Power Sources* **2009**, *188*, 141.

(48) Baschuk, J. J.; Li, X. *International Journal of Energy Research* **2001**, *25*, 695.

(49) Oetjen, H. F.; Schmidt, V. M.; Stimming, U.; Trila, F. *J. Electrochem. Soc.* **1996**, *143*, 3838.

(50) Yu, P.; Pemberton, M.; Plasse, P. *J. Power Sources* **2005**, *144*, 11.

(51) Colón-Mercado, H. R.; Popov, B. N. *J. Power Sources* **2006**, *155*, 253.

(52) Watanabe, M.; Motoo, S. *Journal of Electroanalytical Chemistry and Interfacial Electrochemistry* **1975**, *60*, 267.

(53) Papageorgopoulos, D. C.; Keijzer, M.; de Bruijn, F. A. *Electrochim. Acta* **2002**, *48*, 197.

(54) Santiago, E. I.; Batista, M. S.; Assaf, E. M.; Ticianelli, E. A. *J. Electrochem. Soc.* **2004**, *151*, A944.

(55) Paffett, M. T.; Beery, J. G.; Gottesfeld, S. *J. Electrochem. Soc.* **1988**, *135*, 1431.

(56) Jalan, V.; Taylor, E. J. *J. Electrochem. Soc.* **1983**, *130*, 2299.

(57) Toda, T.; Igarashi, H.; Watanabe, M. *J. Electrochem. Soc.* **1998**, *145*, 4185.

(58) Patra, S.; Munichandraiah, N. *Langmuir* **2008**, *25*, 1732.

(59) Kuo, C.-W.; Huang, L.-M.; Wen, T.-C.; Gopalan, A. *J. Power Sources* **2006**, *160*, 65.

(60) Antolini, E.; Gonzalez, E. R. *Applied Catalysis A: General* **2009**, *365*, 1.

(61) Kulesza, P. J.; Chojak, M.; Karnicka, K.; Miecznikowski, K.; Palys, B.; Lewera, A.; Wieckowski, A. *Chem. Mater.* **2004**, *16*, 4128.

(62) Bensebaa, F.; Farah, A. A.; Wang, D.; Bock, C.; Du, X.; Kung, J.; Le Page, Y. *J. Phys. Chem. B* **2005**, *109*, 15339.

(63) Choi, Y. S.; Joo, S. H.; Lee, S.-A.; You, D. J.; Kim, H.; Pak, C.; Chang, H.; Seung, D. *Macromolecules* **2006**, *39*, 3275.

(64) O'Mullane, A. P.; Dale, S. E.; Macpherson, J. V.; Unwin, P. R. *Chem. Commun. (Cambridge, U. K.)* **2004**, 1606.

(65) O'Mullane, A.; Dale, S.; Day, T.; Wilson, N.; Macpherson, J.; Unwin, P. *J. Solid State Electrochem.* **2006**, *10*, 792.

(66) Liu, S.; Loper Jr, C. R. *Carbon* **1991**, *29*, 547.

(67) McDermott, M. T.; McCreery, R. L. *Langmuir* **1994**, *10*, 4307.

(68) Patel, A. N.; Hung, W. O. Y.; O'Connell, M. A.; Rudd, N. C.; Edwards, M. A.; Macpherson, J. V.; Unwin, P. R. *in preparation* **2011**.

(69) Robinson, R. S.; Sternitzke, K.; McDermott, M. T.; McCreery, R. L. *J. Electrochem. Soc.* **1991**, *138*, 2412.

(70) Peruffo, M.; Contreras-Carballada, P.; Bertoncello, P.; Williams, R. M.; Cola, L. D.; Unwin, P. R. *Electrochem. Commun.* **2009**, *11*, 1885.

(71) Orive, A. G.; Grumelli, D.; Vericat, C.; Ramallo-Lopez, J. M.; Giovanetti, L.; Benitez, G.; Azcarate, J. C.; Corthey, G.; Fonticelli, M. H.; Requejo, F. G.; Creus, A. H.; Salvarezza, R. C. *Nanoscale* **2011**, *3*, 1708.

(72) Brülle, T.; Stimming, U. *J. Electroanal. Chem.* **2009**, *636*, 10.

(73) Rodriguez-Nieto, F. J.; Morante-Catacora, T. Y.; Cabrera, C. R. *J. Electroanal. Chem.* **2004**, *571*, 15.

(74) Cherstiouk, O. V.; Simonov, P. A.; Savinova, E. R. *Electrochim. Acta* **2003**, *48*, 3851.

(75) Penner, R. M. *J. Phys. Chem. B* **2002**, *106*, 3339.

(76) Liu, H.; Favier, F.; Ng, K.; Zach, M. P.; Penner, R. M. *Electrochim. Acta* **2001**, *47*, 671.

(77) Menke, E. J.; Li, Q.; Penner, R. M. *Nano Lett.* **2004**, *4*, 2009.

(78) Zoval, J. V.; Lee, J.; Gorer, S.; Penner, R. M. *J. Phys. Chem. B* **1998**, *102*, 1166.

(79) Bradbury, C. R.; Kuster, L.; Fermín, D. J. *J. Electroanal. Chem.* **2010**, *646*, 114.

(80) Ventosa, E.; Palacios, J. L.; Unwin, P. R. *Electrochem. Commun.* **2008**, *10*, 1752.

(81) Armstrong, F. A.; Bond, A. M.; Hill, H. A. O.; Psalti, I. S. M.; Zoski, C. G. *J. Phys. Chem.* **1989**, *93*, 6485.

(82) Hui, F.; Noël, J.-M.; Poizot, P.; Hapiot, P.; Simonet, J. *Langmuir* **2011**, *27*, 5119.

(83) Hui, F.; Li, B.; He, P.; Hu, J.; Fang, Y. *Electrochem. Commun.* **2009**, *11*, 639.

(84) Bar-Tow, D.; Peled, E.; Burstein, L. *J. Electrochem. Soc.* **1999**, *146*, 824.

(85) Chu, A. C.; Josefowicz, J. Y.; Farrington, G. C. *J. Electrochem. Soc.* **1997**, *144*, 4161.

(86) Buqa, H.; Goers, D.; Holzapfel, M.; Spahr, M. E.; Novak, P. *J. Electrochem. Soc.* **2005**, *152*, A474.

(87) Campana, F. P.; Buqa, H.; Novák, P.; Kötz, R.; Siegenthaler, H. *Electrochem. Commun.* **2008**, *10*, 1590.

(88) Beck, F.; Junge, H.; Krohn, H. *Electrochim. Acta* **1981**, *26*, 799.

(89) Alliata, D.; Häring, P.; Haas, O.; Kötz, R.; Siegenthaler, H. *Electrochem. Commun.* **1999**, *1*, 5.

(90) Bowling, R.; Packard, R. T.; McCreery, R. L. *Langmuir* **1989**, *5*, 683.

(91) Choo, H.-S.; Kinumoto, T.; Nose, M.; Miyazaki, K.; Abe, T.; Ogumi, Z. *J. Power Sources* **2008**, *185*, 740.

(92) Alsmeyer, D. C.; McCreery, R. L. *Anal. Chem.* **1992**, *64*, 1528.

(93) Lee, C.-Y.; Bond, A. M. *Anal. Chem.* **2008**, *81*, 584.

(94) Lee, C.-Y.; Guo, S.-X.; Bond, A. M.; Oldham, K. B. *J. Electroanal. Chem.* **2008**, *615*, 1.

(95) Davies, T. J.; Moore, R. R.; Banks, C. E.; Compton, R. G. *J. Electroanal. Chem.* **2004**, *574*, 123.

(96) Bowling, R. J.; Packard, R. T.; McCreery, R. L. *J. Am. Chem. Soc.* **1989**, *111*, 1217.

(97) Rice, R. J.; McCreery, R. L. *Anal. Chem.* **1989**, *61*, 1637.

(98) Kneten, K. R.; McCreery, R. L. *Anal. Chem.* **1992**, *64*, 2518.

(99) Cline, K. K.; McDermott, M. T.; McCreery, R. L. *J. Phys. Chem.* **1994**, *98*, 5314.

(100) Davies, T. J.; Hyde, M. E.; Compton, R. G. *Angew. Chem.* **2005**, *117*, 5251.

(101) Williams, C. G.; Edwards, M. A.; Colley, A. L.; Macpherson, J. V.; Unwin, P. R. *Anal. Chem.* **2009**, *81*, 2486.

(102) Macpherson, J. V.; Unwin, P. R. *Anal. Chem.* **1999**, *72*, 276.

(103) Patten, H.; Ventosa, E.; Colina, A.; Ruiz, V.; López-Palacios, J.; Wain, A.; Lai, S.; Macpherson, J.; Unwin, P. *J. Solid State Electrochem.*, 1.

(104) Lu, G.; Zangari, G. *Electrochim. Acta* **2006**, *51*, 2531.

(105) Frelink, T.; Visscher, W.; van Veen, J. A. R. *J. Electroanal. Chem.* **1995**, *382*, 65.

(106) Takasu, Y.; Ohashi, N.; Zhang, X. G.; Murakami, Y.; Minagawa, H.; Sato, S.; Yahikozawa, K. *Electrochim. Acta* **1996**, *41*, 2595.

(107) Min, M.-k.; Cho, J.; Cho, K.; Kim, H. *Electrochim. Acta* **2000**, *45*, 4211.

(108) Bergamaski, K.; Pinheiro, A. L. N.; Teixeira-Neto, E.; Nart, F. C. *J. Phys. Chem. B* **2006**, *110*, 19271.

(109) Komanicky, V.; Iddir, H.; Chang, K.-C.; Menzel, A.; Karapetrov, G.; Hennessy, D. C.; Zapol, P.; You, H. *Electrochim. Acta* **2010**, *55*, 7934.

(110) Sánchez-Sánchez, C. M.; Solla-Gullón, J.; Vidal-Iglesias, F. J.; Aldaz, A.; Montiel, V.; Herrero, E. *J. Am. Chem. Soc.* **2010**, *132*, 5622.

(111) Kucernak, A. R.; Chowdhury, P. B.; Wilde, C. P.; Kelsall, G. H.; Zhu, Y. Y.; Williams, D. E. *Electrochim. Acta* **2000**, *45*, 4483.

(112) Morante-Catacora, T. Y.; Ishikawa, Y.; Cabrera, C. R. *J. Electroanal. Chem.* **2008**, *621*, 103.

(113) Zhou, Y.; Pasquarelli, R.; Holme, T.; Berry, J.; Ginley, D.; O'Hayre, R. *J. Mater. Chem.* **2009**, *19*, 7830.

(114) Orive, A. G.; Gimeno, Y.; Creus, A. H.; Grumelli, D.; Vericat, C.; Benitez, G.; Salvarezza, R. C. *Electrochim. Acta* **2009**, *54*, 1589.

(115) Sze, S. M. *Proceedings of the IEEE* **1981**, *69*, 1121.

(116) Collins, A. T.; Williams, A. W. *J. Phys. C.* **1971**, *4*, 1789.

(117) Bott, A. *Curr. Sep.* **1998**, *17*, 87.

(118) Lagrange, J. P.; Deneuville, A.; Gheeraert, E. *Diamond Relat. Mater.* **1998**, *7*, 1390.

(119) Bundy, F. P.; Hall, H. T.; Strong, H. M.; Wentorf, R. H. *Nature* **1955**, *176*, 51.

(120) Sevillano, E.; Williams, B. *Diamond Film Technol.* **1998**, *8*, 73.

(121) Balmer, R. S.; et al. *J. Phys.: Condens. Matter* **2009**, *21*, 364221.

(122) May, P. W. *Philosophical Transactions: Mathematical, Physical and Engineering Sciences* **2000**, *358*, 473.

(123) Kamo, M.; Sato, Y.; Matsumoto, S.; Setaka, N. *J. Cryst. Growth* **1983**, *62*, 642.

(124) Celii, F. G.; Butler, J. E. *Annu. Rev. Phys. Chem.* **1991**, *42*, 643.

(125) Varnin, V. P.; Laptev, V. A.; Ralchenko, V. G. *Inorganic Materials* **2006**, *42*, S1.

(126) Das, D. S., R. N *Int. Mater. Rev.* **2007**, *52*, 29.

(127) Yarbrough, W. A.; Messier, R. *Science* **1990**, *247*, 688.

(128) Iwaki, M.; Sato, S.; Takahashi, K.; Sakairi, H. *Nuclear Instruments and Methods in Physics Research, 209-210, Part 2*, 1129.

(129) Tenne, R.; Patel, K.; Hashimoto, K.; Fujishima, A. *J. Electroanal. Chem.* **1993**, *347*, 409.

(130) Janssen, G.; van Enckevort, W. J. P.; Vollenberg, W.; Giling, L. J. *Diamond Relat. Mater.* **1992**, *1*, 789.

(131) Samlenski, R.; Haug, C.; Brenn, R.; Wild, C.; Locher, R.; Koidl, P. *Diamond Relat. Mater.* **1996**, *5*, 947.

(132) Spitsyn, B. V.; Bouilov, L. L.; Derjaguin, B. V. *J. Cryst. Growth* **1981**, *52*, 219.

(133) Wilson, N. R.; Clewes, S. L.; Newton, M. E.; Unwin, P. R.; Macpherson, J. V. *J. Phys. Chem. B* **2006**, *110*, 5639.

(134) Shiomi, H.; Nishibayashi, Y.; Fujimori, N. *Jpn. J. Appl. Phys., Part 1* **1991**, *30*, 1363.

(135) Salazar-Banda, G. R.; Andrade, L. S.; Nascente, P. A. P.; Pizani, P. S.; Rocha, R. C.; Avaca, L. A. *Electrochim. Acta* **2006**, *51*, 4612.

(136) Ghodbane, S.; Ballutaud, D.; Omnes, F.; Agnes, C. *Diamond Relat. Mater.* **2010**, *19*, 630.

(137) Martin, H. B.; Argoitia, A.; Landau, U.; Anderson, A. B.; Angus, J. C. *J. Electrochem. Soc.* **1996**, *143*, L133.

(138) Hoffmann, R.; Kriele, A.; Obloh, H.; Hees, J.; Wolfer, M.; Smirnov, W.; Yang, N.; Nebel, C. E. *Appl. Phys. Lett.* **2010**, *97*, 052103.

(139) Bennett, J. A.; Wang, J.; Show, Y.; Swain, G. M. *J. Electrochem. Soc.* **2004**, *151*, E306.

(140) Knight, D. S.; White, W. B. *J. Mater. Res.* **1989**, *4*, 385.

(141) Bachmann, P. K.; Leers, D.; Lydtin, H. *Diamond Relat. Mater.* **1991**, *1*, 1.

(142) Hutton, L.; Newton, M. E.; Unwin, P. R.; Macpherson, J. V. *Anal. Chem.* **2008**, *81*, 1023.

(143) Duo, I.; Fujishima, A.; Comninellis, C. *Electrochem. Commun.* **2003**, *5*, 695.

(144) Yagi, I.; Notsu, H.; Kondo, T.; Tryk, D. A.; Fujishima, A. *J. Electroanal. Chem.* **1999**, *473*, 173.

(145) Sarada, B. V.; Rao, T. N.; Tryk, D. A.; Fujishima, A. *Anal. Chem.* **2000**, *72*, 1632.

(146) Granger, M. C.; Witek, M.; Xu, J.; Wang, J.; Hupert, M.; Hanks, A.; Koppang, M. D.; Butler, J. E.; Lucazeau, G.; Mermoux, M.; Strojek, J. W.; Swain, G. M. *Anal. Chem.* **2000**, *72*, 3793.

(147) Angus, J. C.; Martin, H. B.; Landau, U.; Evstefeeva, Y. E.; Miller, B.; Vinokur, N. *New Diamond Front. Carbon Technol.* **1999**, *9*, 175.

(148) Modestov, A. D.; Evstefeeva, Y. E.; Pleskov, Y. V.; Mazin, V. M.; Varnin, V. P.; Teremetskaya, I. G. *J. Electroanal. Chem.* **1997**, *431*, 211.

(149) Holt, K. B.; Bard, A. J.; Show, Y.; Swain, G. M. *J. Phys. Chem. B* **2004**, *108*, 15117.

(150) Wang, S.; Swain, G. M. *J. Phys. Chem. C* **2007**, *111*, 3986.

(151) Neufeld, A.; O'Mullane, A. *J. Solid State Electrochem.* **2006**, *10*, 808.

(152) Montilla, F.; Morallón, E.; Duo, I.; Comninellis, C.; Vázquez, J. L. *Electrochim. Acta* **2003**, *48*, 3891.

(153) Salazar-Banda, G. R.; Eguiluz, K. I. B.; Avaca, L. A. *Electrochem. Commun.* **2007**, *9*, 59.

(154) Fischer, A. E.; Swain, G. M. *J. Electrochem. Soc.* **2005**, *152*, B369.

(155) Ay, A.; Swope, V. M.; Swain, G. M. *J. Electrochem. Soc.* **2008**, *155*, B1013.

(156) Spataru, N.; Zhang, X.; Spataru, T.; Tryk, D. A.; Fujishima, A. *J. Electrochem. Soc.* **2008**, *155*, B264.

(157) González-González, I.; Fachini, E. o. R.; Scibioh, M. A.; Tryk, D. A.; Tague, M.; Abruña, H. c. D.; Cabrera, C. R. *Langmuir* **2009**, *25*, 10329.

(158) Fischer, A. E.; Lowe, M. A.; Swain, G. M. *J. Electrochem. Soc.* **2007**, *154*, K61.

(159) Salazar-Banda, G. R.; Suffredini, H. B.; Calegaro, M. L.; Tanimoto, S. T.; Avaca, L. A. *J. Power Sources* **2006**, *162*, 9.

(160) Salazar-Banda, G. R.; Suffredini, H. B.; Avaca, L. A.; Machado, S. A. S. *Mater. Chem. Phys.* **2009**, *117*, 434.

(161) Wang, J.; Swain, G. M.; Tachibana, T.; Kobashi, K. *Electrochem. Solid-State Lett.* **2000**, *3*, 286.

(162) Szunerits, S.; Manesse, M.; Actis, P.; Marcus, B.; Denuault, G.; Jama, C.; Boukherroub, R. *Electrochem. Solid-State Lett.* **2007**, *10*, G43.

(163) Yano, T.; Tryk, D. A.; Hashimoto, K.; Fujishima, A. *J. Electrochem. Soc.* **1998**, *145*, 1870.

(164) El Roustom, B.; Siné, G.; Fóti, G.; Comninellis, C. *J. Appl. Electrochem.* **2007**, *37*, 1227.

(165) Lu, G.; Cooper, J. S.; McGinn, P. J. *J. Power Sources* **2006**, *161*, 106.

(166) Lu, G.; Cooper, J. S.; McGinn, P. J. *Electrochim. Acta* **2007**, *52*, 5172.

(167) Bard, A. J.; Fan, F. R. F.; Kwak, J.; Lev, O. *Anal. Chem.* **1989**, *61*, 132.

(168) Bai, Y.; Sun, P.; Zhang, M.; Gao, Z.; Yang, Z.; Shao, Y. *Electrochim. Acta* **2003**, *48*, 3447.

(169) Bollo, S.; Finger, S.; Sturm, J. C.; Núñez-Vergara, L. J.; Squella, J. A. *Electrochim. Acta* **2007**, *52*, 4892.

(170) Fernández, J. L.; Walsh, D. A.; Bard, A. J. *J. Am. Chem. Soc.* **2004**, *127*, 357.

(171) Slevin, C. J.; Gray, N. J.; Macpherson, J. V.; Webb, M. A.; Unwin, P. R. *Electrochem. Commun.* **1999**, *1*, 282.

(172) Brunner, R.; Bietsch, A.; Hollricher, O.; Marti, O. *Rev. Sci. Instrum.* **1997**, *68*, 1769.

(173) Hollricher, O.; Brunner, R.; Marti, O. *Ultramicroscopy* **1998**, *71*, 143.

(174) Ballesteros Katemann, B.; Schulte, A.; Schuhmann, W. *Chemistry – A European Journal* **2003**, *9*, 2025.

(175) Katemann, B. B.; Schuhmann, W. *Electroanalysis* **2002**, *14*, 22.

(176) Ballesteros Katemann, B.; Schulte, A.; Schuhmann, W. *Electroanalysis* **2004**, *16*, 60.

(177) Wain, A. J.; Cox, D.; Zhou, S. Q.; Turnbull, A. *Electrochem. Commun.* **2011**, *13*, 78.

(178) Leonhardt, K.; Avdic, A.; Lugstein, A.; Pobelov, I.; Wandlowski, T.; Wu, M.; Gollas, B.; Denuault, G. *Anal. Chem.* **2011**, *83*, 2971.

(179) Burt, D. P.; Wilson, N. R.; Weaver, J. M. R.; Dobson, P. S.; Macpherson, J. V. *Nano Lett.* **2005**, *5*, 639.

(180) Holder, M. N.; Gardner, C. E.; Macpherson, J. V.; Unwin, P. R. *J. Electroanal. Chem.* **2005**, *585*, 8.

(181) Williams, D. E.; Mohiuddin, T. F.; Zhu, Y. Y. *J. Electrochem. Soc.* **1998**, *145*, 2664.

(182) Jones, C. E.; Macpherson, J. V.; Barber, Z. H.; Somekh, R. E.; Unwin, P. R. *Electrochem. Commun.* **1999**, *1*, 55.

(183) Eckhard, K.; Shin, H.; Mizaikoff, B.; Schuhmann, W.; Kranz, C. *Electrochem. Commun.* **2007**, *9*, 1311.

(184) Kueng, A.; Kranz, C.; Lugstein, A.; Bertagnolli, E.; Mizaikoff, B. *Angewandte Chemie International Edition* **2003**, *42*, 3238.

(185) Macpherson, J. V.; Jones, C. E.; Barker, A. L.; Unwin, P. R. *Anal. Chem.* **2002**, *74*, 1841.

(186) Dobson, P. S.; Weaver, J. M. R.; Holder, M. N.; Unwin, P. R.; Macpherson, J. V. *Anal. Chem.* **2004**, *77*, 424.

(187) Shin, H.; Hesketh, P. J.; Mizaikoff, B.; Kranz, C. *Anal. Chem.* **2007**, *79*, 4769.

(188) Spaine, T. W.; Baur, J. E. *Anal. Chem.* **2001**, *73*, 930.

(189) Lohrengel, M. M.; Rosenkranz, C.; Klüppel, I.; Moehring, A.; Bettermann, H.; Bossche, B. V. d.; Deconinck, J. *Electrochim. Acta* **2004**, *49*, 2863.

(190) Suter, T.; Böhni, H. *Electrochim. Acta* **1997**, *42*, 3275.

(191) Böhni, H.; Suter, T.; Schreyer, A. *Electrochim. Acta* **1995**, *40*, 1361.

(192) Böhni, H.; Suter, T.; Assi, F. *Surf. Coat. Technol.* **2000**, *130*, 80.

(193) Hoche, H.; Rosenkranz, C.; Delp, A.; Lohrengel, M. M.; Broszeit, E.; Berger, C. *Surf. Coat. Technol.* **2005**, *193*, 178.

(194) Suter, T.; Böhni, H. *Electrochim. Acta* **2001**, *47*, 191.

(195) Lohrengel, M. M.; Moehring, A.; Pilaski, M. *Fresenius. J. Anal. Chem.* **2000**, *367*, 334.

(196) McKelvey, K.; Edwards, M. A.; Unwin, P. R. *Anal. Chem.* **2010**, *82*, 6334.

(197) Ebejer, N.; Schnippering, M.; Colburn, A. W.; Edwards, M. A.; Unwin, P. R. *Anal. Chem.* **2010**, *82*, 9141.

(198) McKelvey, K.; Snowden, M. E.; Peruffo, M.; Unwin, P. R. *Anal. Chem.* **2011**, *83*, 6447.

CHAPTER 2

EXPERIMENTAL

This Chapter details the chemicals, materials, electrode fabrication and experimental procedures employed throughout this thesis.

CHEMICALS

All aqueous solutions were prepared from Milli-Q reagent water (Millipore Corp.) with resistivity of 18.2 MΩ cm at 25 °C. All chemicals used in this thesis are detailed in Table 2.1. They were all weighed using a four figure analytical balance (Sartorius A2008).

Table 2.1 A list of chemicals used in this thesis

Chemicals	Details	Supplier
Ruthenium (III) hexaamine, $Ru(NH_3)_6^{3+}$	99%	Strem Chemicals Ltd.
Ferrocenylmethyltrimethylammonium hexafluorophosphate, $FcTMA^+PF_6$	Prepared in - house from $FcTMA^+I^-$ via metathesis with Ag^+PF_6	
Ferrocenylmethyltrimethylammonium iodide, $FcTMA^+I^-$	99%	Strem Chemicals Ltd.
Silver hexafluorophosphate, Ag^+PF_6	99.5%	Strem Chemicals Ltd.
Potassium nitrate, KNO_3	99%,	Fisher Scientific Ltd.
Potassium Chloride, KCl	99 %	Sigma-Aldrich

Methanol, CH_3OH	99.99 %	Fisher Scientific
Sulphuric Acid, H_2SO_4	TraceSELECT® ≥95 %	Sigma-Aldrich
HEPES	99 %	Fluka
Serotonin (5-hydroxytryptamine)		Sigma-Aldrich
Ferrosulphate, $FeSO_4$		Sigma-Aldrich
Lithium perchlorate, $LiClO_4$	≥ 95 %	Sigma-Aldrich
3,4-ethylenedioxythiophene (EDOT)		Sigma-Aldrich
Perchloric Acid, $HClO_4$	74 %	Acros Organics
Formic Acid, HCOOH	≥ 98 %	Sigma-Aldrich
Potassium hexachloroplatinate, K_2PtCl_6	98 %	Sigma-Aldrich

2.2 MATERIALS

2.2.1 HOPG

SPI-1 grade HOPG (Structure Probe Inc.) was employed as the working electrode in Chapter 3. A 10 x 10 mm sample of HOPG was placed onto a square section of Au-sputtered silicon (sputter-coated (Moorfield minibox conversion) thickness 400 nm), with an underlying electrical contact made using silver DAG (Ag-loaded epoxy, Agar Scientific). Finally, tinned copper wire was soldered to the coated silicon chip in order to make external electrical contact. Prior to any electrochemistry, the HOPG was cleaved revealing a fresh surface, using Scotch tape (3M).

For studies on PEDOT, molecularly smooth films were produced on HOPG as outlined previously, by applying a potential step from +0.5 to +1.05 V for 0.1 s

in a 0.002 M EDOT and 0.1 M $LiClO_4$ solution. As demonstrated elsewhere,[1] growth is governed by a 2-D layer-by-layer process at these low driving forces. The films produced under these conditions typically had a thickness of *ca.* 8 nm.[1]

2.2.2 Polycrystalline Boron Doped Diamond (pBDD)

The pBDD samples were prepared by Element Six Ltd. (E6 Ltd., Ascot, U.K.) using a commercial microwave plasma- chemical vapour deposition (MW-CVD) process, developed in-house. The average boron doping level of this material is about 5×10^{20} atoms cm^{-3}, as determined by secondary ion mass spectrometry (SIMS)[2]. The pBDD employed in this thesis had a thickness of *ca.* 500 μm and an average grain size of 5 – 40 μm. The surface roughness of the pBDD has been characterised using TM-AFM. A typical roughness of 1 – 2 nm has been recorded within a grain, however 1 - 5 nm across grains.

The pBDD employed in this thesis is the same as that sold commercially and used by many different research groups as an electrode for electrochemical measurements. For all of the samples used, a 2 or 3 mm diameter column of pBDD was cut using a laser micromachiner (E-355H-3-ATHI-O system, Oxford Lasers).[3]

This was then acid cleaned by placing the column into H_2SO_4 with KNO_3 and boiling for 1 hour. After rinsing, the column was then placed in a beaker containing only H_2SO_4 and boiled for a further 30 minutes. By boiling in acid the pBDD is cleaned and also oxygen terminated.[4,5] After acid cleaning, an ohmic contact was made to the back of the column by sputtering (Moorfield

Minibox) first Ti (20 nm), followed by Au (400 nm). The sample was then annealed in a tube furnace (Carbolite, UK) at 500°C for 4 hrs to create a titanium carbide contact to the pBDD. Optical images showing the top, back and side of pBDD can be seen in Figure 2.1.

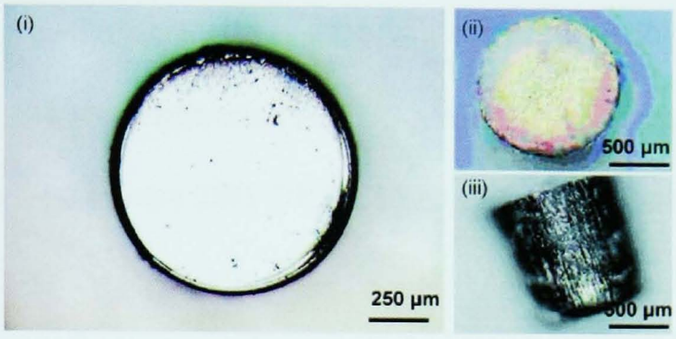

Figure 2.1 Optical images showing the(i) top,(ii) back and(iii) side (Ti/Au sputtered) view of pBDD taken from Ref 3

In Chapter 4 and Chapter 5 the pBDD sample was contacted to a Ti (20 nm) and Au (400 nm) sputter-coated glass slide using Ag paint (Agar Scientific Ltd., UK). Electrical contact was made using tinned copper wire contacted to the slide, again using Ag paint. Double sided tape (3M) was employed to secure the glass slide onto the base of a Teflon SECM cell. The sample was electrically insulated with 5 minute epoxy resin (RS Components, UK) in all areas bar the top surface of the pBDD column.

2.3 Characterisation Techniques

A range of characterisation techniques were employed throughout this thesis including, electrochemical measurements, atomic force microscopy (AFM), field emission scanning electron microscopy (FE-SEM) and Raman spectroscopy.

2.3.1 Electrochemical Measurements

Cyclic voltammetry (CV), linear sweep voltammetry (LSV) and chronoamperometry experiments employed a potentiostat (CH Instruments, model CHI760A) using a typical three electrode set-up where the working electrode is the surface of interest i.e. HOPG or pBDD, the reference electrode is either a saturated calomel electrode (SCE), Ag/AgCl wire or Ag/AgCl (3M KCl) (World Precision Instruments 2SH-DRIREF) and the counter electrode a Pt wire or gauze.

For the experiments performed in Chapter 6 the potentiostat was connected to a rotating disk electrode rotation unit and controller (Pine Instruments). Here, the working electrode was either the pBDD RDE (fabricated in house, details found in Chapter 6) or a Pt RDE (Pine Instruments).

2.3.2 High Resolution Electrochemical Imaging

Intermittent contact – scanning electrochemical microscopy (IC-SECM)[6] and scanning electrochemical cell microscopy (SECCM)[7] were employed to image the pBDD substrate in Chapter 4 and Chapter 5. The experimental details are in the appropriate chapters however some addition information is detailed below.

Figure 2.2a shows a typical camera image before an approach curve and scan starts, for IC-SECM. The Pt UME is brought close to the pBDD surface, where a reflection can be seen, this method is also used to ensure the theta capillary is close to the pBDD before an approach curve is run. Figure 2.2b shows an optical micrograph with the grains of pBDD clearly visible. On both the camera and the

optical image, a trench (50 μm in diameter) is shown which has been laser micromachined into the pBDD disk to provide a reference point for where an electrochemical image is taken from on the sample.

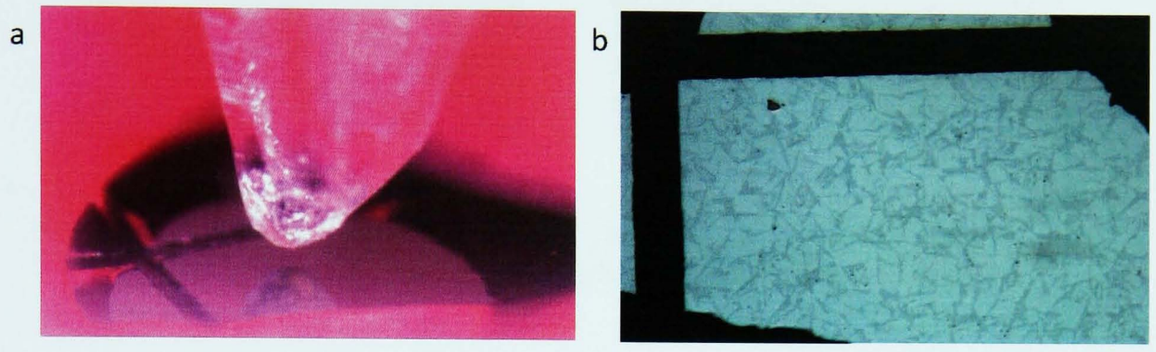

Figure 2.2 a) Camera image to show the positioning of the Pt UME before approach b) Optical micrograph showing a typical surface of a pBDD surface

The capillaries employed in SECCM were 10 mm x 1.5 mm borosilicate theta capillaries (TG 150-10, Harvard Part No. 30-0114) and were laser pulled (Sutter P2000) according to Table 2.2.

Table 2.2 Settings used to pull theta capillaries from 10 cm x 1.5 mm borosilicate capillaries

Heat	Filament	Velocity	Delay	Pull
500	4	30	120	20

After being laser pulled and performing SECCM, the tips were characterised using FE-SEM as shown in Figure 2.3.

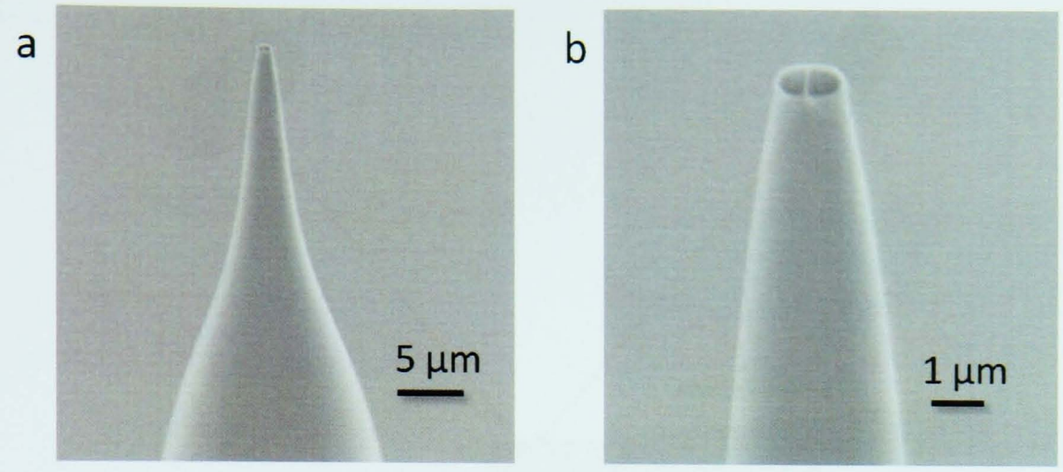

Figure 2.3 FE-SEM images showing a pulled theta capillary where a) lower magnification b) higher magnification

2.3.3 Atomic Force Microscopy (AFM)

In Chapter 3, tapping mode (TM)-atomic force microscopy (AFM) measurements were performed in air using standard Si tapping tips (RRESP-type Veeco Probes) with a Multimode V AFM (Veeco). In Chapter 6 TM-AFM measurements were performed in air using SNL (Bruker Probes) with either a Bioscope Catalyst AFM or a Dimension® Icon® AFM with ScanAsyst™ (Bruker). All images were analysed using Scanning Probe Imaging Processor (SPIP™) software, version 5.1.5 (Image Metrology).

AFM provides nano-scale imaging owing to the sharp tips employed. A schematic of a typical AFM set-up is shown in Figure 2.4. Briefly, a laser is shone onto the back of a force sensitive cantilever (where the tip is connected). Feedback in AFM is based upon force measurements derived from the tip - sample interactions, measured with a force sensitive cantilever. This can be either a static force set - point (contact mode) or due to a damping of oscillation (Tapping, intermittent contact mode).

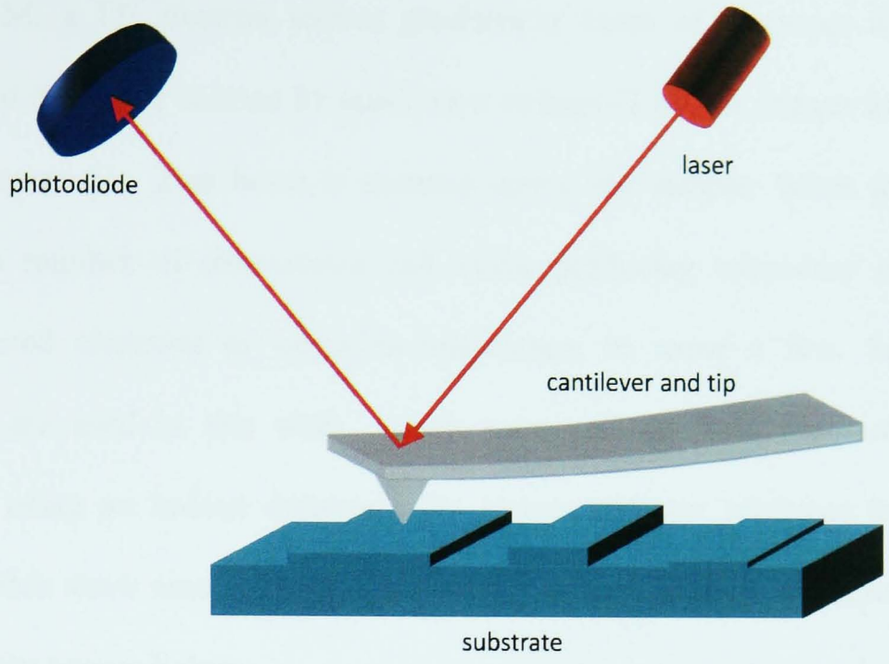

Figure 2.4 Schematic of AFM

The Bioscope Catalyst AFM and the Dimension® Icon® AFM utilise Peak Force Tapping™ mode which performs a force curve at every pixel of an image, where the peak force is used as the feedback signal. This combines intermittent contact (low shear force) imaging with extreme tip-sample force control of contact mode. Using Peak Force Tapping™ mode was particularly useful for imaging pBDD allowing effective use of tips at high resolution with little wear during large scans.

2.3.4 Field Emission Scanning Electron Microscopy (FE-SEM)

Field emission-scanning electrochemical microscopy (FE-SEM) has the ability to record images over large areas. Images of pBDD were recorded (< 75 μm x 75 μm) for Chapter 4 and 5 in this thesis, to show the grain structure using Zeiss Supra 55VP.

In FE-SEM, a FE electron source produces a beam of electrons which are accelerated through a column by applying a voltage (2 kV for images in Chapter 4 and Chapter 5). This beam is scanned across the sample. When it hits the sample, a number of interactions can occur producing secondary electrons, backscattered electrons or cathodoluminescence, to name a few. Secondary electrons are used in this work, which once emitted from the sample, are collected using an in-lens detector. An in-lens detector produces images of pBDD which show areas of high conductivity as dark regions and areas of low conductivity appear lighter.

2.3.5 Micro-Raman Spectroscopy

In Chapter 4 micro-Raman spectroscopy (Renishaw InVia, UK) was performed using a 514.5 nm Ar^+ laser with a CCD detector; Peltier cooled. The spectrometer was equipped with an 1800 lines / mm diffraction grating. Maps were created by using an automated stage (incremental step size of 1.2 μm) where the laser beam was focussed with a 100 × objective. The areas of the peak at ~ 1332 cm^{-1} were analysed (Wire 3.0).

Raman spectroscopy is a technique based on inelastic scattering of monochromatic light, from a laser source. Photons at a given frequency interact with the sample. The sample then emits the photon at a higher frequency (Anti-stokes shift) or a lower frequency (Stokes shift). This shift in frequency is known as Raman shift and individual peaks can be attributed to particular bonds.

Diamond has a characteristic peak at 1332.5 cm^{-1}, the zone centre optical phonon peak. When boron is incorporated into the diamond (> 1 x 10^{20} atoms cm^{-3}) a Fano effect is observed which shifts the 1332.5 cm-1 peak to lower wavenumbers.[8] This peak was analysed in Chapter 4.

The quality of pBDD employed is extremely important. Any impurities present may have an impact on the advantageous properties this material has for use as an electrode material. For example, if there is sp^2 carbon present in electrochemical measurement this may result in a reduced potential window and increased background currents.[9] Raman spectroscopy can be used to assess the quality where, in addition to the characteristic diamond peak at 1332 cm^{-1}, other peaks arise from impurities. Peaks *ca.* 1350 – 1580 cm^{-1} have been attributed to sp^2 carbon[10] and at peaks ca. 1550 – 1500 cm^{-1} indicating amorphous carbon.[11] Figure 2.5 shows graphite impurities in the spectra for a diamond film. The presence of these impurity peaks was negligible in all spectra on pBDD employed in this thesis.

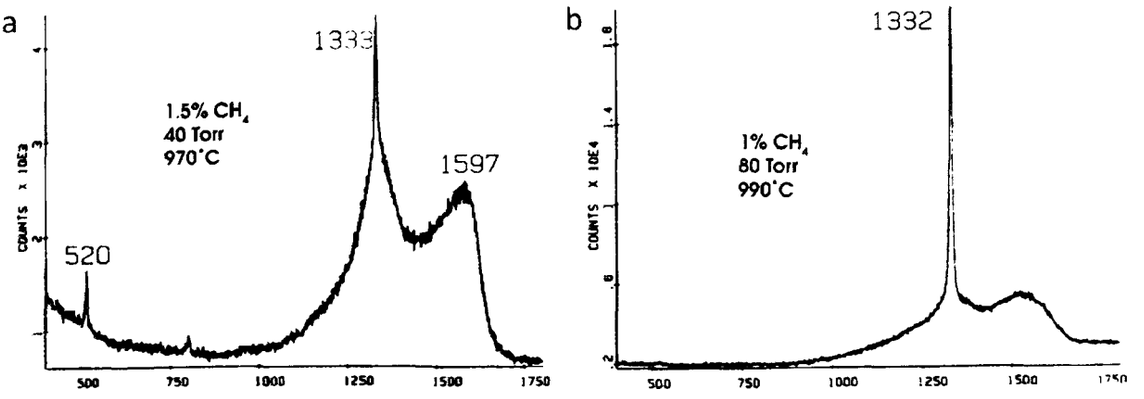

Figure 2.5 Raman spectra of diamond films grown on silicon substrates, showing presence of graphite a) high impurities b) lower impurities taken from Ref. 10

2.4 REFERENCES

(1) Ventosa, E.; Palacios, J. L.; Unwin, P. R. *Electrochem. Commun.* **2008**, *10*, 1752.

(2) Wilson, N. R.; Clewes, S. L.; Newton, M. E.; Unwin, P. R.; Macpherson, J. V. *J. Phys. Chem. B* **2006**, *110*, 5639.

(3) Hutton, L.; Newton, M. E.; Unwin, P. R.; Macpherson, J. V. *Anal. Chem.* **2008**, *81*, 1023.

(4) Pehrsson, P. E.; Long, J. P.; Marchywka, M. J.; Butler, J. E. *Appl. Phys. Lett.* **1995**, *67*, 3414.

(5) Liu, F. B.; Wang, J. D.; Liu, B.; Li, X. M.; Chen, D. R. *Diamond Relat. Mater.* **2007**, *16*, 454.

(6) McKelvey, K.; Edwards, M. A.; Unwin, P. R. *Anal. Chem.* **2010**, *82*, 6334.

(7) Ebejer, N.; Schnippering, M.; Colburn, A. W.; Edwards, M. A.; Unwin, P. R. *Anal. Chem.* **2010**, *82*, 9141.

(8) Lagrange, J. P.; Deneuville, A.; Gheeraert, E. *Diamond Relat. Mater.* **1998**, *7*, 1390.

(9) Yano, T.; Popa, E.; Tryk, D. A.; Hashimoto, K.; Fujishima, A. *J. Electrochem. Soc.* **1999**, *146*, 1081.

(10) Knight, D. S.; White, W. B. *J. Mater. Res.* **1989**, *4*, 385.

(11) Bachmann, P. K.; Leers, D.; Lydtin, H. *Diamond Relat. Mater.* **1991**, *1*, 1.

CHAPTER 3

INFLUENCE OF ULTRATHIN POLY-(3,4-ETHYLENEDIOXYTHIOPHENE) (PEDOT) FILM SUPPORTS ON THE ELECTRODEPOSITION AND ELECTROCATALYTIC ACTIVITY OF DISCRETE PLATINUM NANOPARTICLES

ABSTRACT

Coating a carbon electrode surface, specifically highly oriented pyrolytic graphite (HOPG) with an ultrathin film of poly-(3,4-ethylenedioxythiophene), PEDOT, provides a support on which a high density of uniformly dispersed Pt nanoparticles (NPs) can readily be formed by electrodeposition. The NPs tend to be much smaller, have a higher surface coverage, better dispersion and show a much lower tendency to aggregate, than Pt NPs produced under identical electrochemical conditions on HOPG alone. The electrocatalytic activity of the NPs was investigated for methanol (MeOH) and formic acid (HCOOH) oxidation. Significantly, for similarly prepared particles, Pt NP-PEDOT arrays exhibited higher catalytic activity (in terms of current density, based on the Pt area), towards MeOH oxidation, by an order of magnitude, and towards HCOOH oxidation at high potentials, than Pt NPs supported on native HOPG. These findings can be rationalised in terms of the enhanced oxidation of adsorbed CO, a key reaction intermediate and a catalyst poison.

3.1 INTRODUCTION

Key components of fuel cells are the electrocatalyst and support material. Metal nanoparticles (NPs), typically Pt or Pt–alloys,[1,2] are often employed as the catalyst, usually immobilised on a carbon support. Elucidating the size dependence of electrocatalysis at NPs is of considerable interest.[3,4] Small NPs provide a large area-to-volume ratio which is beneficial for achieving efficient catalyst use, provided there is no reduction in the efficacy of the surface catalytic process. An important consideration is that decreasing the catalyst size may also induce changes in the electronic properties of the particles, which, in turn, may influence their catalytic activity.[5] In addition to particle size effects, the structure and morphology of supported electrocatalysts are also important factors.[6-8]

The development of catalyst dispersion methods and supports for catalytic NPs is of significant interest.[9] It is well-known that the material employed as catalyst support plays an essential role in catalyst activity and stability.[10,11] While carbon materials are most widely used as support materials, conducting polymers (CPs) have also shown great promise.[12-17] Nanocomposites of CPs and NPs have been shown to improve the adherence of NPs to solid electrodes and may impart synergetic electrocatalytic properties,[18,19] notably when employed in the direct methanol fuel cell[15] and the direct formic acid fuel cell.[20]

Methanol (MeOH) oxidation involves several possible pathways, each comprising a number of elementary steps (Figure 3.1), as described by Baltruschat et al.[21,22] and Léger.[23] The oxidation of MeOH can proceed via adsorbed CO (CO_{ads}) (step 1). Although CO_{ads} can be further oxidised to CO_2

(step 2), this reaction is sluggish and requires a high overpotential.[24-26] As a result, CO_{ads} is generally considered a poison in the methanol oxidation mechanism. Alternatively, the reaction may proceed via soluble intermediates such as formic acid (HCOOH; steps 3 and 4). HCOOH oxidation can also occur through more than one pathway resulting in direct oxidation to CO_2 (step 5) or through CO_{ads} (steps 2 and 6).[27-29] This multitude of possible reaction pathways highlights the importance of optimising fuel cell catalyst layers through the assessment of Pt NP electrocatalytic activity in different environments. A previous study showed that by modifying electrodeposited Pt on a glassy carbon electrode with polyindoles, the electrocatalytic activity towards formic acid oxidation was increased. This was attributed to the polyindoles providing a selective pathway, suppressing the formation of CO. This indicated a possible synergetic effect between Pt and polyindoles.[30]

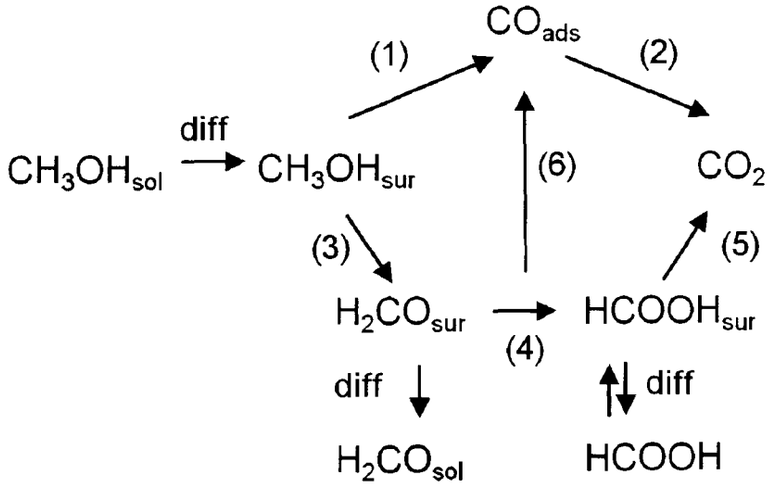

Figure 3.1 Schematic showing the different pathways for MeOH oxidation. Adapted from Baltruschat et al.[21]

Among CPs, poly-(3,4-ethylenedioxythiophene) (PEDOT) has considerable promise as a support for Pt NPs, with enhanced catalytic activity of Pt–PEDOT composites compared to native Pt suggested for the electrooxidation of

MeOH.[31,32] However, the preparation techniques employed in these previous studies resulted in extensive aggregation of NPs, making it difficult to determine the intrinsic activity at the single, isolated particle level and, in particular, elucidate whether PEDOT plays any role in promoting electrocatalysis. In a contrasting report, Pt NP composites with either polypyrrole or PEDOT demonstrated comparable activities towards MeOH oxidation as for a bare Pt electrode.[33] Finally, there is recent evidence for the promotion of electrocatalytic activity for ethanol oxidation by embedding Pd NPs in a PEDOT matrix.[34] In view of the current status of the field, studies with well-defined, non-aggregated Pt NPs are required to elucidate whether PEDOT enhances electrocatalysis at Pt NPs. Such studies are a major focus of this chapter which seeks to compare directly the electrocatalytic activity of isolated, well-defined, Pt NPs on: highly oriented pyrolytic graphite (HOPG) and on molecularly smooth ultrathin films of PEDOT. Through these studies, we are able to determine the influence of PEDOT on enhancing, or otherwise modifying, the activity of Pt NPs towards MeOH and HCOOH oxidation.

Electrodeposition is an attractive route for the formation of tailored nanostructured interfaces, as it provides versatility in the range of particle sizes and surface coverages that can be obtained.[35-37] On the other hand, because such particles are unprotected, there is a tendency for aggregation to occur, and on solid surfaces nucleation and growth may take place at specific locations (e.g. at step edges) leading to non-uniform surface coverages.[38,39] In this work, we show that a further beneficial aspect of PEDOT, as a support, is that it is possible to readily form high-density arrays of small isolated NPs using electrodeposition at

molecularly smooth CP films.[40] The NPs tend to be much smaller and can be deposited with much better dispersion than on bare HOPG.

In this work, the use of such Pt NP-PEDOT arrays for electrocatalysis has been considered through studies of the electrooxidation of MeOH and HCOOH. We are most interested in comparing the activities (in terms of current density) of the different nanostructured interfaces. To this end, the activity of Pt NP-PEDOT has been compared with similarly prepared Pt NPs on HOPG, to fully elucidate the effect of a PEDOT support on heterogeneous electrocatalytic reactions.

3.2 Electrodeposition of Pt NPs on bare and PEDOT-coated HOPG

The electrochemical nucleation and growth of metal NPs on conducting substrates can be controlled by three parameters; the concentration of the metal salt, deposition potential, and deposition time.[41] The last two parameters can be combined by the use of complex potential waveforms.[35] In this study, we mainly considered simple single potential step chronoamperometry, with a deposition time of 10 s in order to elucidate clearly the effect of PEDOT on NP formation. The effect of the salt concentration and deposition potential were investigated. For Pt electrodeposition, the electrode potential was stepped from +0.5 V to a series of different driving potentials in the range −0.1 to −0.4 V. The solution comprised 0.25 M $HClO_4$ with different concentrations of K_2PtCl_6 in the range 1–9 mM. For all driving potentials and timescales, a concentration of 3 mM K_2PtCl_6 was found to give rise to the highest NP surface coverage on PEDOT

films without obvious aggregation; however, aggregation was seen at higher concentrations. We thus focused further on these conditions.

TM-AFM was employed to obtain information on particle size (from maximum height), the particle surface coverage and to determine if there were any preferential sites for deposition on the surfaces of interest. To directly compare Pt electrodeposition on bare and PEDOT-coated HOPG, particles were deposited using chronoamperometry by stepping the potential from 0.5 V to cathodic potentials (10 s). Typical data for a deposition potential of −0.2 V are shown in Figure 3.2. On the PEDOT-coated HOPG (Figure 3.2a), the average particle size is 14 ± 5 nm and the surface coverage is *ca.* nine particles per square micrometer. The image revealed an essentially homogenous dispersion of NPs and no preferential deposition sites on the support electrode. In contrast, for identical deposition parameters, Pt particles electrodeposited on bare HOPG (Figure 3.2b) had an average particle size of 94 ± 17 nm and a coverage of two particles per square micrometer. In general, much larger NP sizes (mainly aggregates) and considerably smaller surface coverages were found on HOPG, with some preferential deposition at step edges. This indicates that the PEDOT film readily promotes the nucleation of a high density of small NPs compared to a bare HOPG electrode. For Pt NPs deposited on PEDOT-coated HOPG, the particle size decreased when the deposition potential was changed from −0.2 to −0.1 V, but small particles could be produced most readily at potentials beyond −0.3 V, due to the concomitant H_2 evolution reaction (HER) which essentially inhibits the electrodeposition process (see Table 2.1).

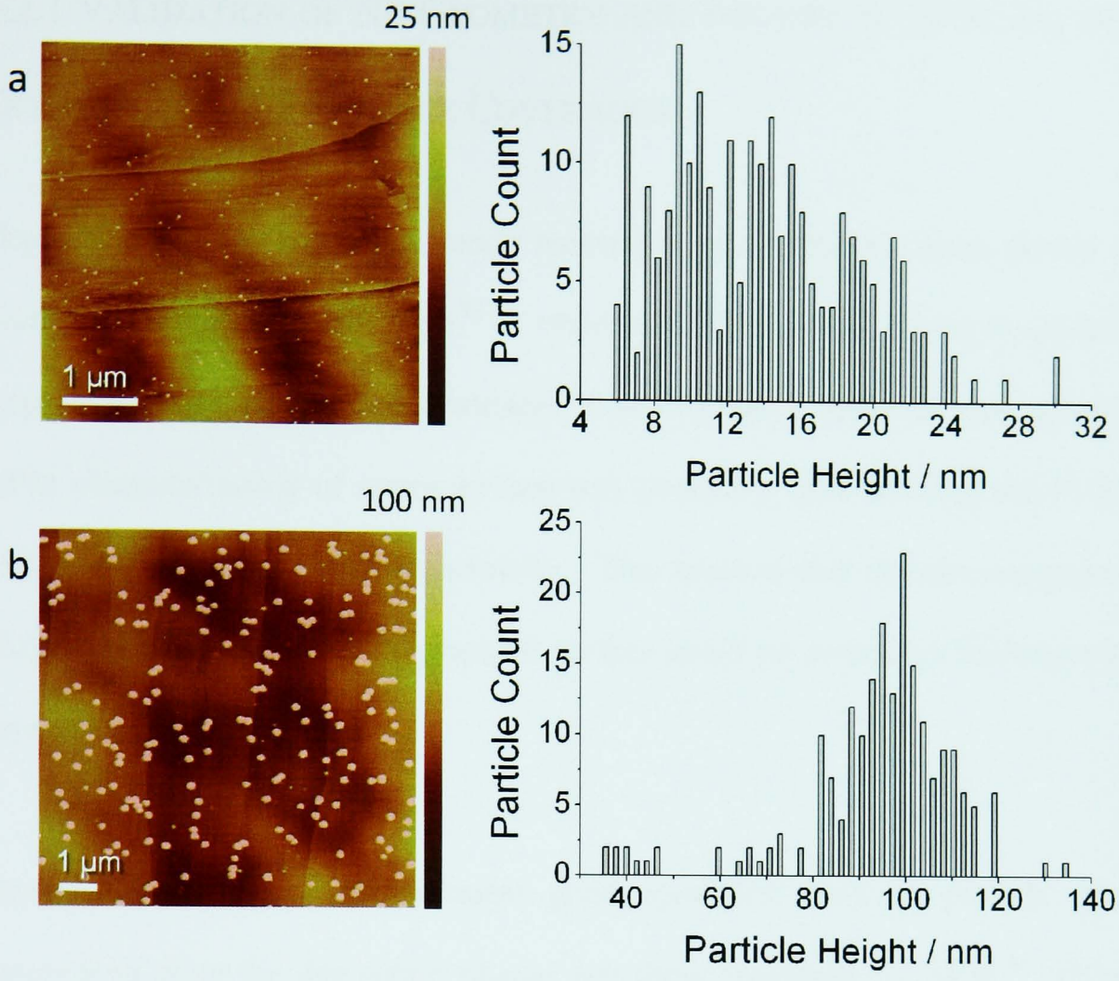

Figure 3.2 Tapping mode AFM images of Pt NPs deposited from a solution of 3 mM K_2PtCl_6 (0.25 M $HClO_4$) with a potential step from 0.5 to −0.2 V (10 s) on: a) PEDOT coated-HOPG and b) bare HOPG. Note the difference in the height scales for the two images

Table 3.1 Pt NP height and number of NPs for electrodeposition on native HOPG and PEDOT coated-HOPG

	Native HOPG		PEDOT	
Potential (V) applied (10 s) for deposition of Pt	NP height (nm)	Number of NPs (μm^{-2})	NP height (nm)	Number of NPs (μm^{-2})
−0.1			15 ± 9	5
−0.2	94 ± 17	2	14 ± 5	9
−0.3	41 ± 30	5	4 ± 3	69
−0.4			6 ± 4	86

3.2.1 Validation of NP Geometry and the use of AFM for the Estimation of NP Surface Coverages

Deposition of NPs and metal oxide nanowires on HOPG has been shown to occur preferentially at step edges[42] or where a reaction can be driven to decorate steps.[36,43] Since each cleaved surface of HOPG has a different step density, AFM characterisation of every surface was necessary after forming the Pt NP arrays and performing electrochemistry. This ensured that the electrocatalysis characteristic of each freshly prepared surface could be correlated directly with catalyst loading.

Previous studies have demonstrated good agreement between particle sizes determined from the deposition charge and those measured by AFM.[44] Other studies have calculated the Pt coverage of a surface using the charge of the Pt oxide stripping peak[45] and the charge of the hydrogen underpotential deposition (hydrogen adsorption; H_{ads}) peaks.[46] Determination of the Pt area using these classical methods was not always possible for the studies herein because of the small geometric area together with the low loading. Furthermore, the use of the charge passed during electrodeposition to estimate the amount of Pt electrodeposited was compromised by the HER when producing the smallest NPs.[31] However, under certain deposition conditions, where the charge from the Pt oxide stripping peak and/or H_{ads} peaks was measurable, the AFM approach to determine Pt surface coverage could be validated. For example, for NPs electrodeposited on HOPG from 3 mM K_2PtCl_6 (0.25 M $HClO_4$) at −0.3 V (10 s) so that a reasonably high surface coverage was produced (Figure 3.3a), it was

possible to show that the surface coverages estimated by AFM and CV (Figure 3.3b) were in good agreement.

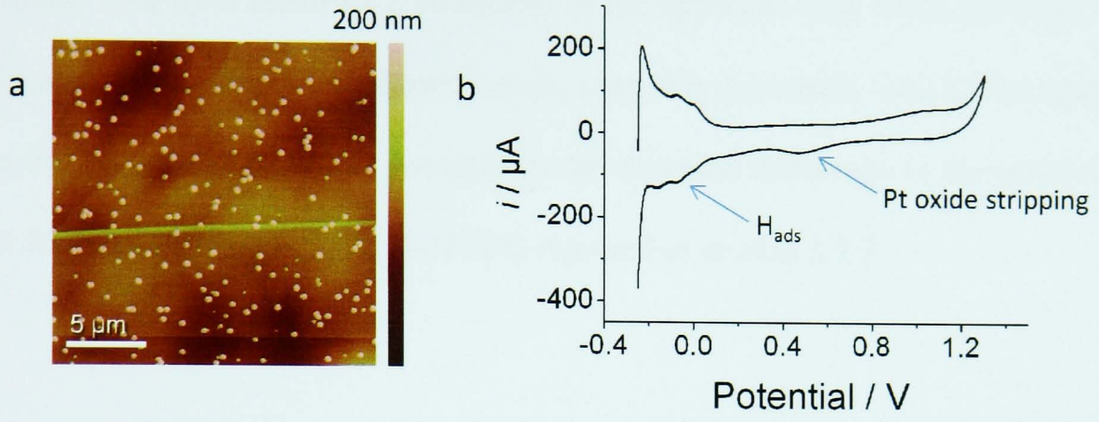

Figure 3.3 Tapping mode AFM image of Pt NPs deposited from a solution of 3 mM K_2PtCl_6 (0.25 M $HClO_4$) following a potential step from 0.5 to −0.3 V (10 s) on bare HOPG a) height image; b) CV to show both the Pt oxide stripping peak and H_{ads} peaks for the Pt-HOPG array electrode using 0.2 M H_2SO_4 with a scan rate of 0.5 Vs^{-1}

CV was performed immediately after deposition of NPs using a fresh aqueous solution containing 0.2 M H_2SO_4 with a scan rate of 0.5 V/s (Figure 3.3b). For this particular case, the surface coverages (active Pt area/electrode geometric area) determined were: Pt oxide stripping 4.8 ± 0.2 %, H_{ads} 5 ± 0.5 %, and AFM 4.2 ± 0.4 %. The AFM value is based on a spherical, rather than hemispherical, NP geometry for which the NP height is equivalent to the NP diameter rather than the NP radius; assumption of a hemispherical NP gave poor agreement. This was confirmed in two further experiments; thus, comparison of the AFM and CV data indicate NPs have a geometry that is close to spherical.

It was not possible to make surface area measurements based on voltammetric methods (Pt oxide stripping or hydrogen adsorption) on PEDOT-coated HOPG because of more sizeable background processes from the conducting polymer film. However, it is important to point out that the assumption of a

hemispherical, rather than spherical geometry for the Pt NPs, would mean using the AFM height data as the hemisphere radius and this would increase the surface area by a factor of 2 compared to the spherical case (with the height as the particle diameter). As shown herein, even this maximum level of uncertainty in the NP geometry cannot account for the dramatic difference in the activity of Pt NPs on HOPG and PEDOT-HOPG reported in section 3.2.3.

3.3 Electrocatalytic Activity of Pt-PEDOT and Pt-HOPG

Both MeOH and HCOOH oxidation were investigated to assess whether an intervening PEDOT film between HOPG and the Pt NPs had any effect on the resulting electrocatalytic activity, compared to bare HOPG, for similarly prepared NPs. The peak currents for these electrochemical processes during LSV at 50 mV s^{-1} were typically background corrected (by performing CV on the substrate with aqueous 0.2 M H_2SO_4 and subtracting this from the response with MeOH or HCOOH present) and normalised by the mean surface area of deposited platinum (determined by AFM image analysis as outlined in section 3.2.1). Because of the Pt aggregation issue on HOPG and the fact that each freshly cleaved surface can vary in terms of step density, the protocol for Pt electrodeposition was established by trial and error to create a Pt NP size on HOPG as close as possible to that on PEDOT.

3.3.1 Electrooxidation of Methanol

The activity of Pt-HOPG (Figure 3.4) and Pt-PEDOT (Figure 3.5) arrays for the electrooxidation of MeOH was investigated by performing LSV measurements

between 0.0 and +0.90 V in a solution containing 0.1 M MeOH and 0.2 M H_2SO_4. The LSV shape for MeOH oxidation, with a peak located at *ca.* +0.6 V (shown in Figure 3.4c and Figure 3.5c) was similar for both surfaces. The average MeOH oxidation peak current for Pt-HOPG was found to be 470 ± 160 μA cm^{-2} ($n = 3$; 1 SD). This value is comparable to previous studies of MeOH oxidation employing HOPG or GC as a support for Pt NPs.[47-49]

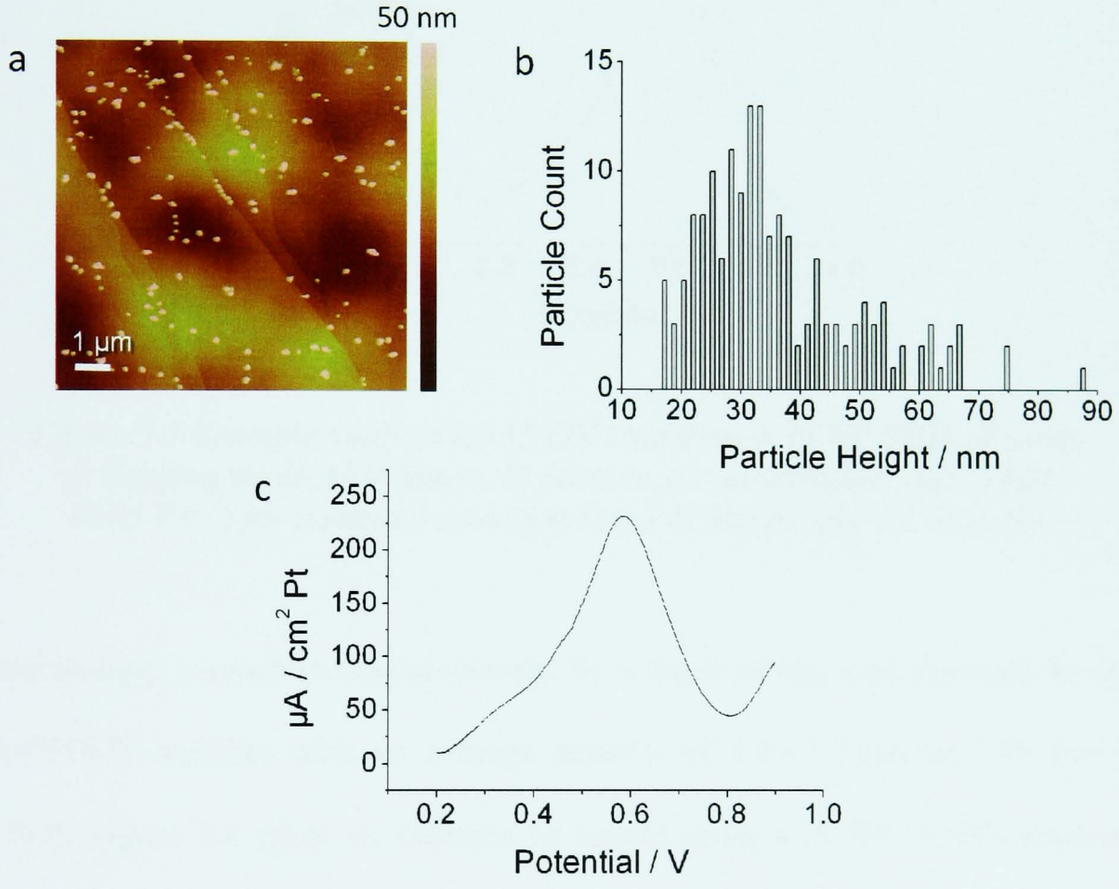

Figure 3.4 Example analysis for MeOH oxidation at Pt NP-HOPG. a) Tapping mode AFM image, b) particle size distribution, and c) LSV (0.05 Vs^{-1}) for methanol oxidation in 0.1 M MeOH and 0.2 M H_2SO_4

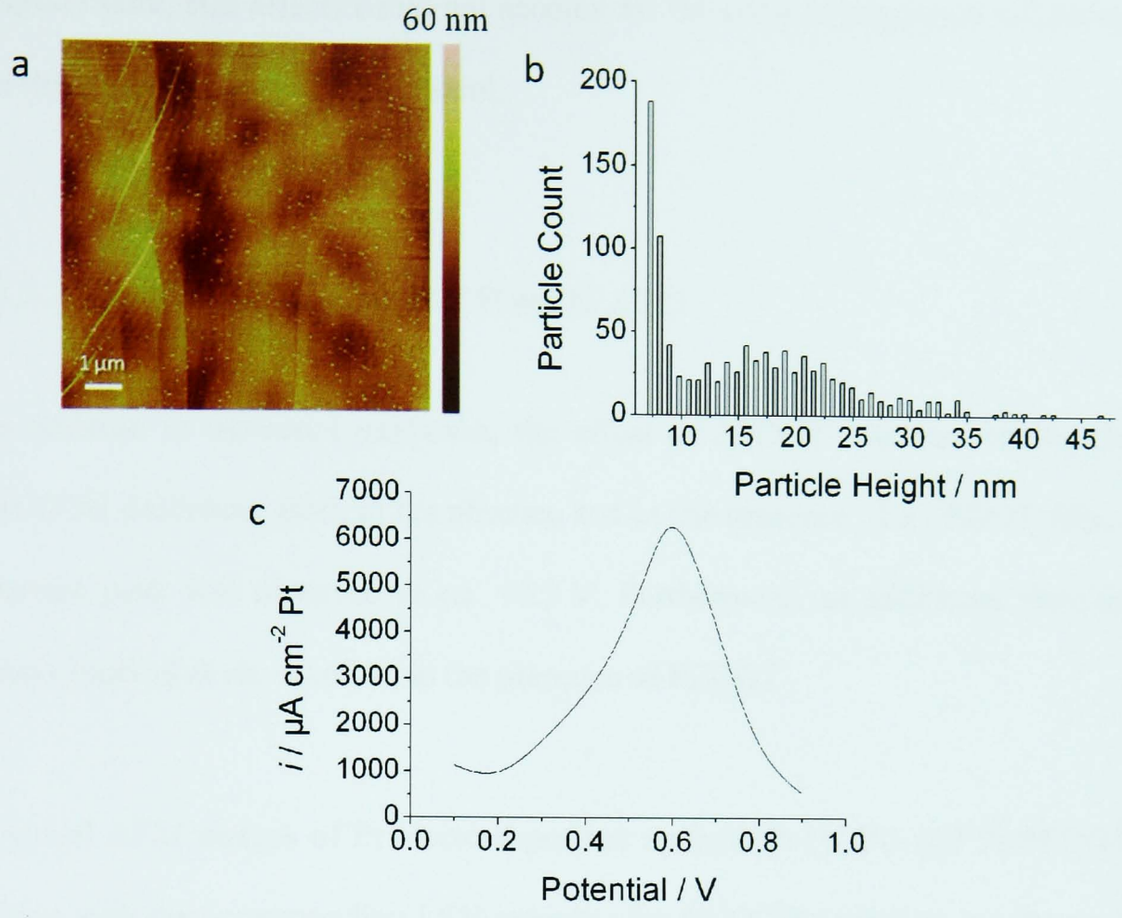

Figure 3.5 Example analysis for MeOH oxidation at Pt NP-PEDOT array. a) Tapping mode AFM image, b) particle size distribution, and c) LSV ($0.05\ V s^{-1}$) for methanol oxidation in 0.1 M MeOH and 0.2 M H_2SO_4

Interestingly, a much increased activity, by a factor of ten, was observed for the Pt-PEDOT surfaces with an average activity of 5.1 ± 1.2 mA cm^{-2} Pt ($n = 3$; 1 SD). Figure 3.4 gives an example of results using a Pt NP-HOPG substrate with an average NP diameter of 36 ± 13.5 nm (6.5 particles per square micrometer) and an activity of 230 µA cm^{-2} Pt (Figure 3.4c), whilst Figure 3.5c demonstrates the same reaction for a Pt NP-PEDOT surface with average NP diameter of 15.5 ± 7.7 nm (9.8 particles per square micrometer) and an activity of 6.3 mA cm^{-2} Pt. It is important to note that although the NPs differ in size by a factor of two, NP size effects are not anticipated for NPs of this size range.[50,51]

Furthermore, size effects could not account for the order of magnitude difference in the current density that is evident.

3.3.2 ELECTROOXIDATION OF FORMIC ACID

In addition to methanol oxidation, the effect of PEDOT was also studied for HCOOH oxidation. Both in the absence and in the presence of a PEDOT film, a current peak was observed at *ca.* +0.3 V. Furthermore, an additional shoulder was observed at *ca.* +0.65 V, in the presence of PEDOT.

Typical AFM images of Pt electrodeposited on both Pt-HOPG and Pt-PEDOT, along with the corresponding LSV response for HCOOH oxidation are shown in Figure 3.6 and Figure 3.7 respectively. Figure 3.6 shows a HOPG surface with an average Pt particle diameter of 13.0 ± 3.8 nm (four particles per square micrometer) with an activity of 7.9 mA cm^{-2} Pt at the peak at 0.3 V, whereas Figure 3.7 shows a Pt NP-PEDOT surface where the average particle diameter is 13.9 ± 5.1 nm (nine particles per square micrometer) with an activity of 5.8 mA cm^{-2} Pt at the peak at 0.3 V. From three separate experiments on each type of surface, the activities (and particle sizes) for Pt-HOPG and Pt-PEDOT were 6.5 ± 1.4 mA cm^{-2} Pt ($n = 3$; 1 SD; 16.8 ± 6.8 nm) and 5.9 ± 0.6 mA cm^{-2} Pt ($n = 3$; 1 SD; 14.4 ± 6.4 nm), respectively. Thus, in terms of the first peak the current density on Pt-PEDOT and Pt NPs was similar. However, a significant activity at higher potentials (above 0.5 V) was also observed in the presence of PEDOT which was negligible on native HOPG. Thus, the PEDOT support

greatly influences the electrocatalytic activity and the reasons for this are considered below.

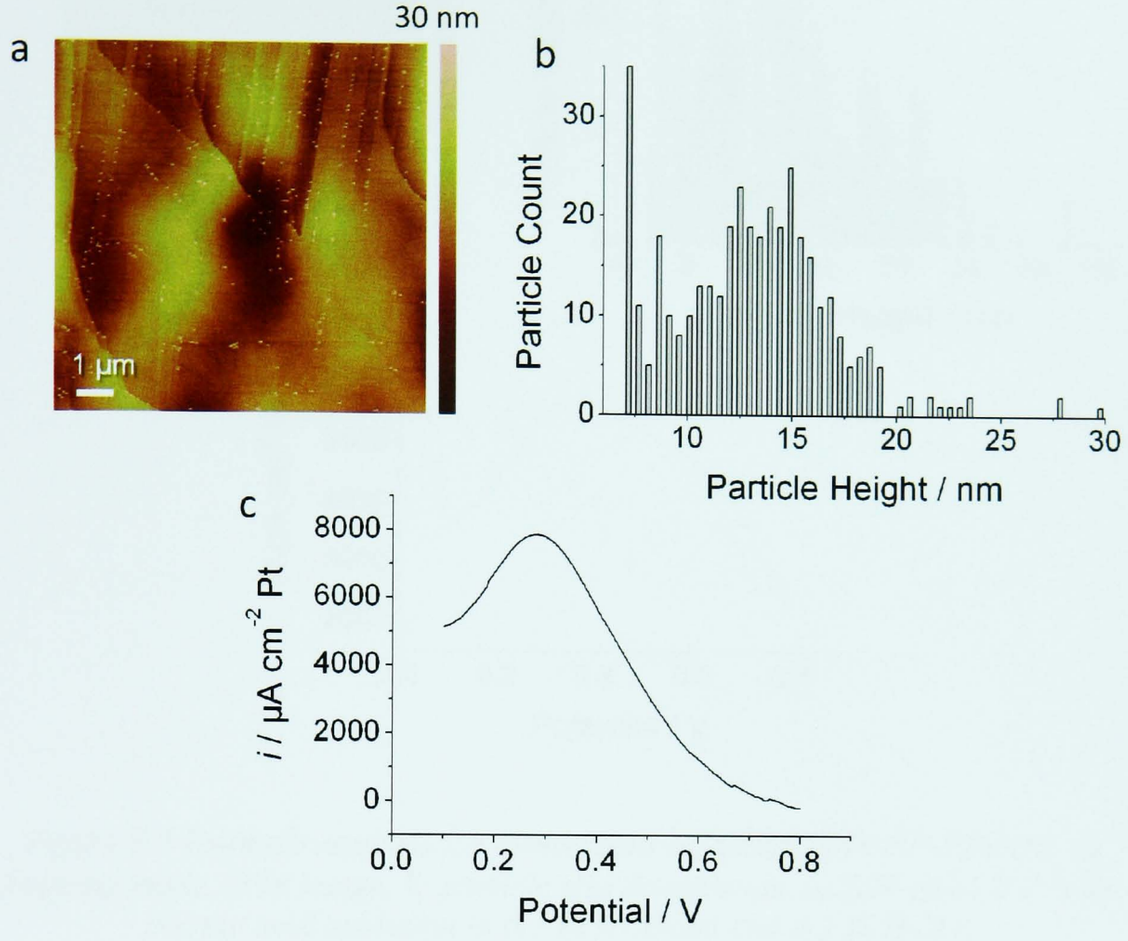

Figure 3.6 Example analysis for formic acid oxidation at Pt NP-HOPG. a) Tapping mode AFM image, b) particle size distribution, c) LSV (0.05 Vs^{-1}) for formic acid oxidation in 0.1 M HCOOH and 0.2 M H_2SO_4

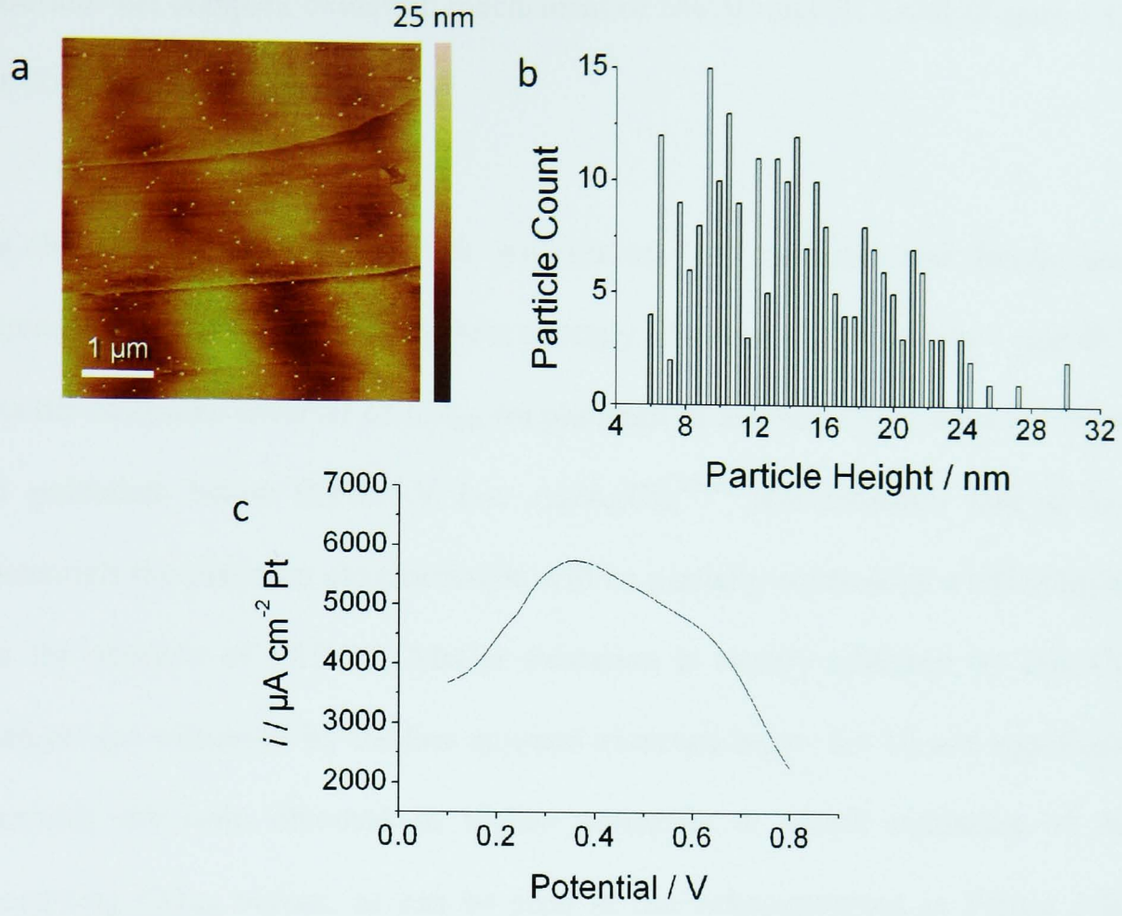

Figure 3.7 Example analysis for formic acid oxidation at Pt NP-PEDOT. a) Tapping mode AFM image, b) particle size distribution, c) LSV (0.05 Vs^{-1}) for formic acid oxidation in 0.1 M HCOOH and 0.2 M H_2SO_4

3.4 General Discussion

Based on the results described in the previous section, it is clear that the presence of a PEDOT film alters the electrocatalytic activity of HOPG supported platinum nanoparticles towards MeOH and HCOOH oxidation significantly. In the case of MeOH oxidation, the PEDOT film increases the current by an order of magnitude while keeping the shape of the voltammetric profile unaltered. On the other hand, for HCOOH oxidation, both the magnitude (currents) and the shape of the voltammetric profile are altered by the presence of a PEDOT film. To understand this markedly different effect of the PEDOT film, it is necessary to

consider the complex oxidation mechanism of MeOH and HCOOH (Figure 3.1), as discussed in section 3.1.

In the absence of PEDOT, it is well-known that methanol and formic acid decompose at low potentials to form strongly adsorbed CO (reactions 1 and 6).[52] As the oxidative removal of CO_{ads} on platinum in sulphuric acid does not occur at potentials below 0.4–0.5 V (vs. Ag/AgCl),[24,26] this indicates that at low potentials the platinum electrocatalyst will be partially covered by a CO adlayer. In the absence of PEDOT, MeOH oxidation is mostly inhibited by this CO adlayer (as witnessed by the low currents observed below 0.4 V) and significant currents are only obtained at higher potentials at which oxidation of the poisoning CO_{ads} occurs, as can be seen in the voltammogram in Figure 3.4c. HCOOH oxidation, however, can take place at a partially blocked surface (Figure 3.6c), indicating that HCOOH oxidation (through reaction 5 in Figure 3.1, as reaction 2 does not occur at low potentials) is less "site-demanding" than MeOH oxidation.

The presence of PEDOT does not significantly alter the voltammetric responses below 0.4 V: MeOH oxidation is still blocked (Figure 3.5c), while HCOOH oxidation (through reaction 5) still occurs at the same effective rate, indicating that the PEDOT film does not change the electrode processes at low potentials (i.e. the electrocatalyst is still blocked by CO_{ads}). At potentials above *ca.* 0.4 V (the potential at which CO_{ads} oxidation occurs), an enhancement in the electrocatalytic activity due to PEDOT can be seen in the large increase in MeOH oxidation peak currents (Figure 3.5c) and the emergence of a second oxidation feature in HCOOH oxidation (Figure 3.7c). This effect can be readily

explained by an increased CO oxidation rate (Figure 3.1, reaction 2) in the presence of PEDOT, reactivating previously blocked sites on the platinum surface at which MeOH or HCOOH can be turned over, and keeping these sites free by immediately oxidising any CO_{ads} formed through reactions 1 and 6.

There are multiple mechanisms through which PEDOT might enhance CO oxidation. One possibility is that PEDOT directly weakens the Pt–CO bond, either through modifying the electronic structure of the Pt NPs or by acting as a sink for CO, due to its lipophilicity. Alternatively, PEDOT might assist in activating water needed to oxidise CO. Finally, PEDOT may play a role in the NP deposition progress, steering it towards the formation of Pt NPs with different structural character which promotes CO oxidation. Unfortunately, it is not possible to distinguish between these mechanisms in the current study, but these would be worthwhile avenues to explore in the future in the view of the evident significant impact of PEDOT on the activity of Pt NPs. Furthermore, the role of PEDOT on the intermediates formed and product distribution also remains to be evaluated through further studies. This would be very challenging at the level of a small surface coverage of well-defined Pt NPs, but would be highly beneficial in terms of understanding and optimising this electrocatalytic system.

3.5 Conclusions

We have demonstrated that high densities of small isolated Pt NPs can be readily formed by electrodeposition at PEDOT-coated HOPG as a support. Thus, PEDOT acts not only as a conducting medium but also as a NP stabiliser

preventing agglomeration in a similar way to other polymers such as block copolymers.[52] In contrast, the formation of discrete NPs on native HOPG is much more difficult to achieve: aggregates of NPs are formed typically, with a preference for NP formation at characteristic sites, such as step edges.

A significant finding in this work is that PEDOT has a large effect on the electrocatalytic activity of the NP: the electrocatalytic oxidation of MeOH is an order of magnitude faster when PEDOT is employed as a support for Pt NPs, compared with similarly prepared Pt NPs on native HOPG (based on the peak current density response). Similarly, HCOOH oxidation is enhanced at high potentials. We have attributed these findings to an enhanced oxidation rate of adsorbed CO in the presence of PEDOT. Thus, CPs show great promise as support materials for enhancing specific electrocatalytic reactions.

Although we have demonstrated enhanced electrocatalytic activity of Pt-PEDOT arrays, further work is needed to fully elucidate the mechanisms operating, including which intermediates are formed.

Finally, we point out that AFM image analysis has proven valuable for determining the morphology, size and surface coverage of NPs, yielding results commensurate with voltammetric analysis of surface area. This was of particular importance in the present study, which often involved a low surface coverage of small NPs where more widely known techniques (charge from either the Pt oxide stripping peak or H_{ads}) sometimes proved difficult to implement.

3.6 REFERENCES

(1) Chan, K.-Y.; Ding, J.; Ren, J.; Cheng, S.; Tsang, K. Y. *J. Mater. Chem.* **2004**, *14*, 505.

(2) Steele, B. C. H.; Heinzel, A. *Nature* **2001**, *414*, 345.

(3) Daniel, M.-C.; Astruc, D. *Chem. Rev. (Washington, DC, U. S.)* **2003**, *104*, 293.

(4) Shan, J.; Tenhu, H. *Chem. Commun. (Cambridge, U. K.)* **2007**, 4580.

(5).Mayrhofer, K. J. J.; Blizanac, B. B.; Arenz, M.; Stamenkovic, V. R.; Ross, P. N.; Markovic, N. M. *J. Phys. Chem. B* **2005**, *109*, 14433.

(6) Scheijen, F.; Beltramo, G.; Hoeppener, S.; Housmans, T.; Koper, M. *J. Solid State Electrochem.* **2008**, *12*, 483.

(7) Sánchez-Sánchez, C. M.; Solla-Gullón, J.; Vidal-Iglesias, F. J.; Aldaz, A.; Montiel, V.; Herrero, E. *J. Am. Chem. Soc.* **2010**, *132*, 5622.

(8) Burda, C.; Chen, X.; Narayanan, R.; El-Sayed, M. A. *Chem. Rev. (Washington, DC, U. S.)* **2005**, *105*, 1025.

(9) Litster, S.; McLean, G. *J. Power Sources* **2004**, *130*, 61.

(10) Rao, V.; Simonov, P. A.; Savinova, E. R.; Plaksin, G. V.; Cherepanova, S. V.; Kryukova, G. N.; Stimming, U. *J. Power Sources* **2005**, *145*, 178.

(11) Zhao, Y.; Yang, X.; Tian, J.; Wang, F.; Zhan, L. *J. Power Sources* **2010**, *195*, 4634.

(12) Antolini, E.; Gonzalez, E. R. *Applied Catalysis A: General* **2009**, *365*, 1.

(13) Kulesza, P. J.; Chojak, M.; Karnicka, K.; Miecznikowski, K.; Palys, B.; Lewera, A.; Wieckowski, A. *Chem. Mater.* **2004**, *16*, 4128.

(14) Bensebaa, F.; Farah, A. A.; Wang, D.; Bock, C.; Du, X.; Kung, J.; Le Page, Y. *J. Phys. Chem. B* **2005**, *109*, 15339.

(15) Salavagione, H. J.; Sanchís, C.; Morallón, E. *J. Phys. Chem. C* **2007**, *111*, 12454.

(16) Choi, Y. S.; Joo, S. H.; Lee, S.-A.; You, D. J.; Kim, H.; Pak, C.; Chang, H.; Seung, D. *Macromolecules* **2006**, *39*, 3275.

(17) Selvaraj, V.; Alagar, M. *Electrochem. Commun.* **2007**, *9*, 1145.

(18) O'Mullane, A. P.; Dale, S. E.; Macpherson, J. V.; Unwin, P. R. *Chem. Commun. (Cambridge, U. K.)* **2004**, 1606.

(19) O'Mullane, A.; Dale, S.; Day, T.; Wilson, N.; Macpherson, J.; Unwin, P. *J. Solid State Electrochem.* **2006**, *10*, 792.

(20) Rice, C.; Ha, S.; Masel, R. I.; Waszczuk, P.; Wieckowski, A.; Barnard, T. *J. Power Sources* **2002**, *111*, 83.

(21) Wang, H.; Löffler, T.; Baltruschat, H. *J. Appl. Electrochem.* **2001**, *31*, 759.

(22) Wang, H.; Wingender, C.; Baltruschat, H.; Lopez, M.; Reetz, M. T. *J. Electroanal. Chem.* **2001**, *509*, 163.

(23) Léger, J. M. *J. Appl. Electrochem.* **2001**, *31*, 767.

(24) Lebedeva, N. P.; Koper, M. T. M.; Feliu, J. M.; van Santen, R. A. *J. Phys. Chem. B* **2002**, *106*, 12938.

(25) Lai, S.; Lebedeva, N.; Housmans, T.; Koper, M. *Top. Catal.* **2007**, *46*, 320.

(26) Markovic, N. M.; Ross, P. N. *Surf. Sci. Rep.* **2002**, *45*, 117.

(27) Capon, A.; Parsons, R. *J. Electroanal. Chem.* **1973**, *44*, 239.

(28) Capon, A.; Parsons, R. *J. Electroanal. Chem.* **1973**, *45*, 205.

(29) Wieckowski, A.; Sobkowski, J. *J. Electroanal. Chem.* **1975**, *63*, 365.

(30) Zhou, W.; Du, Y.; Zhang, H.; Xu, J.; Yang, P. *Electrochim. Acta* **2010**, *55*, 2911.

(31) Patra, S.; Munichandraiah, N. *Langmuir* **2008**, *25*, 1732.

(32) Kuo, C.-W.; Huang, L.-M.; Wen, T.-C.; Gopalan, A. *J. Power Sources* **2006**, *160*, 65.

(33) Vercelli, B.; Zotti, G.; Berlin, A. *J. Phys. Chem. C* **2009**, *113*, 3525.

(34) Pandey, R. K.; Lakshminarayanan, V. *J. Phys. Chem. C* **2010**, *114*, 8507.

(35) Penner, R. M. *J. Phys. Chem. B* **2002**, *106*, 3339.

(36) Li, Q.; Brown, M. A.; Hemminger, J. C.; Penner, R. M. *Chem. Mater.* **2006**, *18*, 3432.

(37) Bayati, M.; Abad, J. M.; Nichols, R. J.; Schiffrin, D. J. *J. Phys. Chem. C* **2010**, *114*, 18439.

(38) Lu, G.; Zangari, G. *Electrochim. Acta* **2006**, *51*, 2531.

(39) Brülle, T.; Stimming, U. *J. Electroanal. Chem.* **2009**, *636*, 10.

(40) Ventosa, E.; Palacios, J. L.; Unwin, P. R. *Electrochem. Commun.* **2008**, *10*, 1752.

(41) Day, T. M.; Unwin, P. R.; Macpherson, J. V. *Nano Lett.* **2006**, *7*, 51.

(42) Boxley, C. J.; White, H. S.; Lister, T. E.; Pinhero, P. J. *J. Phys. Chem. B* **2002**, *107*, 451.

(43) Walter, E. C.; Zach, M. P.; Favier, F.; Murray, B. J.; Inazu, K.; Hemminger, J. C.; Penner, R. M. *ChemPhysChem* **2003**, *4*, 131.

(44) Li, F.; Ciani, I.; Bertoncello, P.; Unwin, P. R.; Zhao, J.; Bradbury, C. R.; Fermin, D. J. *J. Phys. Chem. C* **2008**, *112*, 9686.

(45) Trasatti, S.; Petrii, O. A. *J. Electroanal. Chem.* **1992**, *327*, 353.

(46) Doña Rodríguez, J. M.; Herrera Melián, J. A.; Pérez Peña, J. *J. Chem. Educ.* **2000**, *77*, 1195.

(47) Cherstiouk, O. V.; Simonov, P. A.; Savinova, E. R. *Electrochim. Acta* **2003**, *48*, 3851.

(48) RodrIguez-Nieto, F. J.; Morante-Catacora, T. Y.; Cabrera, C. R. *J. Electroanal. Chem.* **2004**, *571*, 15.

(49) Bayati, M.; Abad, J. M.; Bridges, C. A.; Rosseinsky, M. J.; Schiffrin, D. J. *J. Electroanal. Chem.* **2008**, *623*, 19.

(50) Bergamaski, K.; Pinheiro, A. L. N.; Teixeira-Neto, E.; Nart, F. C. *J. Phys. Chem. B* **2006**, *110*, 19271.

(51) Chang, S. C.; Leung, L. W. H.; Weaver, M. J. *J. Phys. Chem.* **1990**, *94*, 6013.

(52) Kumar, S.; Zou, S. *Langmuir* **2008**, *25*, 574.

CHAPTER 4

QUANTITATIVE DETERMINATION OF THE ELECTRON TRANSFER ACTIVITY OF POLYCRYSTALLINE BORON DOPED DIAMOND USING INTERMITTENT CONTACT - SCANNING ELECTROCHEMICAL MICROSCOPY (IC-SECM)

ABSTRACT

Intermittent contact scanning electrochemical microscopy (IC-SECM) is a relatively new electrochemical imaging technique. Similar to conventional SECM, it employs an ultramicroelectrode (UME), however with this new imaging mode the tip is oscillated at a given frequency. On approach to a substrate this oscillation becomes dampened and thus can be used as a set point for imaging; providing and maintaining a known tip-substrate distance.

Polycrystalline boron doped diamond (pBDD) is an excellent electrode material, however fundamental studies on the micron scale are lacking. Using IC-SECM the whole surface of pBDD has shown to be active, with heterogeneity arising from boron dopant levels. This activity has been directly correlated to boron concentration via both Raman mapping and field emission scanning electron microscopy (FE-SEM), before current maps were converted to maps of standard rate constant, k^0, using finite element modelling.

k^0 values were determined for two concentrations of $Ru(NH_3)_6^{3+}$ and it was concluded that for regions of high boron concentration metallic conductivity occurs, however at the lower doped regions, a hopping mechanism dominates where a depletion of charge carriers may arise.

4.1 INTRODUCTION

The vast majority of solution phase electrode processes are heterogeneous in nature, with the electron transfer (ET) capabilities depending on a myriad of factors such as: (i) local chemical composition; (ii) local surface structure; (iii) local conductivity and (iv) redox properties of the molecule.[1-3] For some substrates, the entire electroactivity can be dominated by only a few active sites on the surface *e.g.* in the case of corrosion.[4,5] Typically electrochemical electron transfer measurements are made using *e.g.* variable scan rate cyclic voltammetry (CV) where the electron transfer characteristics are averaged for the whole surface. Often in these measurements, the surface is assumed to be homogeneously active which is unlikely to be the case in reality.

In order to truly understand the ET characteristics of the electrode/electrolyte interface it is important to be able to spatially map and quantify surface reactivity. Moreover, once the behaviour of the ET electrode system is better understood it may then be possible to re-engineer the material properties of the electrode in order to maximise ET performance. Quantifying local electrochemical activity is demanding and requires the use of high resolution scanned probe techniques such as scanning electrochemical microscopy (SECM), which employs a micro- or nano-electrode as the imaging probe. In order to accurately characterise and map the ET reaction rate the tip must be placed within a tip electrode radius of the substrate and the tip to substrate separation, d, must be accurately known, which is challenging. Attempts to address this have included the use of a non-interacting second redox mediator placed in solution or the development of hybrid techniques such as SECM-atomic force microscopy

(SECM-AFM), where the AFM component of the probe serves to independently determine and control *d*.

Polycrystalline BDD (pBDD) is an extremely useful electrode material due to its very wide potential window in aqueous solution,[6,7] low background currents,[8] resistance to both fouling and corrosion under both acidic and alkaline conditions[9-11] and stability at high temperatures and pressures.[12] The polycrystalline nature of the surface dictates that during the boron doping process different crystallographic grains take up differing amounts of boron resulting in heterogeneous doping of the surface[13-15] and a variation in the surface electrical properties.

There have been many attempts to map the electrochemical activity of the surface; however all have resulted in *qualitative* SECM current maps only. Furthermore, limitations in the techniques employed meant that direct quantitative correlation between surface electrochemical activity, grain structure and dopant density was not possible. SECM approach curve measurements were used in attempts to extract ET kinetics, however these were carried out in isolated areas, the size of which is controlled by the size of the SECM electrode and assumptions had to be made about the local dopant density. Hence, limitations in all the previous imaging techniques has led to a wide range of claims about the ET activity of pBDD, such as the surface is only active at grain boundaries or regions of the surface containing non-diamond like impurities or grains which have been sufficiently doped to become metal-like.

Here we show how by employing the recently developed intermittent contact (IC) -SECM technique, where *d* is unambiguously known and kept fixed during imaging, *i.e.* constant distance imaging, it is possible to extract values for the ET rate constant on a point-by-point basis (controlled by the size of the imaging tip). By using a small *d* (~ 1 μm) in conjunction with a small SECM tip radius (*a* ~1 μm) it is possible to map and quantify the ET activity of pBDD, grain by grain. This information can then be correlated with local boron dopant densities obtained using micro-Raman spectroscopy, enabling the origin of the heterogeneous electroactivity of pBDD to be resolved.

4.2 Intermittent Contact Scanning Electrochemical Microscopy (IC-SECM)

In brief, during IC-SECM[16], the oscillation amplitude of the tip UME is kept fixed at a constant damped value, associated with tip to surface contact, as shown in Figure 4.1a which shows how the free oscillation (oscillation frequency = 80 Hz) for a Pt disk UME, RG = 10 and *a* = 1.3 μm, changes as the tip approaches and then contacts the surface of pBDD. The sudden decrease in oscillation amplitude indicates contact of the tip with the surface. Note that as it is practically near impossible to obtain perfect alignment between tip and substrate, contact is likely from an edge of the glass sheath surrounding the Pt disc UME. This is in general preferred as it avoids direct substrate electrode to tip electrode contact, which typically results in shorting.

During imaging, the tip scans one line in "*contact*" with the surface, collecting information not only on the tip current signal but also on the substrate

topography (via the distance the tip needs to move in order to keep the damped oscillation constant). On the pass back the tip can be set to acquire current data at a distance defined by the user and pertinent to the size of electrode employed. In this work, Pt disk UMEs (a = 0.9 – 1.3 μm) were fabricated in-house from Wollaston wire using established procedures.[17] The radii of the UME employed in this work were selected because of grain sizes (5 – 40 μm diameter) when employing a pBDD sample of 500 μm thick. Typical free oscillation amplitudes of ~200 nm were employed at frequencies of 80 Hz.

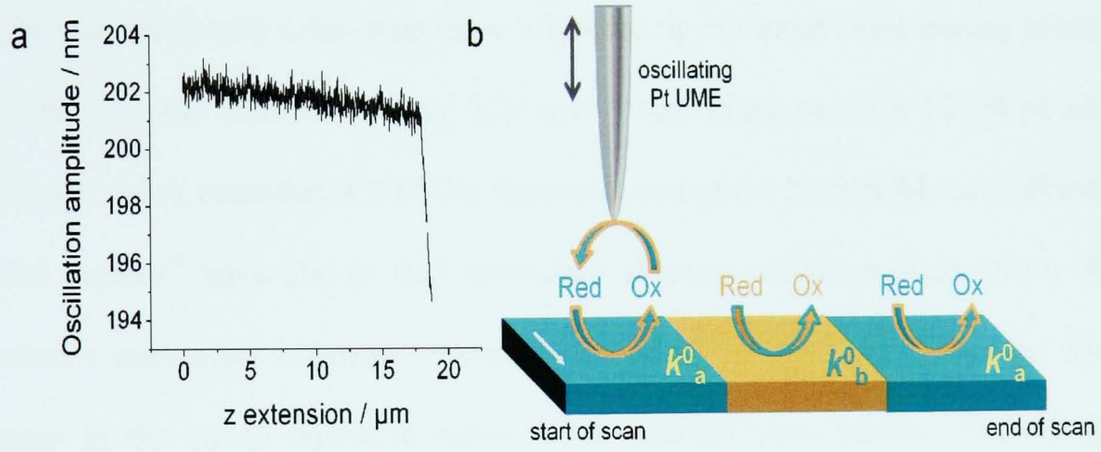

Figure 4.1 a) An example of the oscillation signal with dampening as the tip approaches the substrate b) schematic of IC-SECM in substrate generation – tip collection (SG-TC) mode

Figure 4.1b shows a schematic highlighting application of IC-SECM in substrate generation – tip collection (SG-TC) mode, to the heterogeneously active pBDD surface. Different grains contain different boron dopant levels, each effectively characterised by an intrinsic rate constant, k^0, which is dependent on the number and mobility of charge carriers[18] at the surface of the pBDD. Furthermore, non-

diamond like impurities, if present, will also show ET activity characterised with their own k^0.

Figure 4.2 shows typical 70 μm x 70 μm IC-SECM SG-TC images of the pBDD surface for the tip collection of 5 mM $Ru(NH_3)_6^{2+}$ at fixed d values of (a) 1 μm and (b) 2 μm for a =1.3 μm. The substrate is biased at -0.4 V versus Ag/AgCl to drive $Ru(NH_3)_6^{3+}$ reduction at a diffusion-limited rate, whilst the tip was held at 0.0 V versus Ag/AgCl to collect $Ru(NH_3)_6^{2+}$ at a diffusion-limited rate. All of the IC-SECM images in this work were obtained by taking a reading every 2 μm (the step size) with a sub-step (how often the tip is repositioned during scanning – 'feeling' the substrate) every 0.25 μm. Also displayed is a FE-SEM image (Figure 4.2c), recorded at 2 kV, in the same area of the IC-SECM scan. Previous EM studies[19] have shown that secondary electron emission yields from BDD reach a maximum at boron concentrations of 10^{19} – 10^{20} cm^{-3}, thus the darker areas in the image represent zones which contain more boron. The FE-SEM image of the polished pBDD surface (~ 1 - 2 nm surface roughness within a grain and ~ 1-5 nm across grains as revealed by AFM) shows that the surface is heterogeneously doped, with certain grain structures taking up less boron than surrounding areas.

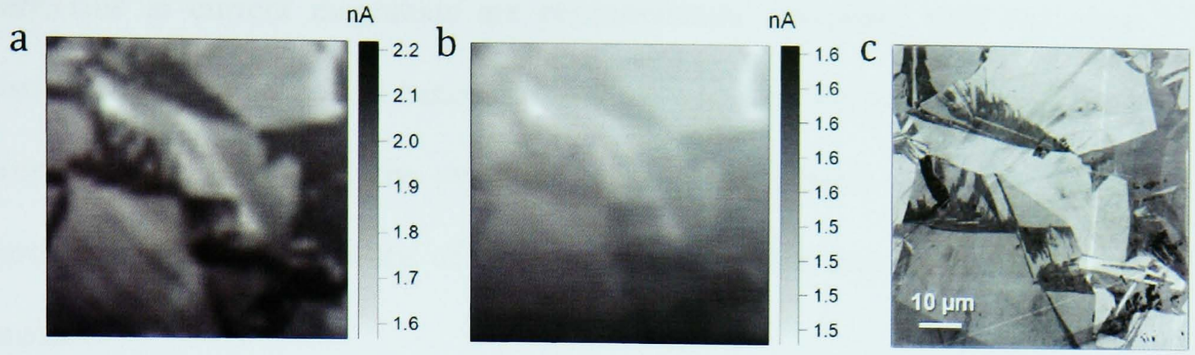

Figure 4.2 70 µm × 70 µm IC-SECM SG-TC mode images for the collection of 5 mM $Ru(NH_3)_6^{2+}$ electrogenerated at the surface of pBDD (held at -0.4 V) at tip-substrate separations of a) 1 µm and b) 2 µm. c) Corresponding FE-SEM image of the same area scanned by the IC-SECM tip

Clearly evident is the close correlation between the FE-SEM image of the grain structure in Figure 4.2c and the IC-SECM tip current map (in SG-TC mode) of the surface electroactivity (especially in Figure 4.2a). Electrochemical images which clearly reveal grain structure have never been observed before during the electrochemical mapping of pBDD. Even subtle current differences within grains are apparent. In essence, qualitatively, the areas which contain higher levels of boron show enhanced tip current *i.e.* increased electroactivity. It is also clear that the electrochemical resolution of the image is enhanced by employing smaller tip-substrate imaging separations and highlights one of the advantages of this technique *i.e.* the ability to accurately control and maintain the tip-substrate separation. This is essential when using high resolution tips, even a difference in d of 1 µm, for a tip characterised by a = 1.3 µm, makes an enormous difference to the resolution of the electrochemical image as evidence by the difference between Figure 4.2a and b.

Previous SECM studies have associated increased areas of current with either areas of inter-granular non-diamond-like (sp^2) carbon or metallic-like regions of the surface.[20-23] From these images it is already strikingly clear that the

variations in current magnitude are predominantly associated with the grain structure of the surface and hence boron dopant levels. Further information on boron dopant levels and the presence of sp^2 contaminants was obtained by recording micro-Raman maps of the surface in the same area as the IC-SECM images.

Figure 4.3a shows the Raman map for the integrated area under the peak for the zone centre optical phonon (~ 1332 cm^{-1}) associated with sp^3 carbon. As the boron concentration increases the peak shifts to lower wavenumbers, with a smaller integrated peak area.[24,25] For the image in Figure 4.3a, a Raman spectrum was recorded at every 1.2 μm over the wavenumber range 900-1800 cm^{-1}. The spot size employed was < 5 μm; however the intensity of this is much greater in the centre. The darker zones in the image are thus associated with higher boron content and correlate with the data recorded in Figure 4.2.

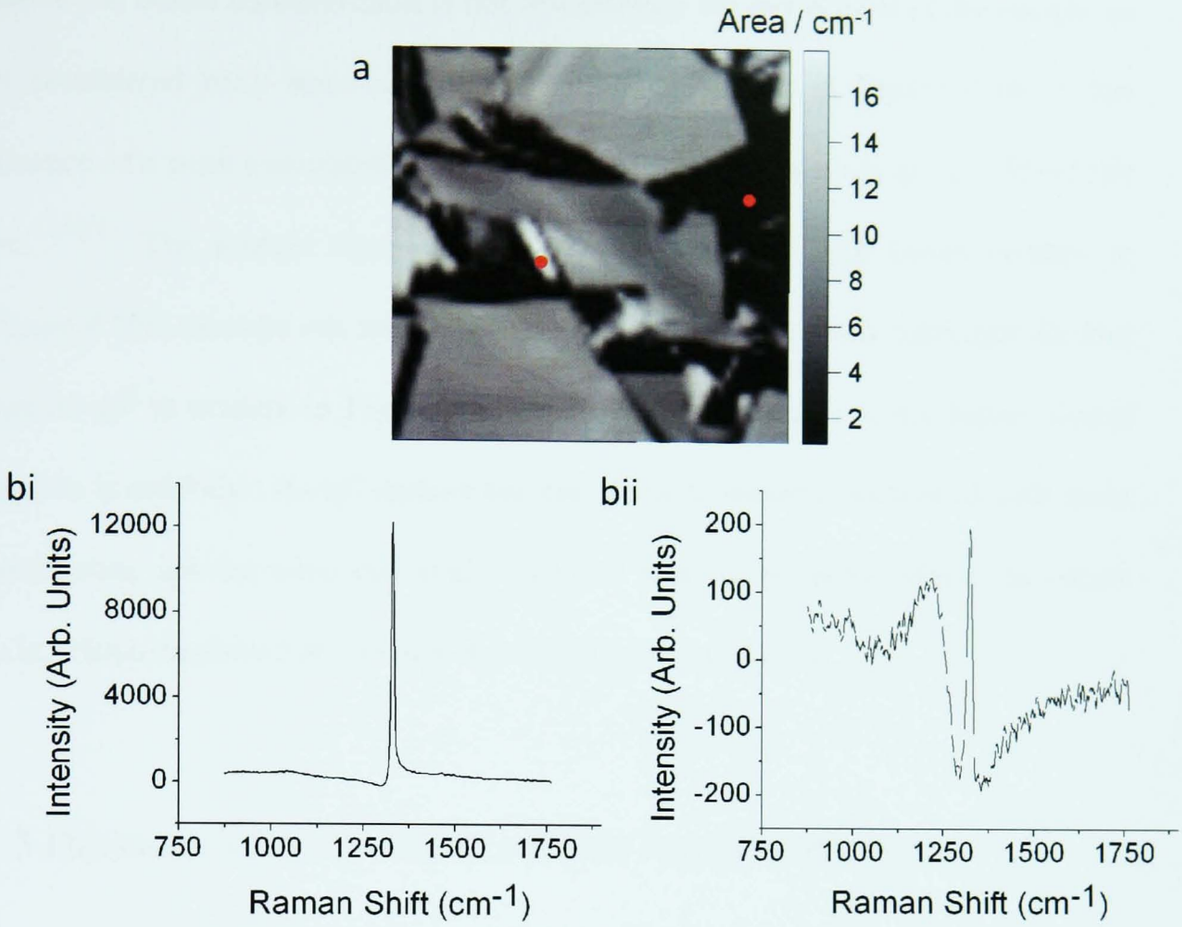

Figure 4.3 a) Raman map showing the integrated area under the peak for the zone centre optical phonon (~ 1332 cm^{-1}) b) Spectra from the points on the map (•) in the region for i) lowest concentration of boron ii) highest concentration of boron

To provide further information on the boron doping levels, individual spectra were analysed in regions of the sample which contained the lowest and highest boron levels (as indicated by the red dots on Figure 4.3a). Both spectra (Figure 4.3bi and bii) show a diamond (sp^3) peak centred at 1332 cm^{-1}, the asymmetry of the peak (Fano resonance) indicates that in both areas the boron concentration, [B], must be $\geq 10^{20}$ atoms cm^{-3}. As the boron concentration increases the peak becomes more asymmetrical. In terms of electrical characteristics, p-type semi-conducting behaviour is expected for [B] < 1 x 10^{19} atoms cm^{-3}, as [B] increases from 1 x 10^{19}- 3 x 10^{20} cm^{-1} electrical conduction is via a hopping mechanism, until at [B] $\geq$ 3 x 10^{20} atoms cm^{-3} the material exhibits metal-like conductivity.[26]

Hence the boron concentration is not low enough for any region of the sample to be considered truly semi-conducting. Also important, in Figure 4.3bi is the absence of a peak associated with non-diamond-like sp^2 carbon at *ca.* 1350-1580 cm^{-1}.[27,28] The Raman signal associated with the very high boron content in Figure 4.3bii swamps out any potential signal from sp^2 carbon, although the fact that no sp^2 is evident in Figure 4.3bi indicates its presence in the higher doped regions is unlikely. As sp^2 carbon has also been previously associated with grain boundaries, spectra were also analysed for at least 10 grain boundaries in Figure 4.3a. None displayed any evidence of significant sp^2carbon.

4.3 Determination of the Standard Rate Constant, K^0

To quantify the tip currents recorded in Figure 4.2a, finite element (FEM) simulations were employed to simulate the theoretical current response as a function of k^0 using Butler-Volmer kinetics. Modelling was performed using the commercial FEM package COMSOL Multiphysics 3.5a (COMSOL AB, Sweden) with the Matlab Interface (Release 2010a) (Mathworks Inc., Cambridge, UK). Typically, 100,000 triangular mesh elements were used in each simulation with the greatest mesh resolution at the pBDD and Pt UME boundaries. For the $Ru(NH_3)_6^{3+}$ species the following one-electron oxidation reaction was considered (Equation 4.1)

$$Ru(NH_3)_6^{3+} + e^- \underset{k_b}{\overset{k_f}{\rightleftharpoons}} Ru(NH_3)_6^{2+} \qquad (4.1)$$

where k_f and k_b are the rate constants of electron transfer for the reduction and oxidation reactions respectively.

For this reaction the following time-dependent diffusion equation was solved (Equation 4.2):

$$\frac{\partial c_i}{\partial t} = D_i\left(\frac{\partial^2 c_i}{\partial r^2} + \frac{1}{r}\frac{\partial c_i}{\partial r} + \frac{\partial^2 c_i}{\partial z^2}\right) \tag{4.2}$$

where c_i (mol cm^{-3}) and D_i (cm^2 s^{-1}) represent the concentration and diffusion coefficient of species i ($Ru(NH_3)_6^{3+}$) and r and z are the coordinates in the directions radial and normal to the centre of the Pt UME surface.

In order to simplify the model, D_i was assumed to be identical for both oxidation states of the redox couple, to allow each simulation to be formulated with only one species, where D ($Ru(NH_3)_6^{3+/2+}$) = 8.8 x 10^{-6} cm^2 s^{-1}.[29]

The finite element method[30] was used to determine the current response at the Pt UME in the SG-TC mode by solving the time-dependent diffusion equation on the interior of the domain depicted in Figure 4.4a subject to the boundary conditions of the system, which are summarised in Table 1.

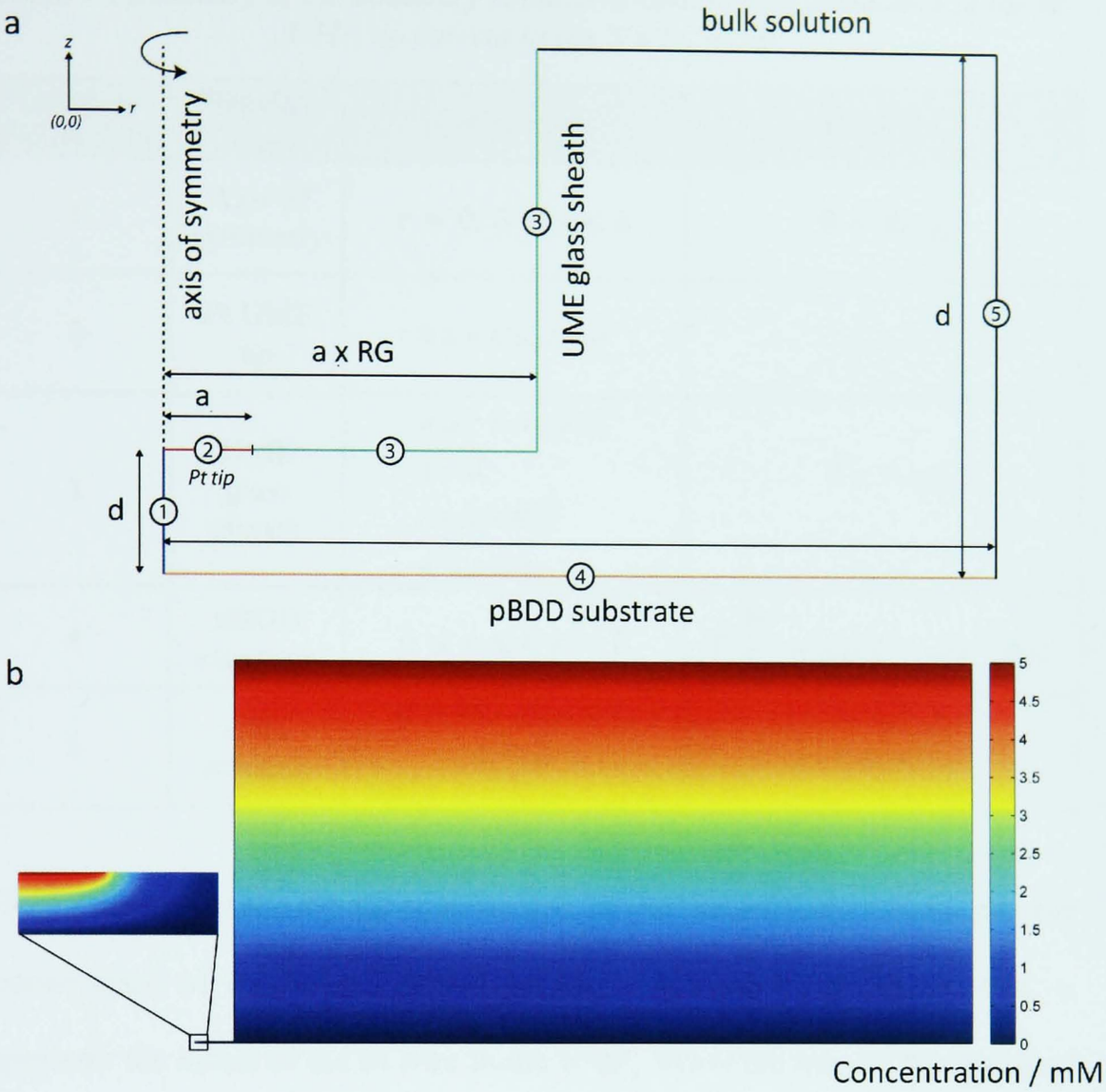

Figure 4.4 a) 2D simulation domain for the SG-TC setup (not to scale). d between Pt UME and pBDD is typically ~ 1 µm; the exact value is known and used in the simulation. a for the Pt UME is set to match that determined experimentally. The RG value is 10 and the length and height of the simulation domain is 200 µm. (b) Simulated steady-state diffusion-limited concentration profile of $Ru(NH_3)_6^{3+}$ in the SG-TC mode with the overpotential, $\eta = 0.235$ V. The inset shows the concentration profile at the Pt UME in more detail

Table 4.1 Summary of the boundary conditions used for the simulation of the Pt UME tip current in the SG/TC mode

Label in Figure 5.4a	Boundary type	Coordinates	Equation
1	Axis of symmetry	$r = 0, 0 \leq z \leq h$	$0 = \nabla c.\underline{n}$
2	Pt UME tip	$0 \leq r \leq a, z = d$	$c = c^*$
3	UME glass sheath	$a \leq r \leq a \times RG,$ $z = d$ $r = a \times RG$ $d \leq z \leq h$	$0 = \nabla c.\underline{n}$
4	pBDD substrate	$0 \leq r \leq l, z = 0$	$D\frac{\partial c}{\partial z} = k_b(c^* - c) - k_f c$
5	Bulk solution	$a \times \mathrm{RG} \leq r \leq l,$ $z = h$ and $r = l, 0 \leq z \leq h$	$c = c^*$

where $\underline{n}$ represents the inward-pointing unit normal vector and c^* represents the concentration of $Ru(NH_3)_6^{3+}$ added initially. As shown in Figure 4.4a, a represents the radius of the Pt wire in the UME, RG is the ratio of the radius of the entire electrode to that of the Pt wire, d is the separation between the Pt UME and the pBDD substrate and l and h are the width and height of the simulation box respectively. The simulations were carried out with RG = 10, l = 200 μm and h = 200 μm.

The value of a was calculated using Equation 4.3:

$$a = \frac{i_{\mathrm{lim}}}{4nFDc} \tag{4.3}$$

where n is the number of electrons transferred, F is Faraday's constant.

The observed limiting current (i_{lim}) was recorded in a CV taken before each IC-SECM scan. A CV was also taken after each scan to ensure there was no tip deterioration. Similarly d was determined from IC-SECM approach curves, recorded before each scan.

The Butler-Volmer equation[31] (Equation 4.4 and Equation 4.5) was used to describe ET kinetics at the pBDD electrode/solution interface, for which

$$k_f = k^0 \exp\left[\frac{-\alpha\eta F}{RT}\right] \tag{4.4}$$

$$k_b = k^0 \exp\left[\frac{(1-\alpha)\eta F}{RT}\right] \tag{4.5}$$

where R is the ideal gas constant, T is the temperature, α is the transfer coefficient and η is the overpotential. Simulations were carried out for T = 298 K, as employed in the experiments and α = 0.5.

The Butler-Volmer relationship describes how the applied potential to the electrode affects the kinetics and in turn will influence the measured current. Electron transfer kinetics will determine the rate that the electrode can reduce or oxidise a species. Consequently, faster electron transfer kinetics will produce higher currents than a reaction occurring with slower electron transfer kinetics. However, as the applied potential is increased to extreme driving forces (large η), the current may become limited by mass transfer rates to the electrode. It is to be noted that the overpotentials selected for imaging throughout this thesis were those from kinetically limited regions, determined by employing CV before imaging.

Figure 4.4b shows the steady-state diffusion-limited concentration profile of the tip generated $Ru(NH_3)_6^{3+}$ in SG-TC mode. The substrate is driven at a high overpotential, η = 0.235 V, so that $Ru(NH_3)_6^{3+}$ is completely reduced to $Ru(NH_3)_6^{2+}$ at the pBDD substrate, which is then subsequently collected at the Pt UME tip.

A series of simulations were carried out whereby k^0 was consistently varied and the limiting Pt UME tip current for each k^0 was obtained, producing a sigmoidal plot of $\log(k^0)$ vs. limiting current for each set of the experimental conditions (Figure 4.5). A Boltzmann curve was then fitted to the simulation data to find an analytical expression for the curve of the form;

$$i = A_2 + \frac{A_1 - A_2}{1 + \exp\left(\frac{\log(k^0) - x_0}{dx}\right)} \tag{4.6}$$

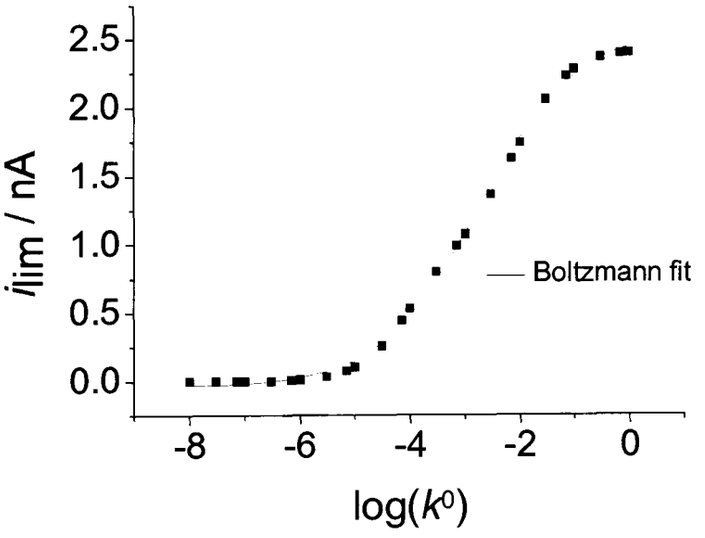

Figure 4.5 Plot of simulated Pt UME tip limiting current versus $\log(k^0)$ for k^0 values in the range 1 x 10^{-8} – 1 cm s^{-1}. A Boltzmann function is fitted to the data to give an analytical expression for i_{lim} as a function of k^0 to enable IC-SECM maps of current to be converted to k^0 maps

Equation 4.6 was employed to obtain an expression for k^0 as a function of i_{lim}. The IC-SECM maps could then be re-plotted in terms of k^0 versus tip x,y position to obtain quantitative information on ET activity across the heterogeneously doped surface.

4.4 Maps of Standard Rate Constant, K^0

Figure 4.6a shows the resulting k^0 map as a function of tip *x,y* position, for a fixed *d* of 1 μm, extracted from the raw limiting current data shown in Figure 4.2a. This is the first time that SECM has been utilised to extract k^0 on a point-by-point basis on a heterogeneously active electrode surface. This is only possible as the tip-substrate separation is unambiguously known at all points during the scan. Figure 4.6a, k^0 ranges from a value of 4.6×10^{-3} ($\pm 0.6 \times 10^{-3}$) cm s^{-1} in the most active areas to 0.3×10^{-3} ($\pm 0.1 \times 10^{-3}$) cm s^{-1} in the least active areas. These values and additional k^0 values quoted are based upon 1 % of the highest and 1 % lowest values with the corresponding standard deviation.

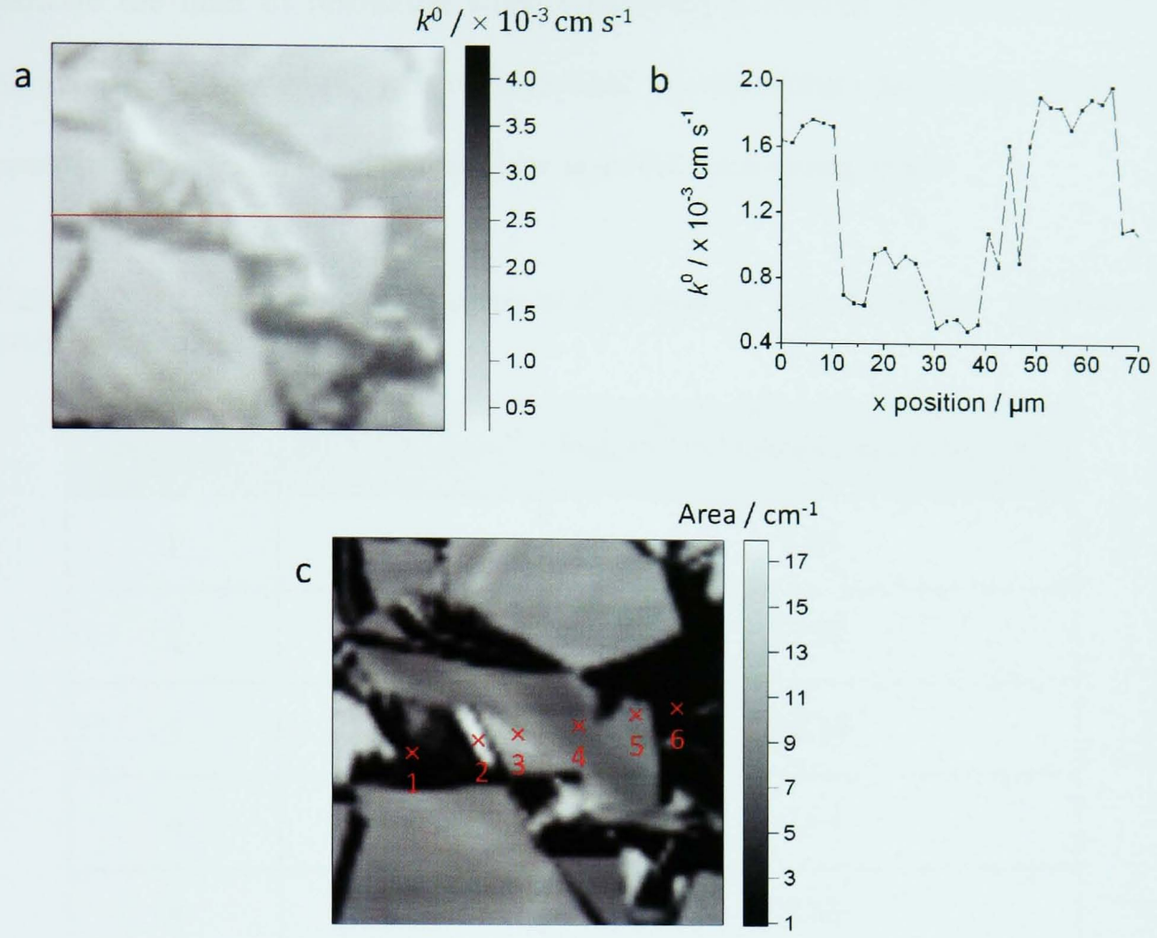

Figure 4.6 a) IC-SECM map of k^0 values (obtained from the raw data in Figure 4.2a). b) Cross sectional plot of k^0 across the red line section shown in Figure 4.6a illustrating the variation in k^0 both within a single grain and across grains c) Raman peak integration is compared with standard rate constant values in the regions marked (×) (see Table 4.2 for this comparison)

A further indication of how k^0 varies from grain to grain is given by the line cross section (Figure 4.6b). Points from the k^0 cross section have been correlated with the same selected areas on the micro Raman map (Figure 4.6c), as indicated by the red crosses (×). The corresponding values of k^0 and integrated peak area under the 1332 cm^{-1} Raman peak have been tabulated in Table 4.2 and this shows that the highest k^0 values occur at the more heavily doped regions of the surface (as determined from the lower integrated peak areas). The only exception to this trend is at position 2, where the Raman signal indicates the lowest concentration of boron (but still above 10^{20} cm^{-1}) but not the lowest k^0 value. This could

indicate the limit of resolution when employing IC-SECM with the Pt UME dimensions in this work, where diffusional overlap occurs and hence there is contribution towards the electroactivity from the surrounding areas.

Table 4.2 *A table to show the values of k^0 compared with the Raman integrated peak area (1332 cm^{-1})*

Position	k^0 / × 10^{-3} cm s^{-1}	Raman / integrated peak area (cm^{-1})
1	1.85	1.31
2	0.87	17.02
3	0.47	12.14
4	0.93	7.34
5	0.65	8.33
6	1.76	1.49

To further prove the validity of the technique 70 μm x 70 μm IC-SECM images were recorded in a different area of the sample at d = 1 μm, for a = 0.9 μm. For these images the concentration of $Ru(NH_3)_6^{3+}$ in the bulk solution was decreased from 5 mM to 1 mM to see if the effect of challenging the surface with less redox active species would have any effect on the measured k^0 values. For a pure metal there should be no effect. Here, the substrate was held at -0.21 V versus Ag/AgCl which corresponds to η = -0.052 V, Figure 4.7a, whilst the tip was held at 0.0 V versus Ag/AgCl to oxidise $Ru(NH_3)_6^{2+}$ at a diffusion-limited rate. Figure 4.7b shows the corresponding k^0 map, extracted from the experimental tip limiting currents values whilst Figure 4.7c and d show the micro-Raman map of integrated peak area and FE-SEM image, respectively, recorded under identical

conditions as for Figure 4.2c and Figure 4.3a. Individual micro-Raman spectra recorded in the highest and lowest integrated peak areas again both show a Fano resonance indicating that the minimum [B] is $\geq 10^{20}$ atoms cm^{-3}.

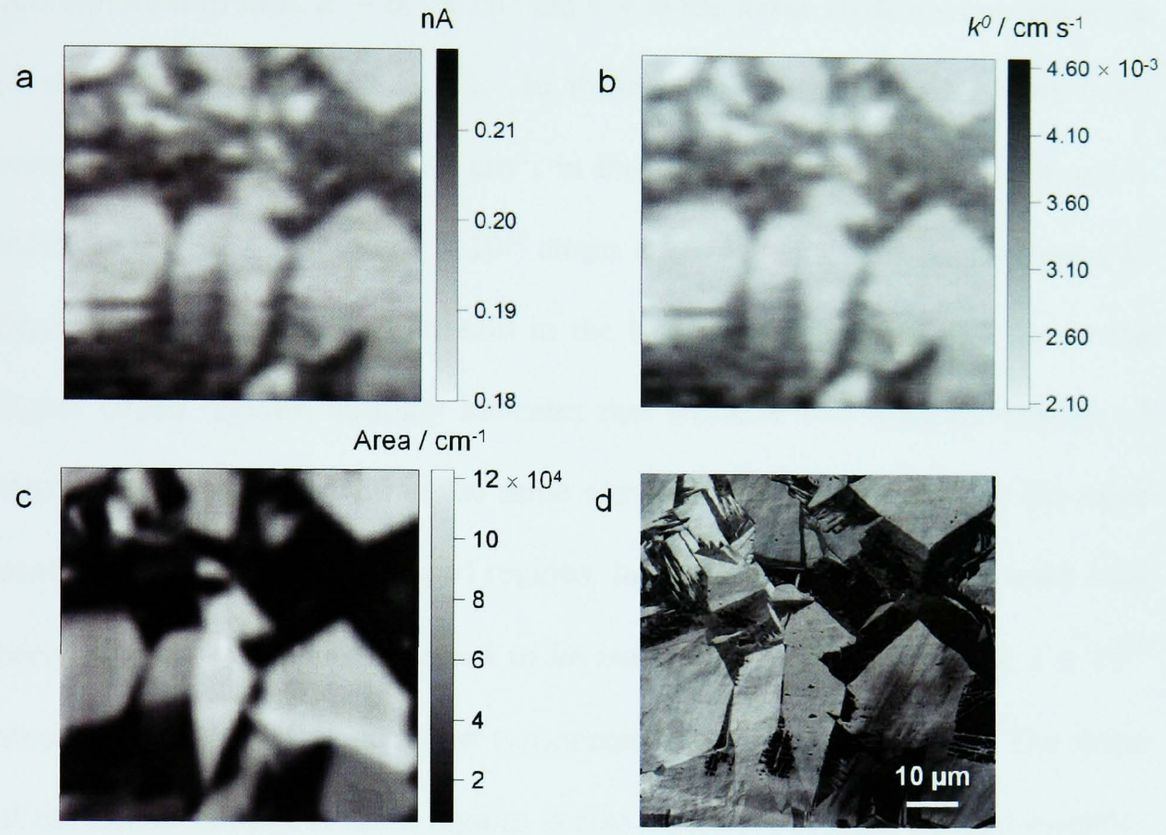

Figure 4.7a) 70 µm × 70 µm IC-SECM SG-TC mode images for the collection of 1 mM $Ru(NH_3)_6^{2+}$ electrogenerated at the surface of pBDD. The substrate was held at η = -0.052 V. b) k^0 maps extracted from the limiting current maps c) Raman map to show the integrated area of the 1332 cm^{-1} peak and d) FE-SEM image

As before the higher tip current regions correlate exactly with the higher doped boron regions as evidenced from both the micro-Raman and FE-SEM maps. The simulation derived k^0 values for $Ru(NH_3)_6^{3+}$ reduction at the substrate electrode range from 2.1 x 10^{-3} (± 0.1 x 10^{-3}) cm s^{-1} (minimum) to 4.5 x 10^{-3} cm s^{-1} (maximum).

Interestingly, for the reduction of $Ru(NH_3)_6^{3+}$ at 1 mM and 5 mM concentrations, the same value of k^0 *ca.* 4 x 10^{-3} cm s^{-1}, was determined in the regions shown to

be the most highly doped with [B], from Raman spectroscopy. However, for the lower doped [B] regions there was a significant difference in k^0, by a factor of 5, when comparing the experiments performed with the highest redox mediator concentration (5 mM, $k^0 \sim 0.3 \times 10^{-3}$ cm s^{-1}) to the lower mediator concentration (1 mM, $k^0 \sim 2.1 \times 10^{-3}$ cm s^{-1}). In these regions the presence of the Fano resonance centred around 1332 cm^{-1}, in the Raman spectra (800 – 1800 cm^{-1}) indicates that [B] is at least 1×10^{20} atoms cm^{-3}. However, the fact we see a k^0 dependence on redox concentration in the lower doped regions, but not in the higher doped regions, strongly indicates that we have two different regions of electronic conductivity within the same sample. We propose that for the more conducting and higher [B] doped regions, the grains are sufficiently doped with boron that they can be considered to be metallic in nature i.e. [B] $\geq 3 \times 10^{20}$ atoms cm^{-3}, and thus do not show a concentration dependence on k^0. The shape of the Raman spectra in these regions is also indicative of highly doped metallic-like conducting diamond.[32] However, in the lower [B] doped regions the grains are not doped sufficiently to be metallic like, but the presence of the Fano signal in the Raman indicates that [B] lies in the range $1 \times 10^{20} - 3 \times 10^{20}$ B atoms cm^{-3}. In this doping region, the BDD is not a true semiconductor; instead electrical conduction via a hopping mechanism is proposed.[26] Although, the ET rate will be sensitive to the number of available charge carriers in the material, the effect is not as significant as for truly semi-conducting BDD. For example, it has been shown that for $Ru(NH_3)_6^{3+}$ reduction at low doped BDD electrodes [$<1 \times 10^{19}$ B atoms cm^{-3}] the material behaves as a p-type semiconductor in the charge depleted state, whereby ET is effectively retarded.[33,34]

4.5 Effect of using an Alternative Mediator

To further investigate k^0 rates at the pBDD electrode/solution interface an alternative redox mediator was employed, $FcTMA^+$. The standard redox potential for $FcTMA^{+/2+}$ (0.42 V versus Ag/AgCl)[35] is further positive than for $Ru(NH_3)_6^{3+}$ (-0.122 V versus Ag/AgCl), and although still in the depletion region for p-type semiconducting BDD, is less negative of the flatband potential than for $Ru(NH_3)_6^{3+}$. Flatband potentials in the range 1.0 – 4.0 V versus SCE have been measured for oxygen terminated BDD surfaces.[36,37]

70 μm x 70 μm IC-SECM images were recorded in a different area of the sample at d = 1 μm, for a = 1.3 μm (Figure 4.8a) in a solution containing 1 mM $FcTMA^+$ in 50 mM KNO_3 supporting electrolyte. The substrate was biased at a potential of 0.42 V versus Ag/AgCl to oxidise $FcTMA^+$ whilst the tip was biased at 0 V. The corresponding k^0 map, Raman map and FE-SEM image are shown in Figure 4.8b, c and d respectively.

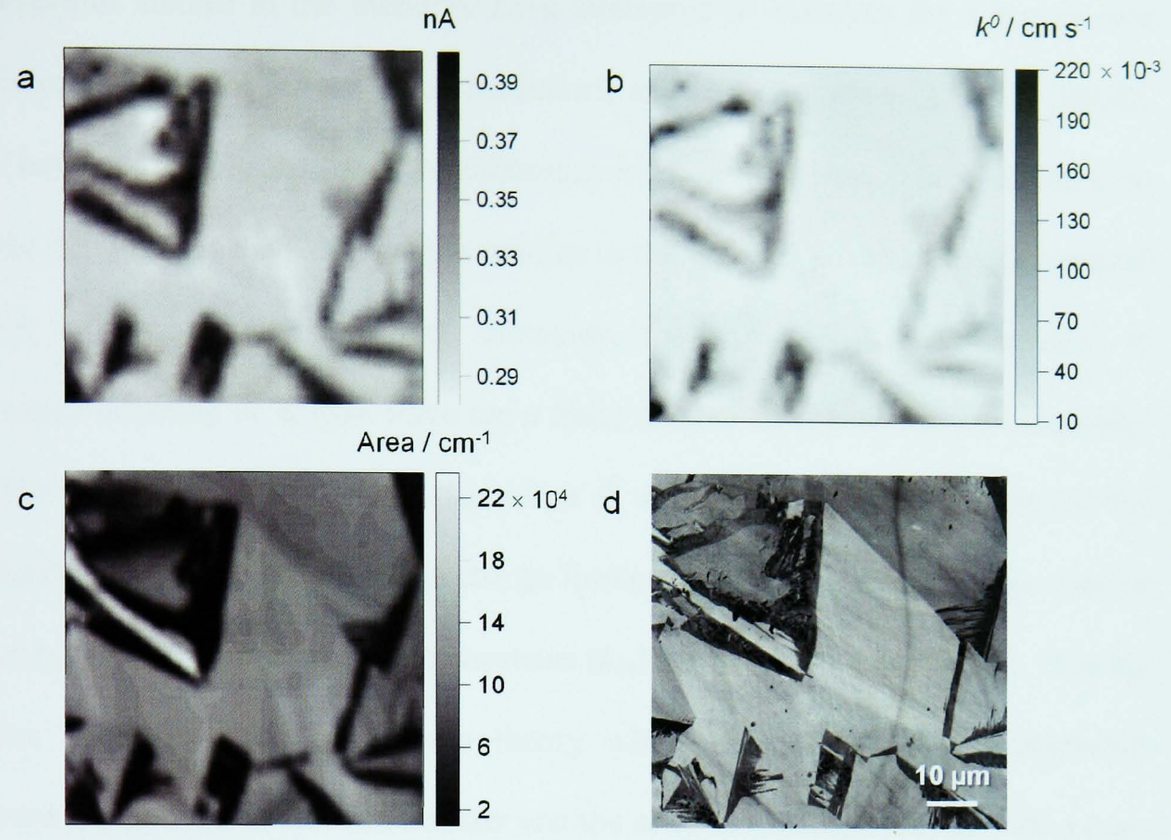

Figure 4.8 a) 70 µm × 70 µm IC-SECM SG-TC mode images for the collection of 1 mM $FcTMA^{2+}$ electrogenerated at the surface of pBDD. The substrate was held with an η of 0.045 V. b) k^0 maps calculated from the measured tip currents using the finite element simulations described above. c) Raman map to show the integrated area of the 1332 cm^{-1} peak and d) FE-SEM image recorded at 2 kV

Again as for $Ru(NH_3)_6^{3+}$ reduction there is a very close correlation between the ET activity and the boron doping levels of the substrate. All areas of the surface investigated in Figure 4.8 show [B] > 10^{20} atoms cm^{-3} (from the presence of the Fano resonance in the Raman spectra) and the ET rate is highest in the more highly doped regions of the surface. k^0 values across the surface ranged from 208 x 10^{-3} (± 44 x 10^{-3}) cm s^{-1} (most highly doped regions) to 12 x 10^{-3} (± 0.55 x 10^{-3}) cm s^{-1} (least doped regions). When comparing the ET activity i.e. k^0, for the same concentration redox species, the more highly doped regions of the pBDD show k^0 values approximately fifty times higher for $FcTMA^+$ oxidation than for $Ru(NH_3)_6^{3+}$ reduction.

Previous studies in the literature have attempted to calculate the apparent rate constant (k_{app}) for several redox mediators, including $Ru(NH_3)_6^{3+}$,[38,39] on pBDD. They have largely attributed the difference in k_{app} for different redox mediators to the E^o value for the redox couple relative to the flatband potential of the material i.e. a charge depletion effect. However, this assumes that the material is semiconducting or at least there are a finite number of charge carriers available. The fact we see redox couple dependant k^0 values in the metallic regions of the surface cannot be ascribed to a charge limiting effect. Instead it is important to consider the self exchange rate constants (k_{ex}) for the two redox couples. The k_{ex} has been described by Marcus theory which demonstrates the relationship between the rate of electron transfer and the activation energy required for a one-electron oxidation or reduction process to occur. In order for the mediator to change oxidation state it has to reorganise itself by altering bond lengths and angles. This requires a certain amount of energy, the reorganisation energy, and the rate at which this process can occur is governed by the self exchange rate constant. This therefore is the limiting factor for the standard rate of reaction. k_{ex} is related to k^0 through the following equation:

$$(k_{ex} / A_{ex})^{1/2} = k^0 / A_{el} \qquad (4.7)$$

where A_{ex} (10^4 – 10^5 cm s^{-1}) and A_{el} (10^{11} – 10^{12} M^{-1} s^{-1}) are pre-exponential factors for the self exchange and electrode reaction.[31,40] k_{ex} for $FcTMA^+$ = 9 × 10^6 M^{-1} s^{-1} [41] whilst k_{ex} for $Ru(NH_3)_6^{3+}$ ~ 4 × 10^3 M^{-1} s^{-1},[42,43] This suggests that ET for $FcTMA^+$ oxidation should be significantly faster (by 50 times) than for $Ru(NH_3)_6^{3+}$ reduction, as observed in this data for the more conducting regions.

4.6 CONCLUSIONS

IC-SECM, the newly developed electrochemical imaging technique, which enables exquisite control over the tip-substrate separation, has been employed to map and quantify the activity of pBDD. The tip-substrate separation can be accurately determined and kept at a fixed distance during scanning.

This work has enabled the electroactivity of pBDD to be both mapped and quantified in terms of k^0, on a grain by grain and point by point basis; resolution of the SECM image is ~ 2 μm governed by the size of the SECM electrode employed. Areas of the sample which contained higher levels of boron, as determined by both FE-SEM and Raman mapping, were shown to exhibit faster ET than neighbouring less boron doped regions. Raman mapping indicated that the [B] of the surface > 1×10^{20} atoms cm^{-3}, with some areas doped sufficiently to be metallic in nature whilst the remainder of the surface exhibited "hopping type" conductivity. The [B] of the surface was never low enough for any region of the surface to be deemed semi-conducting.

For $Ru(NH_3)_6^{3+}$ reduction the ET activity of the surface ranged from 2.1×10^{-3} ($\pm$ 0.1×10^{-3}) – 4.5×10^{-3} ($\pm$ 0.1×10^{-3}) cm s^{-1} at 1 mM concentration, whilst at 5 mM concentration a range of 0.3×10^{-3} ($\pm$ 0.1×10^{-3}) – 4.6×10^{-3} ($\pm$ 0.1×10^{-3}) cm s^{-1} for k^0 was determined. For $FcTMA^+$ oxidation at 1 mM concentration k^0 values ranged from 12×10^{-3} ($\pm$ 0.55×10^{-3}) – 208×10^{-3} ($\pm$ 44×10^{-3}) cm s^{-1}. For $Ru(NH_3)_6^{3+}$ reduction in the more highly doped regions of the surface, k^0 is effectively independent of concentration indicating that these regions are doped metallically, as indicated by the Raman spectra. In the lower doped regions the

fact that k^0 is lower for the higher redox concentration solution suggests that the number of available charge carriers in the material is a limitation. For 1 mM $FcTMA^+$ oxidation in the metallic–like regions significantly larger k^0 values are observed compared to k^0 for the reduction of $Ru(NH_3)_6^{3+}$, the difference can be explained by consideration of the self exchange rate constant for the two different species. Again in the lower doped regions of the sample k^0 for $FcTMA^+$ oxidation is reduced re-emphasising a reduction in the available charge carriers in the less doped material.

4.7 REFERENCES

(1) Johnson, L.; Niaz, A.; Boatwright, A.; Voisey, K. T.; Walsh, D. A. *J. Electroanal. Chem.* **2011**, *657*, 46.

(2) Wang, J.; Yang, S.; Guo, D.; Yu, P.; Li, D.; Ye, J.; Mao, L. *Electrochem. Commun.* **2009**, *11*, 1892.

(3) Dumitrescu, I.; Dudin, P. V.; Edgeworth, J. P.; Macpherson, J. V.; Unwin, P. R. *J. Phys. Chem. C* **2010**, *114*, 2633.

(4) Oltra, R.; Zimmer, A.; Sorriano, C.; Rechou, F.; Borkowski, C.; Néel, O. *Electrochim. Acta* **2011**, *56*, 7038.

(5) Santana, J. J.; González-Guzmán, J.; Fernández-Mérida, L.; González, S.; Souto, R. M. *Electrochim. Acta* **2010**, *55*, 4488.

(6) Argoitia, A.; Martin, H. B.; Rozak, E. J.; Landau, U.; Angus, J. C. *Electrochemical studies of boron-doped diamond electrodes*; Materials Research Soc: Pittsburgh, 1996.

(7) Martin, H. B.; Argoitia, A.; Landau, U.; Anderson, A. B.; Angus, J. C. *J. Electrochem. Soc.* **1996**, *143*, L133.

(8) Xu, J. S.; Granger, M. C.; Chen, Q. Y.; Strojek, J. W.; Lister, T. E.; Swain, G. M. *Anal. Chem.* **1997**, *69*, A591.

(9) Guell, A. G.; Meadows, K. E.; Unwin, P. R.; Macpherson, J. V. *Phys. Chem. Chem. Phys.* **2010**, *12*, 10108.

(10) Rao, T. N.; Yagi, I.; Miwa, T.; Tryk, D. A.; Fujishima, A. *Anal. Chem.* **1999**, *71*, 2506.

(11) Sarada, B. V.; Rao, T. N.; Tryk, D. A.; Fujishima, A. *Anal. Chem.* **2000**, *72*, 1632.

(12) Compton, R. G.; Foord, J. S.; Marken, F. *Electroanalysis* **2003**, *15*, 1349.

(13) Janssen, G.; van Enckevort, W. J. P.; Vollenberg, W.; Giling, L. J. *Diamond Relat. Mater.* **1992**, *1*, 789.

(14) Samlenski, R.; Haug, C.; Brenn, R.; Wild, C.; Locher, R.; Koidl, P. *Diamond Relat. Mater.* **1996**, *5*, 947.

(15) Spitsyn, B. V.; Bouilov, L. L.; Derjaguin, B. V. *J. Cryst. Growth* **1981**, *52*, 219.

(16) McKelvey, K.; Edwards, M. A.; Unwin, P. R. *Anal. Chem.* **2010**, *82*, 6334.

(17) Macpherson, J. V. PhD thesis, University of Warwick 1996.

(18) Bard, A. J.; Faulkner, L. R. **2001**, 127.

(19) Miller, J. B.; Brandes, G. R. *J. Appl. Phys.* **1997**, *82*, 4538.

(20) Holt, K. B.; Bard, A. J.; Show, Y.; Swain, G. M. *J. Phys. Chem. B* **2004**, *108*, 15117.

(21) Wilson, N. R.; Clewes, S. L.; Newton, M. E.; Unwin, P. R.; Macpherson, J. V. *J. Phys. Chem. B* **2006**, *110*, 5639.

(22) Neufeld, A. K.; O'Mullane, A. P. *J. Solid State Electrochem.* **2006**, *10*, 808.

(23) Honda, K.; Noda, T.; Yoshimura, A.; Nakagawa, K.; Fujishima, A. *J. Phys. Chem. B* **2004**, *108*, 16117.

(24) Bernard, M.; Deneuville, A.; Muret, P. *Diamond Relat. Mater.* **2004**, *13*, 282.

(25) Szunerits, S.; Mermoux, M.; Crisci, A.; Marcus, B.; Bouvier, P.; Delabouglise, D.; Petit, J.-P.; Janel, S.; Boukherroub, R.; Tay, L. *J. Phys. Chem. B* **2006**, *110*, 23888.

(26) Lagrange, J. P.; Deneuville, A.; Gheeraert, E. *Diamond Relat. Mater.* **1998**, *7*, 1390.

(27) Knight, D. S.; White, W. B. *J. Mater. Res.* **1989**, *4*, 385.

(28) Bachmann, P. K.; Leers, D.; Lydtin, H. *Diamond Relat. Mater.* **1991**, *1*, 1.

(29) Macpherson, J. V.; O'Hare, D.; Unwin, P. R.; Winlove, C. P. *Biophys. J.* **1997**, *73*, 2771.

(30) Burnett, D. S. *Finite Element Analysis*; Addison-Wesley: Reading, Massachusetts, 1987.

(31) Bard, A. J.; Faulkner, L. R. *Electrochemical Methods: Fundamentals and Applications 2nd ed.*; Wiley: New York, 2001.

(32) Gheeraert, E.; Gonon, P.; Deneuville, A.; Abello, L.; Lucazeau, G. *Diamond Relat. Mater.* **1993**, *2*, 742.

(33) Barbu, B. *Electrical and Electrochemical Characterisation of Single Crystal Diamond (PhD Thesis 2010).*

(34) Latto, M. N.; Pastor-Moreno, G.; Riley, D. J. *Electroanalysis* **2004**, *16*, 434.

(35) Krapf, D.; Quinn, B. M.; Wu, M.-Y.; Zandbergen, H. W.; Dekker, C.; Lemay, S. G. *Nano Lett.* **2006**, *6*, 2531.

(36) van de Lagemaat, J.; Vanmaekelbergh, D.; Kelly, J. J. *J. Electroanal. Chem.* **1999**, *475*, 139.

(37) Rao, T. N.; Tryk, D. A.; Hashimoto, K.; Fujishima, A. *J. Electrochem. Soc.* **1999**, *146*, 680.

(38) Granger, M. C.; Witek, M.; Xu, J.; Wang, J.; Hupert, M.; Hanks, A.; Koppang, M. D.; Butler, J. E.; Lucazeau, G.; Mermoux, M.; Strojek, J. W.; Swain, G. M. *Anal. Chem.* **2000**, *72*, 3793.

(39) Neufeld, A.; O'Mullane, A. *J. Solid State Electrochem.* **2006**, *10*, 808.

(40) Anderson, L. B.; Reilly, C. N. *J. Chem. Educ.* **1967**, *44*, 9.

(41) Nielson, R. M.; McManis, G. E.; Weaver, M. J. *J. Phys. Chem.* **1989**, *93*, 4703.

(42) Smolenaers, P. J.; Beattie, J. K. *Inorg. Chem.* **1986**, *25*, 2259.

(43) Brown, G. M.; Sutin, N. *J. Am. Chem. Soc.* **1979**, *101*, 883.

CHAPTER 5

SCANNING ELECTROCHEMICAL CELL MICROSCOPY (SECCM): APPLICATION TO ELECTROCHEMICAL PROCESSES AT POLYCRYSTALLINE BORON DOPED DIAMOND (PBDD)

ABSTRACT

The recently developed scanning electrochemical cell microscopy (SECCM) technique has been employed to demonstrate the many advantages this technique has over conventional electrochemical imaging methods. The SECCM employs a laser pulled theta capillary which is filled with electrolyte and/or a redox active mediator forming a meniscus at the end. The pipette contains measurement electrodes. This meniscus is brought into contact with an electrode surface to form an electrochemical cell, where localised measurements can be taken. A polycrystalline boron doped diamond (pBDD) substrate is employed herein to demonstrate electrochemical reactions of classical outer sphere and 'simple' inner sphere electron transfer reactions. The maps of electroactivity reveal a heterogeneous substrate. Furthermore, the activity can be correlated with field emission scanning electron micrographs (FE-SEM) of the various grains. In addition to the outer sphere and 'simple inner sphere' mediators, a 'complex' inner sphere electron transfer reaction has been investigated which is notorious for electrode fouling. However, because SECCM scans a droplet over a surface, a fresh area is analysed, as the capillary is moved during scanning. Fouling of the electrode is thus largely avoided and a map revealing the heterogeneity of the pBDD substrate can be obtained.

5.1 INTRODUCTION

Electrochemical scanning probe techniques provide the opportunity to electrochemically image a surface, providing valuable local information about a substrate. Scanning electrochemical microscopy (SECM)[1-3] and scanning ion conductance microscopy (SICM)[4] are amongst these techniques. However, with conventional SECM imaging techniques it is very difficult to distinguish the variations in local activity from the topographical features of the sample, as both give rise to similar features in the imaging maps, as highlighted in the preceding Chapter. Therefore, there has been an increased interest in developing electrochemical scanning probe techniques with positional feedback, such as SECM-AFM[5], SECM-SICM[6] and, more recently, IC-SECM.[7] However, all these techniques still require the sample to be completely immersed in solution, which can lead to three major implications. First, the spatial resolution will be limited (to some extent) due to the overlap of diffusion fields from different reactive regions of the substrate. Second, imaging with these techniques require the whole substrate to be held at conditions where it is active during the entire time it takes to record an image (which may be tens of minutes to hours). This can lead to changes in surface properties over time. Finally, extended immersion of the sample can lead to fouling / deactivation by adsorption of species. This is a significant issue in electrochemistry which is often overlooked.

To minimise these potential issues, there is a need for a spatially localised electrochemical imaging technique in which the sample is only in contact with solution for short amounts of time. Keeping this in mind, we have recently developed the scanning electrochemical cell microscopy (SECCM) technique.[8]

In this chapter we demonstrate the advantages of this technique with a heterogeneous polycrystalline boron doped diamond (pBDD) substrate (oxygen terminated).[9-11]

Employing SECCM on pBDD, we demonstrate how the electrochemical activity of a single pBDD grain can be determined using two classical outer sphere redox mediators, a 'simple' inner sphere redox mediator and a 'complex' inner sphere redox system which is known to foul the electrode upon oxidation. Furthermore, we show that the standard rate constant k^0 can be obtained from the electrochemical activity, through finite element simulations.

5.2 Scanning electrochemical cell microscopy (SECCM)

Scanning electrochemical cell microscopy (SECCM)[8] has major advantages over existing electrochemical imaging techniques, as it enables electrochemical measurements to be taken in a spatially localised region. A schematic showing the typical set-up of this technique can be seen in Figure 5.1.

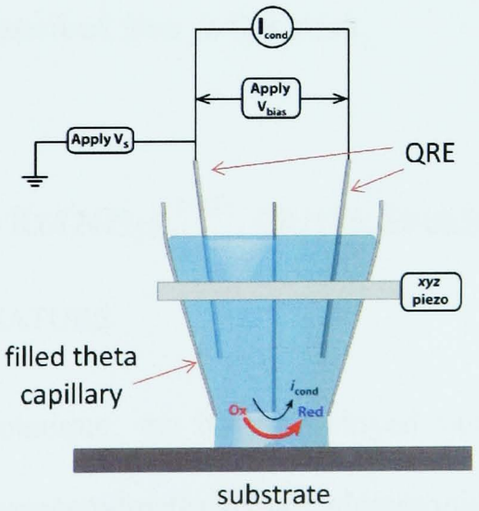

Figure 5.1 Schematic showing a typical SECCM set-up adapted from Ref. 12

The SECCM employs a laser-pulled borosilicate theta capillary as the electrochemical probe. The theta capillary has two barrels, separated by a glass septum, which are filled with the redox mediator or electrolyte of interest (using a Microfil (WPI Instruments) and syringe). The filled capillary is approached to the substrate of interest, in this case pBDD, with a bias applied between the quasi reference electrodes (QREs) in the barrels (either Ag/AgCl wires or Pd-H_2[13]). When the meniscus, formed at the mouth of the capillary, comes into contact with a surface, an alternating current component, i_{AC}, in the current between the barrels is established, due to a small oscillation applied to the z-position of the capillary. This alternating current is very sensitive to the tip-substrate separation and can be used as a set point for electrochemical imaging, to maintain contact between the meniscus and substrate. The mean conductance current, i_{DC}, can be measured simultaneously. Therefore, this technique not only provides topographical information about the substrate, but also the local functional properties. The capillary (and thus the electrochemical cell) can be swept over the surface to map the surface reactivity, or held at a fixed position to perform localised electrochemical experiments such as cyclic voltammetry (CV) or chronoamperometry, described later in this work.

5.3 $FcTMA^{+/2+}$ and $Ru(NH_3)_6^{3+/2+}$: Outer Sphere Electron Transfer Mediators

Using the SECCM technique, we have employed two classical outer sphere redox mediators, ferrocenylmethyltrimethylammonium ($FcTMA^{+/2+}$) and hexamine ruthenium chloride ($Ru(NH_3)_6^{3+/2+}$) to study electron transfer kinetics at pBDD. Figure 5.2 shows an example of an i_{AC} approach curve. This shows

that when the capillary is in air the observed current is *ca.* 0 A. A sharp increase in i_{AC} can be observed as the meniscus comes into contact with the surface. An i_{AC} set-point is used to obtain the maps and to ensure the meniscus would keep contact with the surface, without crashing into the surface. This was set between 80-120 pA, approximately 1 % of i_{DC} current, which can be used to determine the meniscus height, or the tip-substrate separation determined to be *ca.* one capillary radius (*ca.* 1 μm), based on finite element modelling.[14]

The electrochemical reactivity maps for the oxidation of $FcTMA^+$ (for example Figure 5.3ai) or the reduction of $Ru(NH_3)_6^{3+}$ (for example Figure 5.3aii) were performed using a capillary with a total inner diameter of *ca.* 2 μm (< 1 μm in each channel). Since the contact area between the meniscus and the surface is determined by capillary diameter,[8] this results in an effective working electrode area of a few μm^2.

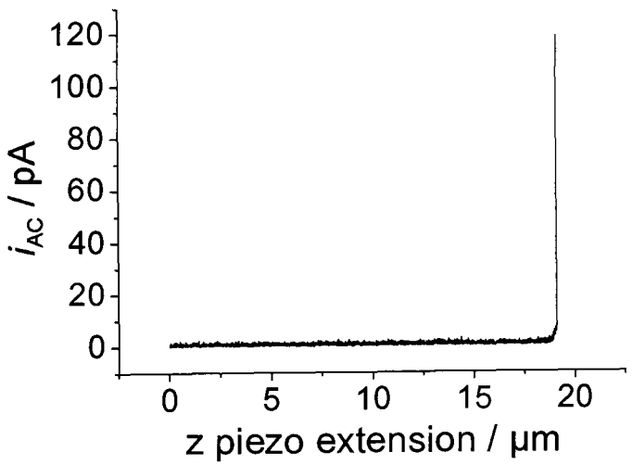

Figure 5.2 An example of an i_{AC} *approach curve*

Figure 5.3a shows typical 50 x 50 μm SECCM images of the pBDD surface for the i) oxidation of 2 mM $FcTMA^+$ (substrate held at 300 mV η = -8mV versus

Ag/AgCl) and ii) the reduction of 2 mM $Ru(NH_3)_6^{3+}$ (substrate held at -250 mV, η = 23 mV versus Ag/AgCl). Images were recorded by taking a reading every 1 μm. The corresponding field emission scanning electron microscopy (FE - SEM) images are shown in Figure 5.3b. It is evident that heterogeneities in current on the pBDD surface are a direct consequence of the grain structure. As highlighted earlier in this thesis, different crystal faces of pBDD incorporate boron more readily into the lattice, for example the (111) crystal face may take up to ten times more boron than the (100) face during synthesis.[15-17]

Comparison of the electrochemical activity maps obtained using SECCM (Figure 5.3a) with the FE-SEM images shows that there is a close correlation between heterogeneities in electron transfer rate across the surface (as reflected in the SECCM currents) with the underlying grain structure. Evidently, areas with higher dopant levels yield a higher current, which is indicative of faster ET kinetics. This indicates that the local dopant level directly impacts the corresponding local electrochemical reactivity. Furthermore, the SECCM maps clearly show that the entire surface of the pBDD is electrochemically active,[10,18] with no evidence for any increased intrinsic electron transfer rates at grain boundaries, a topic that has been debated in the literature.[19]

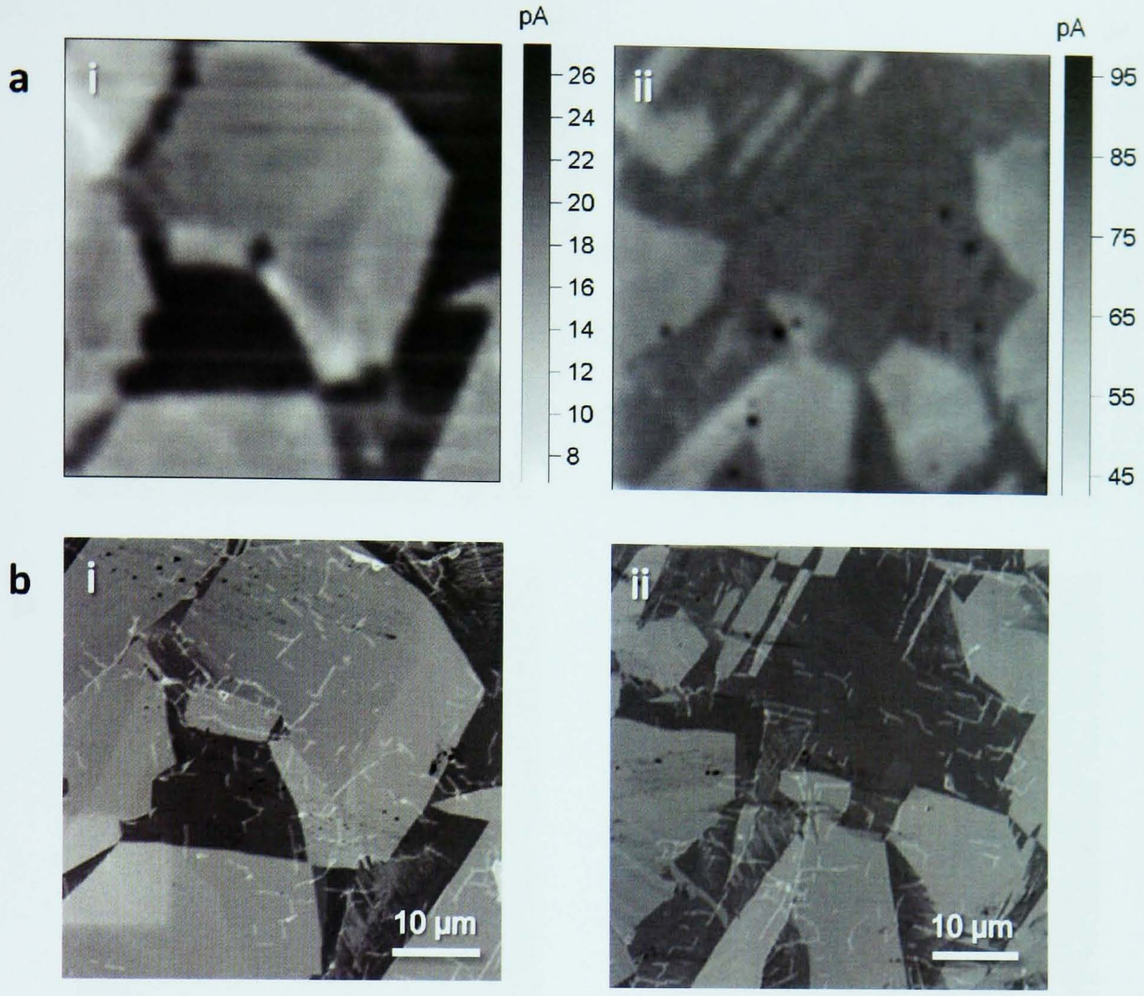

Figure 5.3 50 x 50 µm SECCM images of ai) oxidation of 2 mM $FcTMA^+$ (300 mV at substrate η = - 8mV) and aii) reduction of 2 mM $Ru(NH_3)_6^{3+}$ (-250 mV at substrate η = 23 mV) bi) and bii) show the corresponding FE-SEM images

The effect of analyte concentration was studied by recording SECCM maps at varying $Ru(NH_3)_6^{3+}$ bulk concentrations. Figure 5.4a shows 50 x 50 µm SECCM images of the pBDD surface for the i) reduction of 5 mM $Ru(NH_3)_6^{3+}$ ii) reduction of 10 mM $Ru(NH_3)_6^{3+}$ where the substrate is held at -250 mV, η = 23 mV. The corresponding FE-SEM images are shown in Figure 5.4b. The concentration dependence of $Ru(NH_3)_6^{3+}$ is of particular interest as pBDD is a p-type semi conductor. p-type semi-conductors have holes as charge carriers, where charge carrier depletion effects may play a role for electro-reduction processes at increased mediator concentrations.

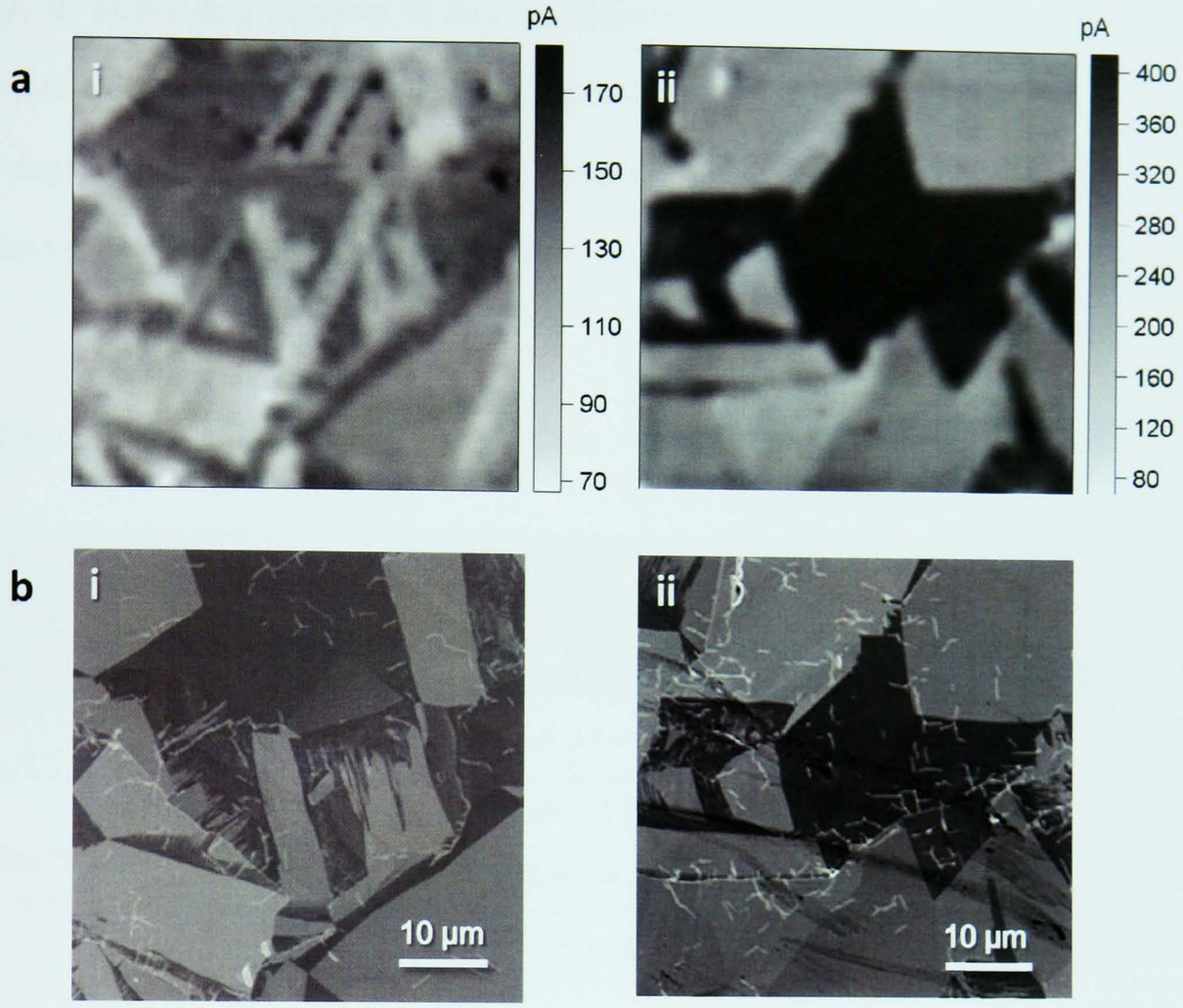

Figure 5.4 50 x 50 µm SECCM images of ai) reduction of 5 mM $Ru(NH_3)_6^{3+}$ (-250 mV at substrate, η = 23 mV) and aii) reduction of 10 mM $Ru(NH_3)_6^{3+}$ (-250 mV at substrate, η = 23 mV) bi) and bii) show the corresponding FE-SEM images

Table 5.1 shows the ratio of electroactivity for the more and less conducting regions on pBDD. The ratio has been calculated using the highest 10 % (corresponding to 260 pixels on map) and lowest 10 % (corresponding to 260 pixels on map) of current values from the SECCM images in Figure 5.3a and Figure 5.4a. When analysing the reduction of $Ru(NH_3)_6^{3+}$, a direct comparison between the ratios can be made as the images showing the reduction for 2 mM, 5 mM and 10 mM were recorded at the same (over)potential. As the concentration of the $Ru(NH_3)_6^{3+}$ mediator is increased, it is evident that the difference in activity between the more and less conducting grains is enhanced. We propose,

due to earlier data (Chapter 4) that the regions of higher conductivity behave metallic-like, however grains that are less conducting become challenged due to a depletion of charge carriers. In this instance, the conductivity is not metallic-like but occurs via a hopping mechanism.[20]

Table 5.1 Table to show the activity ratio at more and less conducting grains for two redox mediators with a range of concentrations

Redox Mediator	Concentration (mM)	Electroactivity for more conducting regions (pA)	Electroactivity for less conducting regions (pA)	Ratio of activity (more / less)
$FcTMA^{+/2+}$ η = -8 mV	2	25.5 ± 0.7	12.3 ± 1.8	2.1
$Ru(NH_3)_6^{3+/2+}$ η = 23 mV	2	83.6 ± 2.5	67.2 ± 2.3	1.2
	5	149.9 ± 5.4	90.3 ± 6.0	1.6
	10	401.0 ± 42	201 1 ± 1.86	1.9

5.4 Determining the standard rate constant, K^0

A finite element model (FEM) (Comsol Multiphysics 4.1 (Comsol AB, Sweden with MatLab 2009b (Mathworks Inc., Cambridge)) was employed to determine the k^0 for the oxidation of $FcTMA^+$. The model approximates the SECCM tip geometry accurately using certain geometric information about the capillary[14] shown in Figure 5.5a. The key parameters are the semi-angle (θ) and the tip radius (r_p) as these determine the flux to the substrate electrode. These parameters can be measured by FE-SEM. Other important parameters are the meniscus height (m_h) and contact diameter (m_w). Approach curve experiments[12] can be used and in this work the meniscus height was determined to be typically the equivalent of 1 radius away from the substrate (pBDD). As capillaries employed for SECCM measurements were silanised before use to render the

outer walls hydrophobic, we confine the meniscus to the end of the capillary in the simulations. In particular, the meniscus has straight sidewalls and a contact radius (m) identical to the pipette radius (in the FEM).

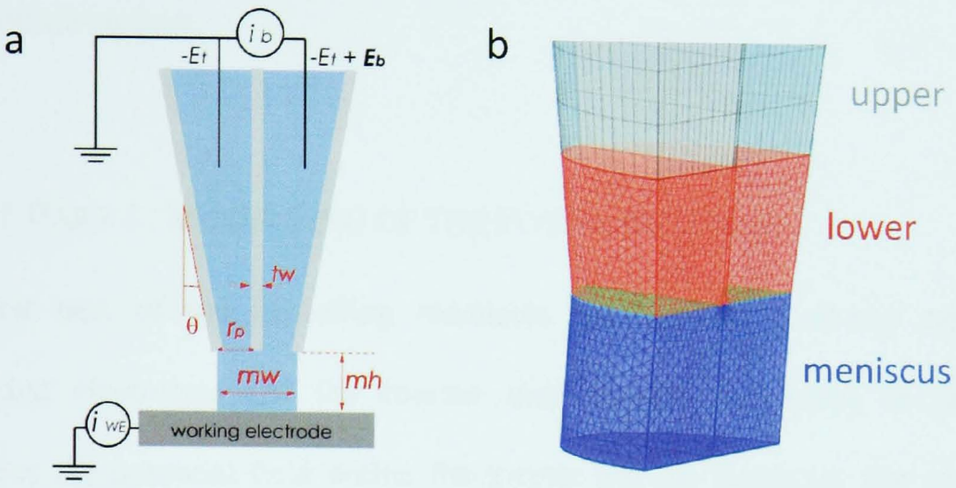

Figure 5.5 a) Schematic to represent the SECCM set-up with key parameters shown including r_p (inner radius), m_w (meniscus contact diameter), m_h (meniscus height), t_w (central segment thickness) and θ (semi-angle of the pulled pipette) taken from Ref 14 b) Schematic of the capillary that is modelled showing the relative mesh sizes

One half of each filled capillary was modelled to optimise computational resources as there is a symmetry plane perpendicular to the septum of the capillary and the electrode surface. The simulated domain was split into three segments to aid meshing, the upper region, the lower region and the meniscus, as highlighted in Figure 5.5b. The meniscus and the lower section of the barrel were modelled using a finer mesh than the upper section. This enabled the model to be computationally efficient without sacrificing the accuracy in the areas of highest concentrations and potential changes (lower region and meniscus).

The model was solved in two separate steps: (i) calculation of the potential field independent of a surface reaction, and (ii) calculating the mass transport of the mediator species under the influence of the potential field calculated in part (i) with a kinetically limited electrochemical reaction (Butler-Volmer kinetics) at the substrate surface.

5.4.1.1 PART 1: MODELLING OF THE POTENTIAL FIELD

The first part of the modelling simulates the movement of the mediator, supporting electrolyte and the counter ions present in solution in order to determine the potential field within the pipette and the meniscus. For example, when electrochemically imaging the oxidation of $FcTMA^+$, the model will simulate movement of $FcTMA^+$ (the concentration of $FcTMA^{2+}$ was not taken into account as this was a minor species), the counter ion, PF_6^-, and also the supporting electrolyte ions, K^+ and Cl^-. The Nernst-Planck equations for mass transport are solved within the simulated domain with the potential field calculated (Equation 5.1, 5.2 and 5.3):

$$\nabla(-D_i \nabla c_i - z_i u_{m,i} F c_i \nabla V) = 0 \tag{5.1}$$

$$\sum z_i c_i = 0 \tag{5.2}$$

$$N_i = F \sum z_i \left(-D_i \nabla c_i - z_i u_{m,i} F c \nabla V\right) \tag{5.3}$$

where c_i is the concentration, D_i is the diffusion coefficient, z_i is the charge of the species, u_i is the ionic mobility of the species, F is Faraday's constant and V is the electric field.

For the modelling of the potential field, the substrate is set up to be inert, RE1 is set to 0 V and RE2 to the experimentally applied bias potential (generally 200 mV). As the simulated domain is only a fraction of the experimental pipette there will be a resistance within the pipette. To take into account uncompensated simulated resistance, the simulated migration current is matched to the experimental current by setting the simulated bias to a fraction of the experimental bias.

5.4.1.2 PART 2: MOVEMENT OF MEDIATOR

This part of the modelling uses the potential field calculated from Part 1 to determine how species are moving, or specifically the oxidised or the reduced form of the mediator (Note: only the reactant species is accounted for here). Mass transport of the mediator is solved within the domain using the Nernst-Planck equation (Equation 5.1). The flux normal to all side walls and the meniscus walls are set to zero because there is no transport across these boundaries. Butler-Volmer kinetics (Equations 5.4 and 5.5) are described at the electrode/solution interface where k_f and k_b are the rate of the forward and backward reaction respectively.

$$k_f = k^0 \exp\left[\frac{-\alpha\eta F}{RT}\right] \tag{5.4}$$

$$k_b = k^0 \exp\left[\frac{(1-\alpha)\eta F}{RT}\right] \tag{5.5}$$

where k^0 is the standard rate constant, α is the transfer coefficient, η is the overpotential (or E-$E^{0'}$ where $E^{0'}$ is the formal potential), F is Faraday's constant, R is the gas constant and T is the temperature.

A series of k^0 values are input into the model and used to calculate k_f and k_b (Equation 5.4 or 5.5), which, in turn, determined the interfacial flux:

$$\mathbf{n}.N_{med} = k_b(c_{bulk} - c_{med}) - k_f c_{med} \quad (5.6)$$

where $\mathbf{n}.N_{med}$ is the flux of the mediator ($FcTMA^+$) and c is the concentration.

5.4.1.3 Converting current maps to K^0

A plot showing the log (k^0) versus the current was fitted with a Boltzmann curve, providing a fit that can convert experimental current values to k^0.

Figure 5.6 shows the k^0 map for the oxidation of 2 mM $FcTMA^+$, where the tip was fully characterised with FE-SEM (radius of tip = 0.75 μm). From the simulations, k^0 values of ~ 0.21 cm s^{-1} are reported for the regions of high conductivity, whereas ~ 0.01 cm s^{-1} were determined for the regions of low conductivity. These were in good agreement for the values of k^0 determined in Chapter 4 when intermittent contact-scanning electrochemical microscopy (IC-SECM) was employed to investigate the oxidation of 2 mM $FcTMA^+$ at a pBDD substrate, demonstrating the ability of extracting quantitative kinetic information from SECCM measurements.

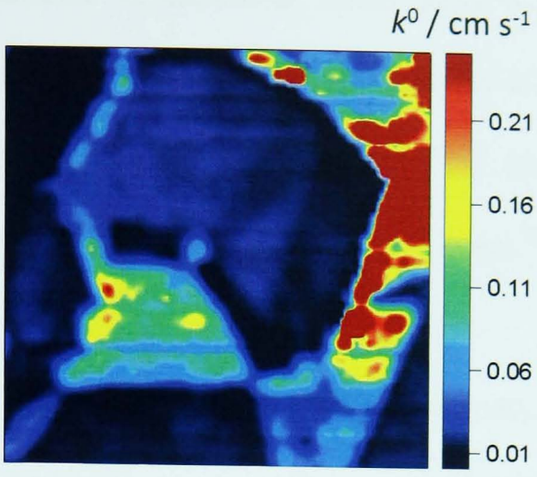

Figure 5.6 Map of k^0 (cm s^{-1}) for the oxidation of 2 mM $FcTMA^+$ at a pBDD substrate

5.5 $Fe^{2+/3+}$: A 'Simple' Inner Sphere Electron Transfer Mediator

In addition to studying outer sphere ET couples, we have also investigated the reactivity of pBDD towards a typical 'simple' inner sphere electron transfer mediator, $Fe^{2+/3+}$. Inner sphere electron transfer mediators differ from the classical outer sphere redox mediators as the mediator needs to lose part of its solvation shell before electron transfer, in which surface coordination plays a role. There are two specific motivations to investigate an inner sphere mediator on a pBDD substrate. Firstly, pBDD is a heterogeneous substrate as a result of the varied boron uptake in the sample and therefore an interesting material to investigate (discussed in more detail in Section 5.3). Furthermore, different grains could possess different terminating oxygen functional groups.[21,22] For example, it is known that (111) faces are mostly terminated by hydroxyl groups while the most abundant groups on the (100) faces are ethers or carboxyl groups.[23,24] As the $Fe^{2+/3+}$ redox couple is considered to be sensitive to surface oxygen - containing functional groups on pBDD and carbon electrodes in

general,[25] varying surface terminations could have a big influence on the reactivity of pBDD. Further evidence for this argument is that the reversibility of other inner-sphere redox couples such as $Fe^{3+/2+}$ is improved upon oxygen-termination due to the catalytic effect of carbonyl groups.[26]

Figure 5.7a shows a typical 50 x 50 μm SECCM activity map for the oxidation of 2 mM Fe^{2+} in 0.5 M H_2SO_4 at an oxidising potential of 1.2 V (versus Pd-H_2). Similar to the outer sphere redox mediators (Section 5.3) the inherent grain structure of the pBDD (Figure 5.7a) is clearly evident in the images. Closer inspection shows that the difference between the two types of grain is much more distinct than for the studied outer sphere electron transfer reactions.

Typical CVs on the different grains are shown in Figure 5.7b, which shows a very clear difference in the oxidation onset potential towards the oxidation of Fe^{2+}. However, from these CV measurements it is evident that although the onset potential changes significantly, there are no differences observed for $E_{3/4}$-$E_{1/4}$.[27] In both cases $E_{3/4}$-$E_{1/4}$ = 144 mV (when i_{lim} was taken at 1.2 V in the more conducting region and 1.4 V in the less conducting region).

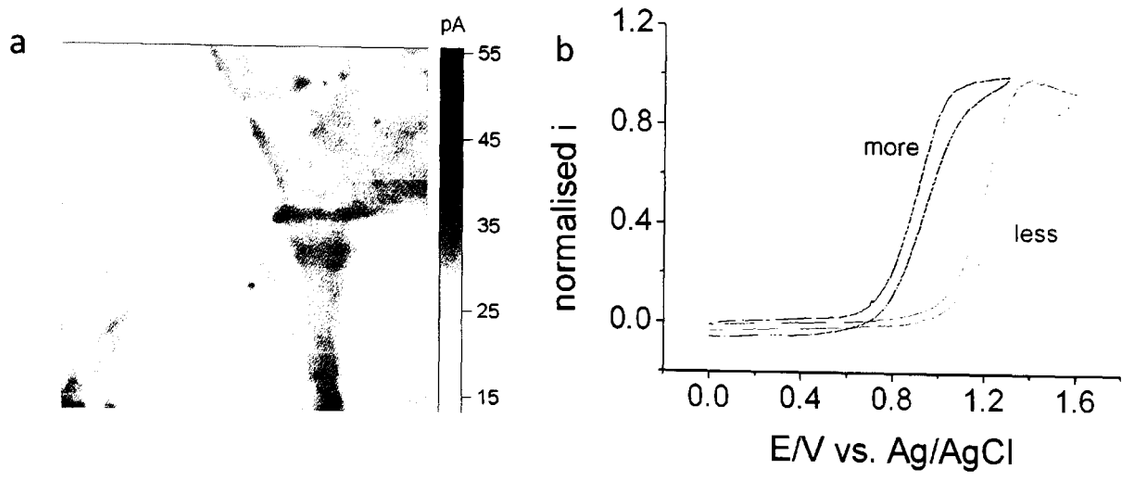

Figure 5.7 a) 50 x 50 μm SECCM image of the oxidation of 2 mM Fe^{2+} in 0.5 M H2SO4 (1.2 V at substrate) b) CVs recorded on a more and less conducting grain at a scan rate of 100 mV/s.

The CV taken on the less conducting region is shifted to a much higher overpotential. As this cannot be attributed solely to impeded electron transfer, it must be related to the local interaction between the Fe^{2+} and the pBDD grain. To verify that the shift in onset potential is related to coordinative effects, the experiments were repeated on two single crystal BDD samples with orientations of (100) (boron concentration 1 - 1.2 x 10^{19} cm^{-3} bulk with 65 nm cap layer 1 - 2 x10^{21} cm^{-3}) and (110) (boron concentration 0.8 - 1 x 10^{20} cm^{-3}) crystallographic faces.

A typical 50 x 50 μm SECCM map for the oxidation of 2mM Fe^{2+} in 0.5 M H_2SO_4 on a single crystal BDD sample is shown in Figure 5.8a, which displays uniform behaviour across the sample as expected and observed for both crystal orientations employed. CVs were recorded from 3 areas on both samples which interestingly showed that on the (110) BDD substrate the potential for the oxidation of Fe^{2+} was shifted further positive than on the (100) sample, similar to the results obtained on the different grains of the polycrystalline substrate. In

particular, the onset potential for Fe^{2+} oxidation on (100) BDD and (110) BDD correspond closely to those on the more and less doped grains on the pBDD substrate respectively, indicating that the heterogeneity of pBDD towards Fe^{2+} oxidation, could arise from the crystal orientation alone.. The resulting CV cannot be entirely due to slower kinetics as this shift in onset potential is significant.

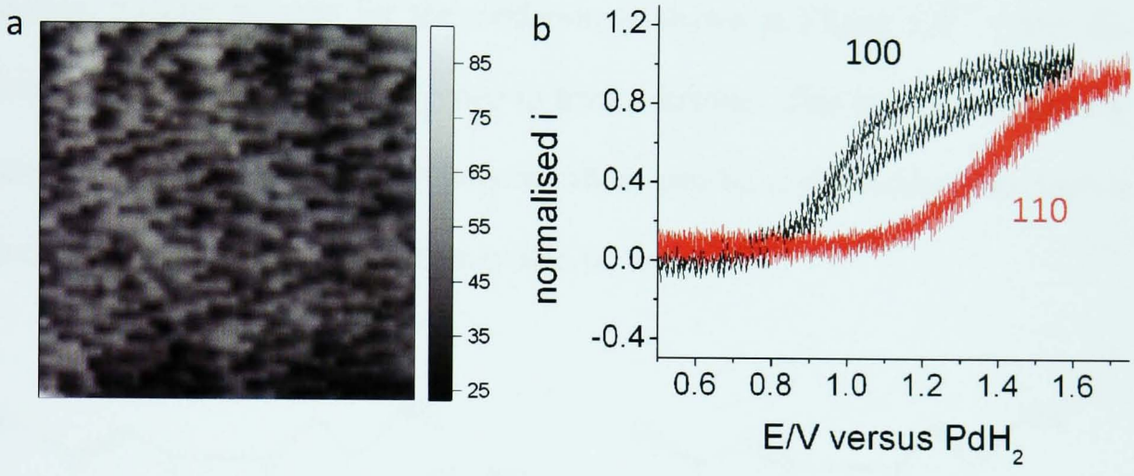

Figure 5.8 a) 50 x 50 μm SECCM images of oxidation of 2 mM Fe^{2+} in 0.5 M H_2SO_4 (1.2 V versus PdH_2 at substrate) b) Example CVs showing the response from a (110) and (100) crystal face using a scan rate of 100 mV/s

These results do suggest that, as stated in literature, the oxidation of Fe^{2+} is sensitive to surface termination and in particular the oxidation occurs more readily on the (100) orientation where carbonyl groups are most abundant. However, to further probe the reaction on the polycrystalline sample additional information on the crystal orientation is required. X-ray photoelectron spectroscopy (XPS) could be employed to determine the orientation of the more and less conducting regions and hence provide evidence that the carbonyl groups are most favoured for this oxidation.

5.6 SEROTONIN: A 'COMPLEX' INNER SPHERE MEDIATOR

Using electrochemistry to analyse neurotransmitters has been considered important for understanding and developing treatments of various illnesses, such as Alzheimer's disease, depression and schizophrenia.[28] Serotonin, or 5-Hydroxytryptamine (5-HT), is a 'complex' inner sphere electron transfer mediator which is extremely difficult to work with in terms of electrochemistry. The oxidation of serotonin is complex as many products can be formed. A two electron transfer process for the oxidation is shown in Figure 5.9[29] where the oxidation occurs at the phenol group to from a ketone. This ketone is extremely unstable and can form a hydroquinone which can be easily oxidised to form a quinone.[29] Many other products may also be formed.[30,31]

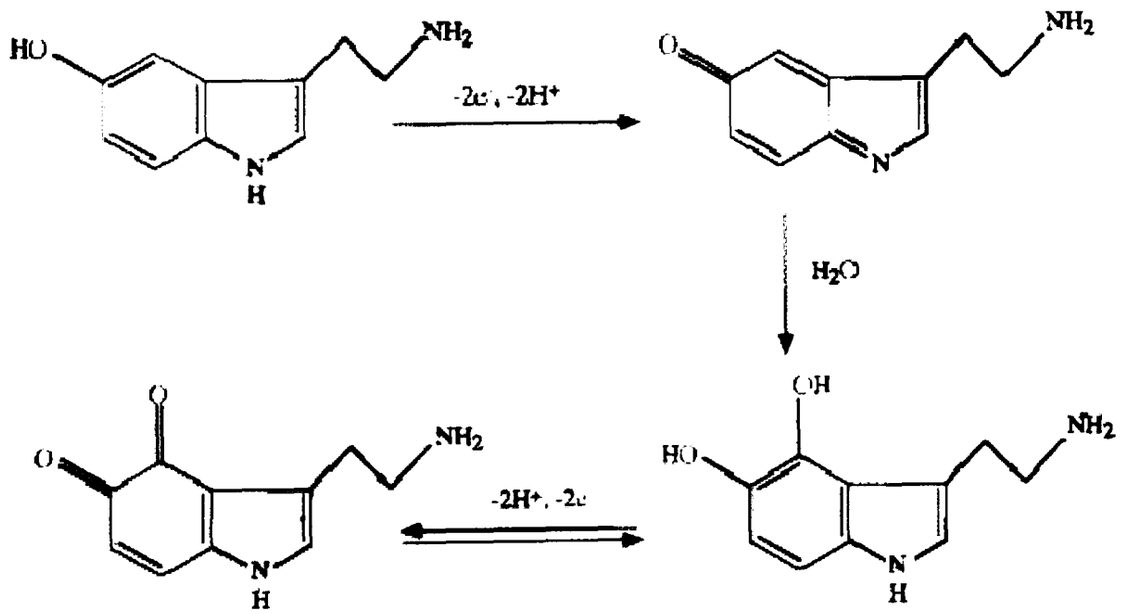

Figure 5.9 A scheme to show the oxidation of Serotonin with possible products taken from Ref[29]

The products from the oxidation of serotonin can be reactive and are notorious for blocking or fouling the electrode,[32] as previously reported based on CV measurements.[33] The products that have this blocking effect are quinones and to

alleviate the fouling of the electrode, fast scan rate CVs are performed,[32] but even then, some account of blocking must be taken. pBDD has been shown in previous reports as a promising material for the electroanalysis of serotonin.[29]

In this work, we demonstrate that serotonin oxidation on pBDD can be successfully imaged to study local reactivity even though electrode fouling occurs during the reaction. Figure 5.10a shows a 45 x 45 μm SECCM image for the oxidation of 2 mM serotonin in 5 mM HEPES and 0.1 M NaCl (substrate potential held at 0.65 V vs. Ag/AgCl QRE). Significantly, a local reactivity map can be recorded without interference from electrode fouling during the oxidation process. We attribute this with the localised nature of SECCM, in which a fresh, new electrode/electrolyte interface is probed as the capillary is moved during scanning. This demonstrates a major advantage of SECCM over conventional electrochemical imaging methods where the substrate would be immersed in solution. SECCM provides evidence for a clear difference in current towards the oxidation of serotonin, shown by the distinctive grain structure in the electrochemical image. To demonstrate the fouling effect conventional SECM based techniques would suffer from, a second image was taken immediately after the first using identical experimental conditions (Figure 5.10b). In this image there is no evidence of the underlying grain structure due to the fouling of the electrode from the initial scan. If no fouling occurred we would expect to see the same image as in Figure 5.10a. When employing a classical outer sphere redox mediator (as in Section 5.3) a repeat scan over the same area clearly shows the grain structure of pBDD. However, for the oxidation of serotonin, even though a film is formed after initial oxidation, still a significant current is passed compared with the initial scan (Figure 5.10b). This implies that the electrode has

been fouled by the deposition of a conducting film or a porous membrane. This fouling or film formation can be easily visualised with optical microscopy where a micrograph was taken after one scan had started (Figure 5.10c right side) and then after two images were completed (Figure 5.10c furthest left square). The optical images prove there is film formation when employing serotonin as the redox mediator which was not observed in the optical image when employing a classical outer sphere or 'simple' inner sphere redox mediator. This film or membrane becomes thicker after multiple scans demonstrating the progressive formation. Moreover, Figure 5.10d provides additional evidence for the fouling on pBDD where a topographical image has been taken.

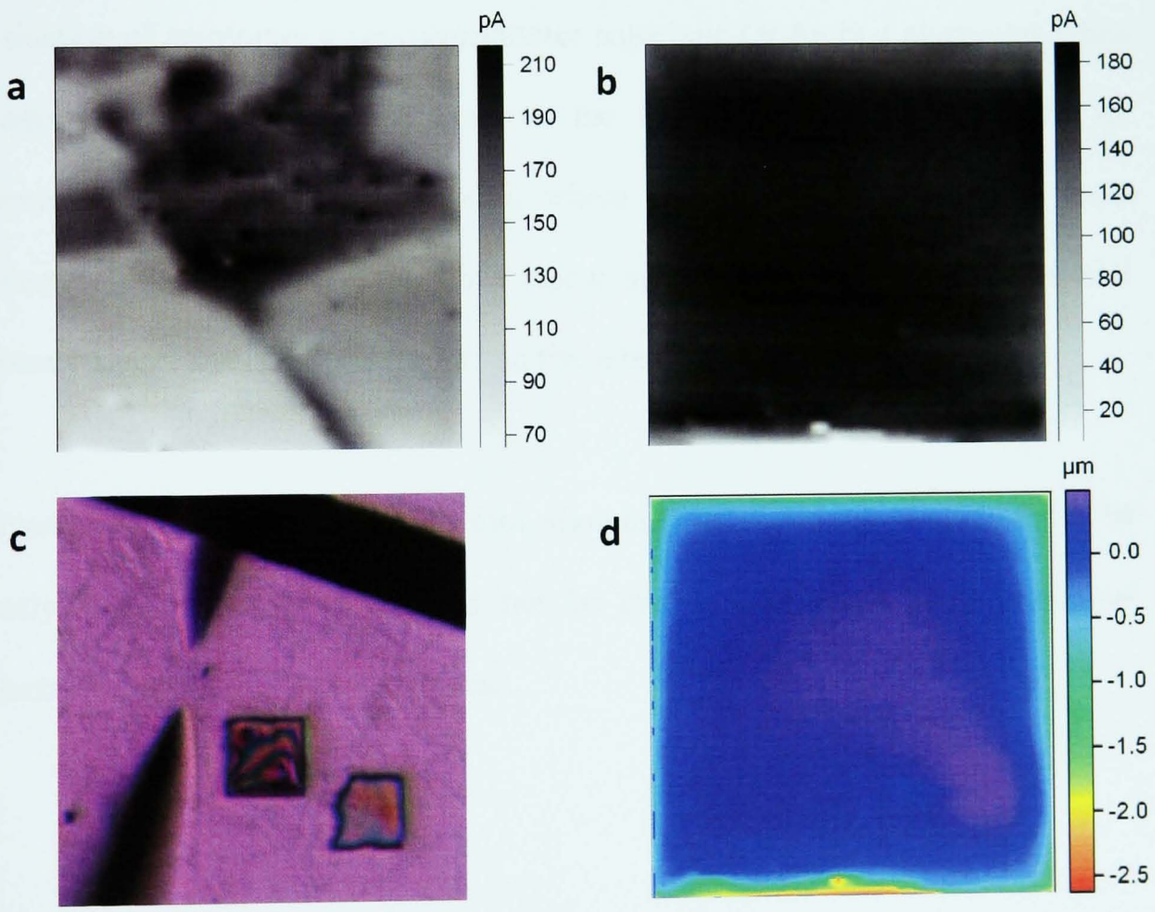

Figure 5.10 45 x 45 µm SECCM images showing the oxidation of 2 mM serotonin (650 mV at substrate) a) first image taken showing a clear effect of grain structure b) second image taken c) optical micrograph showing film formation after scanning d) topography image after second scan

5.7 Conclusion

SECCM is a new electrochemical imaging technique that provides a considerable amount of information on local electrochemical reactions. We have investigated reactions at pBDD using both classical outer sphere and inner sphere redox mediators. SECCM provides further evidence that the entire surface of pBDD is active with heterogeneity from grain to grain where boron uptake varies. Also, for the electron transfer of $FcTMA^+$, a classical outer sphere redox mediator, the corresponding standard rate constants (k^0) have been calculated, whereby each current pixel has been converted to k^0.

Another advantage of using SECCM has been demonstrated by mapping the oxidation of serotonin; a neurotransmitter notorious for fouling electrodes when performing electrochemistry. Due to the localised nature of SECCM an electrochemical image can be taken which clearly shows the inherent grain structure of pBDD. However, on a repeat scan either a conducting film or a porous membrane had been formed on the substrate.

Overall, SECCM is an exciting tool allowing for a variety of surfaces to be analysed which previously could not be due to limitations of conventional electrochemical imaging techniques.

5.8 REFERENCES

(1) Bard, A. J.; Fan, F. R. F.; Kwak, J.; Lev, O. *Anal. Chem.* **1989**, *61*, 132.

(2) Kwak, J.; Bard, A. J. *Anal. Chem.* **1989**, *61*, 1221.

(3) Kwak, J.; Bard, A. J. *Anal. Chem.* **1989**, *61*, 1794.

(4) Hansma, P. K.; Drake, B.; Marti, O.; Gould, S. A.; Prater, C. B. *Science* **1989**, *243*, 641.

(5) Macpherson, J. V.; Unwin, P. R. *Anal. Chem.* **1999**, *72*, 276.

(6) Takahashi, Y.; Shevchuk, A. I.; Novak, P.; Murakami, Y.; Shiku, H.; Korchev, Y. E.; Matsue, T. *J. Am. Chem. Soc.* **2010**, *132*, 10118.

(7) McKelvey, K.; Edwards, M. A.; Unwin, P. R. *Anal. Chem.* **2010**, *82*, 6334.

(8) Ebejer, N.; Schnippering, M.; Colburn, A. W.; Edwards, M. A.; Unwin, P. R. *Anal. Chem.* **2010**, *82*, 9141.

(9) Hutton, L.; Newton, M. E.; Unwin, P. R.; Macpherson, J. V. *Anal. Chem.* **2008**, *81*, 1023.

(10) Wilson, N. R.; Clewes, S. L.; Newton, M. E.; Unwin, P. R.; Macpherson, J. V. *J. Phys. Chem. B* **2006**, *110*, 5639.

(11) Colley, A. L.; Williams, C. G.; D'Haenens Johansson, U.; Newton, M. E.; Unwin, P. R.; Wilson, N. R.; Macpherson, J. V. *Anal. Chem.* **2006**, *78*, 2539.

(12) Lai, S. C. S.; Dudin, P. V.; Macpherson, J. V.; Unwin, P. R. *J. Am. Chem. Soc.* **2011**, *133*, 10744.

(13) Vasile, M. J.; Enke, C. G. *J. Electrochem. Soc.* **1965**, *112*, 865.

(14) Snowden, M. E.; Güell, A. G.; Ebejer, N.; Lai, S. C. S.; O'Connell, M. A.; McKelvey, K.; Colburn, A. W.; Unwin, P. R. *In Preparation.*

(15) Janssen, G.; van Enckevort, W. J. P.; Vollenberg, W.; Giling, L. J. *Diamond Relat. Mater.* **1992**, *1*, 789.

(16) Samlenski, R.; Haug, C.; Brenn, R.; Wild, C.; Locher, R.; Koidl, P. *Diamond Relat. Mater.* **1996**, *5*, 947.

(17) Spitsyn, B. V.; Bouilov, L. L.; Derjaguin, B. V. *J. Cryst. Growth* **1981**, *52*, 219.

(18) Neufeld, A.; O'Mullane, A. *J. Solid State Electrochem.* **2006**, *10*, 808.

(19) Holt, K. B.; Bard, A. J.; Show, Y.; Swain, G. M. *J. Phys. Chem. B* **2004**, *108*, 15117.

(20) Lagrange, J. P.; Deneuville, A.; Gheeraert, E. *Diamond Relat. Mater.* **1998**, *7*, 1390.

(21) Rao, T. N.; Tryk, D. A.; Hashimoto, K.; Fujishima, A. *J. Electrochem. Soc.* **1999**, *146*, 680.

(22) Shirafuji, J.; Sakamoto, Y.; Furukawa, A.; Shigeta, H.; Sugino, T. *Diamond Relat. Mater.* **1995**, *4*, 984.

(23) Thomas, R. E.; Rudder, R. A.; Markunas, R. J. *J. Vac. Sci. Technol., A* **1992**, *10*, 2451.

(24) Nebel, C. E.; Ristein, J. *Thin-Film Diamond II*; Elsevier Academic Press, 2004; Vol. 77.

(25) Chen, P.; McCreery, R. L. *Anal. Chem.* **1996**, *68*, 3958.

(26) Fischer, A. E.; Show, Y.; Swain, G. M. *Anal. Chem.* **2004**, *76*, 2553.

(27) Bard, A.; Faulkner, L. R. *Electrochemical Methods: Fundamentals and Applications, 2nd Edition* **2001**.

(28) Igbal, N.; van Praag, H. M. *Eur. Neuropsychopharmacol.* **1995**, *5*, 11.

(29) Sarada, B. V.; Rao, T. N.; Tryk, D. A.; Fujishima, A. *Anal. Chem.* **2000**, *72*, 1632.

(30) Wrona, M. Z.; Dryhurst, G. *The Journal of Organic Chemistry* **1987**, *52*, 2817.

(31) Wrona, M. Z.; Dryhurst, G. *Journal of Electroanalytical Chemistry and Interfacial Electrochemistry* **1990**, *278*, 249.

(32) Jackson, B. P.; Dietz, S. M.; Wightman, R. M. *Anal. Chem.* **1995**, *67*, 1115.

(33) Ewing, A. G.; Dayton, M. A.; Wightman, R. M. *Anal. Chem.* **1981**, *53*, 1842.

CHAPTER 6

POLYCRYSTALLINE BORON DOPED DIAMOND (PBDD) ROTATING DISK ELECTRODE (RDE): FABRICATION, CHARACTERISATION AND FUNCTIONALISATION FOR NANOPARTICLE ELECTROCATALYSIS

ABSTRACT

The fabrication of polycrystalline boron doped diamond (pBDD) rotating disk electrodes (RDE) are reported. Various insulating sheaths have been explored including a variety of resins and polytetrafluoroethylene (PTFE). The RDEs were electrochemically tested with two redox mediators both in stationary solutions and by rotating. The pBDD RDEs fabricated using PTFE showed to be the most promising material, particularly for employing the electrode to investigate reactions in the proton exchange membrane fuel cell (PEMFC) environments with acidic conditions.

The 'pristine' pBDD employed in this work is an excellent material for use as a support for the electrodeposition of Pt nanoparticles (NPs). It has low background currents, which show no evidence for the oxygen reduction reaction (ORR) during electrochemical measurements. The surface of the pBDD is flat; where NP size and coverage can be determined using atomic force microscopy (AFM) as the pBDD RDE can be directly imaged.

The fabricated pBDD RDE functionalised with Pt NPs has been compared with a bulk Pt RDE for the ORR. It was concluded that on short timescales the reaction predominantly occurs via a four electron transfer mechanism, with a small contribution from the two electron transfer mechanism. However, on longer timescales the two electron transfer reaction dominates.

6.1 INTRODUCTION

An increased awareness of the limited supply of fossil fuels has prompted a renewed interest in alternative energy sources. Proton exchange membrane fuel cells (PEMFC)[1,2] operating at 'low' temperature (< 80 °C) are generally considered to be one of the most promising technologies. In a PEMFC, the fuel is oxidised at the anode, releasing electrons which flow through an external circuit to the cathode, where the oxidant is reduced. A range of molecules are being studied for their potential use as a fuel in the PEMFC (such as hydrogen or small organic molecules), however the choice of the reactant at the cathode is limited to oxygen. Although the oxygen reduction reaction (ORR) has been studied extensively, several outstanding issues remain, limiting the performance of PEMFCs and inhibiting their widespread commercialisation.

The electrocatalyst support is another issue: to maximise metal utilisation, the Pt or Pt-based electrocatalyst is dispersed on a carbon support material (such as carbon black) in the form of nanoparticles. However, degradation of the supported electrocatalyst can readily occur during operation through nanoparticle sintering, decreasing the metal surface area,[3] carbon corrosion causing the dislodging of particles,[4] and potential cycling induced particle dissolution.[5] To minimise these causes of degradation, alternative materials as a support for Pt based electrocatalysts are sought, which offer an increased resistance to corrosion and stronger particle bonding. Studied materials include boron doped carbon,[6] nitrogen doped carbon,[7] graphite,[8,9] carbon nanotubes[10,11] and (polycrystalline) boron doped diamond[12].

In many respects, polycrystalline boron doped diamond (pBDD) would be an ideal catalyst support material, as it offers low background currents (thus minimising undesired side processes), resistance to corrosion under acidic and alkaline conditions, and an increased stability at both high temperature and pressure.[13-15] In addition, platinum-modified pBDD has already been shown as an excellent quantitative oxygen sensor, in which there was no detected electrochemical response for ORR from pBDD alone in a particular potential range.[12] pBDD has also been employed previously for the investigation of oxygen reduction in alkaline solutions.[16]

Although there have been previous studies employing BDD electrodes to investigate the ORR, to the best of our knowledge no work has yet been reported on the fabrication of a rotating disk electrode showing full electrochemical testing, before applying this method to study the ORR by functionalisation with metal nanoparticles. The RDE is proving to be a key tool for the assessment of nanoparticle electrocatalysts.[17-20]

A thin film BDD turbine cell has been used,[21] as well as a modified RDE[22] to study the ORR however the fabrication here was not fully explored. In addition to these, many other BDD electrodes employed for the investigation of the ORR are fabricated using H-terminated diamond[23] or diamond which possesses a large amount of sp^2 carbon. H-terminated BDD is undesirable as it is unstable[24] in both acidic conditions and when the potential is swept positive;[25] a property which could be used if the BDD was modified using Pt nanoparticles and they needed to be electrochemically cleaned. Furthermore, a desirable property of BDD for its use of studying catalytic processes is that it is insensitive to ORR

during certain potential ranges. The addition of sp^2 carbon provides a substrate where the ORR can occur shown by the addition of this during the growth process.[26]

In this chapter, we report the fabrication of a platinum functionalised pBDD rotating disc electrode (RDE), which has been electrochemically tested. Furthermore, the pBDD employed is oxygen terminated, has very little sp^2 content as well as being polished allowing for AFM characterisation when the surface is functionalised. We will show that this electrode can be employed to obtain fundamental information on the ORR with increased mass transport rates.

6.2 pBDD RDE: Fabrication and Electrochemical Characterisation

Although a few rotating disk electrodes fabricated from pBDD are commercially available, they are poorly suited for fundamental studies of the ORR using the environment analogous to a PEMFC. For example, some of these commercially available electrodes show impeded electron transfer, while others have a relatively high surface roughness (due to certain grains of the pBDD protruding) (Adamant®-RDE, Element 6 RDE). As the pBDD-RDE has to be functionalised for the ORR, these factors could result in non-uniform nanoparticle (NP) deposition, especially for the electrodeposition of NP catalysts. Furthermore, NP characterisation would be challenging as most quantitative characterisation techniques, such as atomic force microscopy (AFM), require a flat surface. Therefore, rather than employing a commercially available electrode, we have chosen to fabricate a pBDD-RDE in-house using 2 mm diameter pBDD disk

produced by laser micromachining.[12] The disk was electrically connected by creating a Ti (20 nm) / Au (400 nm) ohmic back contact using a sputterer (Moorfield Minibox Conversion), before using silver epoxy to contact this to the screw exterior. To avoid exposure of the back contact and to maintain a good alignment, it was necessary to encapsulate the disk in an insulating sheath (Figure 6.1).

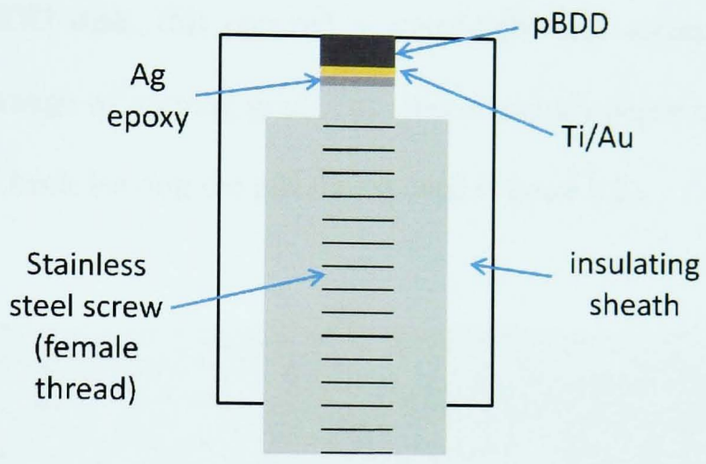

Figure 6.1 Schematic of the RDE

Several materials can be employed to create the insulating sheath depending on the desired application. In order to be employed for ORR (or other PEMFC reactions) studies, the material needs to be stable under operating conditions typical for PEMFC application; high acidity and temperatures. In elevated temperatures, ORR kinetics are enhanced[27] and the adsorption of the poisoning species is weakened.[28] While operating in these harsh conditions it is particularly important to maintain a water tight seal around the pBDD disk. In this study, two types of material have been investigated for the insulating sheath of the RDE; namely resins and polytetrafluoroethylene (PTFE).

6.2.1 RESIN INSULATING SHEATH

Several resins were tested as the material for the insulating sheath. In all cases, the RDE was fabricated as follows. The Ti/Au sputtered pBDD disk was contacted to a stainless steel cylinder, possessing an internal thread, using silver loaded epoxy. This was then placed, with the disk facing down, into a PTFE mould and resin was poured around this. As the resin directly set and cured around the pBDD disk, this ensured a water-tight seal around the electrode. After curing a range of varying grades of silicon carbide paper was employed to polish the resin back leaving the pBDD exposed (Figure 6.2).

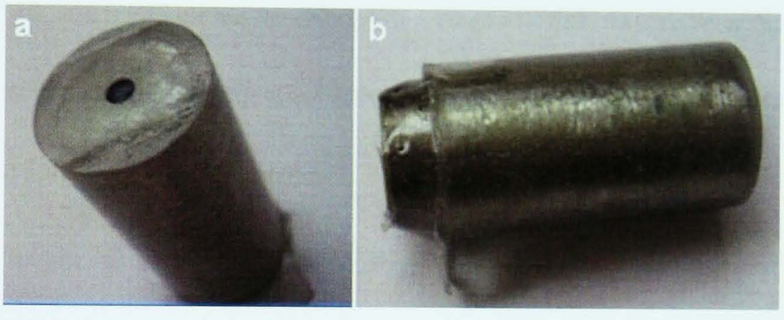

Figure 6.2 Example of a pBDD RDE fabricated using resin for the insulating material a) top view b) side view

Electrodes were fabricated with a variety of resins (epoxy and the hardener) or adhesives including DR2188/HY2188 (Delta Resin, UK), CY29/HY30 (Delta Resin, UK), 9323B/A (3M Scotch-Weld, UK) and Norland Optical Adhesive 81 (Norland, NJ). These were then polished and electrochemically tested. For most of the resins, on repeat cycling of the potential, in a given redox mediator, the peak current deteriorated, an indication of leaching where the resin could be soluble in solution and causing the active electrode to foul. This effect was particularly pronounced when taking the electrode up to elevated temperatures

common for fuel cell applications. The most promising resin tested was prepared from HY2188 hardener and DR2188 epoxy (Delta Resins, UK), which is used commercially as a radiator sealant, indicating its heat-resistance, therefore maintaining a seal to the pBDD disk at high temperatures. In addition, there was less tendency for this resin to leach, blocking the active pBDD surface.

After polishing, the pBDD-RDE was tested electrochemically to ensure if the electrical contact is maintained and to verify the quality of the seal. Initially the potentials were swept from extreme positive to negative values, showing the background currents in 0.1 M KCl to ensure there was no sloping evident in the response due to high resistances present. In addition, background currents also give an indication of the quality of the pBDD (which, in theory, fully consist of sp^3 hybridised carbon). Low currents with a wide potential window could imply there is little or no sp^2 carbon present in the sample. The pBDD employed here is also tested for the presence of sp^2 carbon using Raman spectroscopy, which proved there was a minimal amount present in the sample. This becomes increasingly important as it will influence any electrochemical response observed, particularly in the case of the ORR. Resistance may be introduced due to a poor ohmic contact, due to resin leaching or through a poor seal around the electrode. Typical cyclic voltammograms (CV) using the simple outer sphere redox mediator, ferrocenylmethyltrimethylammonium ($FcTMA^+$), are shown in (Figure 6.3).

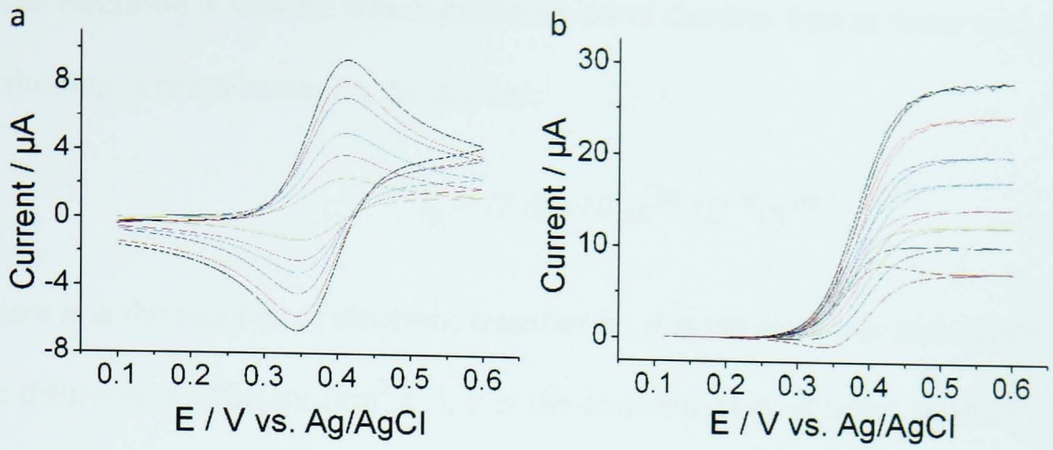

Figure 6.3 Cyclic voltammograms of epoxy sealed pBDD RDE to show reversible electrochemistry (1 mM FcTMA+ in 0.1 M KCl) at a) various scan rates under stationary conditions (V/s) – 0.2 – 0.15 –0.1 –0.15 –0.03 –0.01 b) various rotation speeds (RPM) – 4003 – 3003 –2004 –1502 –1005 –749 –501 –249

Figure 6.3a shows the voltammetric profiles under stationary conditions at room temperature (22 °C) recorded at various scan rates. This CV shows a steady increase in current when the potentials are swept in the positive direction, where $FcTMA^{+}$ becomes oxidised to $FcTMA^{2+}$, until a maximum peak current (i_p) is achieved. After the maximum is reached the current then begins to fall as there is a depletion of the mediator close to the surface of the electrode, showing a diffusion-limited response. The experimental peak currents were in accordance with the Randles-Sevcik (Equation 6.1). In particular the measured currents were as expected when the size of the electrode, mediator concentration, diffusion coefficient and scan rate were taken into account. This indicated that the electrode seal was sufficient, with no solution leaking between the resin and pBDD disk. Various scan rates were employed to ensure there was a linear relationship between the i_p and the square root of the scan rate (according to Equation 6.1). When the scan rate is decreased, the potential sweep takes longer to perform, which allows for a thicker diffusion layer to form. Therefore the flux

to the electrode is smaller which produces lower currents than at faster scan rates, as the flux is proportional to the current.

$$i_p = (2.69\times10^5)n^{3/2}AD^{1/2}cv^{1/2} \qquad (6.1)$$

where n is the number of electrons transferred, A is the electrode area (cm^2), D is the diffusion coefficient ($cm^2\ s^{-1}$), c is the concentration of redox mediator (mol cm^{-3}) and v is the scan rate ($V\ s^{-1}$)

Voltammograms recorded at different rotation rates (generally slow scan rates were employed, < 5 mV s^{-1}) are shown in Figure 6.3b where we observe a limiting current (i_{lim}) instead of a i_p. When the electrode is rotating the system is not limited by diffusion because rotation of the electrode ensures a constant supply of fresh solution, replenishing redox mediator at the surface of the electrode. Hence we observe a steady current at the more positive potentials for the oxidation of $FcTMA^+$. This steady-state current increases linearly with the square root of the rotation speed, according to the Levich equation:

$$i_{lim} = 0.620nAFD^{2/3}\omega^{1/2}\nu^{-1/6}c \qquad (6.2)$$

where i_{lim} is the limiting current, n is the number of electrons, A is the electrode area, F is the Faraday constant, D is the diffusion coefficient, ω is the angular rotation speed ($\omega = 2\pi f/60$ where f is the rotation speed in RPM), ν is the kinematic viscosity and c is the bulk concentration.

The electrode was then further tested by increasing the temperature of solution (1 mM $FcTMA^+$ and 0.1 M KCl) from room temperature up to 69°C. The peak to peak separation changed according to Equation 6.3 and currents observed were in accordance to theory, demonstrating that the resin seal to the pBDD was

sufficient at the higher temperature range. There was no evidence of the seal failing which would have caused solution to leak between the resin and pBDD reaching the Au contact, which would produce an increase in current when performing CV and also cause a change on the peak to peak separation.

$$\Delta E_p = 2.303RT/nF \tag{6.3}$$

where ΔE_p is the peak to peak separation, R the gas constant (J mol^{-1} K^{-1}) and T is the temperature (K).

6.2.2 Polytetrafluoroethylene (PTFE) Insulating Sheath

For many commercially available RDEs insulating sheaths are fabricated using polytetrafluoroethylene (PTFE) due to its high thermal and chemical resistance.[29] However, achieving and maintaining a good seal with PTFE can be challenging not only because it was not in a liquid form which could be easily set around the electrode, but also because of the thermal expansion, which would occur during the machining process before the electrode would be considered for use electrochemically. Two methods were explored to sheath the pBDD disk in the RDE. Initially, the PTFE sheathed pBDD-RDE was fabricated similar to the resin sheathed RDE: the pBDD was connected to the screw with Ag which was left to dry for 24 hours. An interference fit (where the casing, PTFE has an inner diameter smaller than the outer diameter of the screw), was then used by pushing the screw and pBDD through a PTFE case (Figure 6.1). The PTFE was polished back with silicon carbide paper to expose the pBDD disk and tested in an electrochemical set-up.

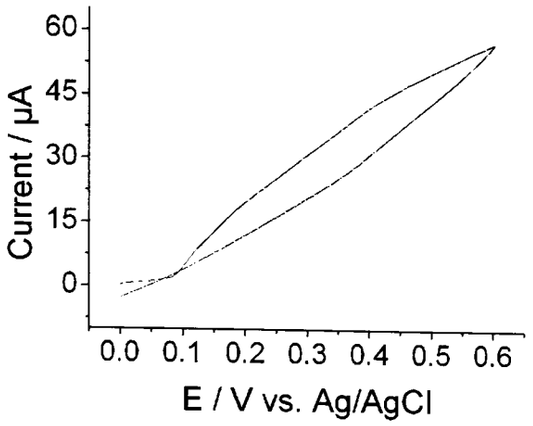

Figure 6.4 Cyclic voltammograms 1 mM $FcTMA^+$ in 0.1 M KCl to test the PTFE pBDD RDE

The resulting voltammogram can be seen in Figure 6.4. By comparing this CV to Figure 6.3a it is immediately evident that the CV of the PTFE sheathed pBDD–RDE shows a strong deviation from the ideal behaviour. This could be attributed to a poor electrode seal and therefore an alternative method of sheathing the BDD in PTFE is explored. The pBDD and insulating sheath were compressed using a collet connected to a lathe. A lathe is a piece of machinery that can be used to rotate an object whilst cutting. The collet is used to hold that object by applying a clamping force around it. The electrode was then re-polished and the resulting electrochemical response can be seen in Figure 6.5a.

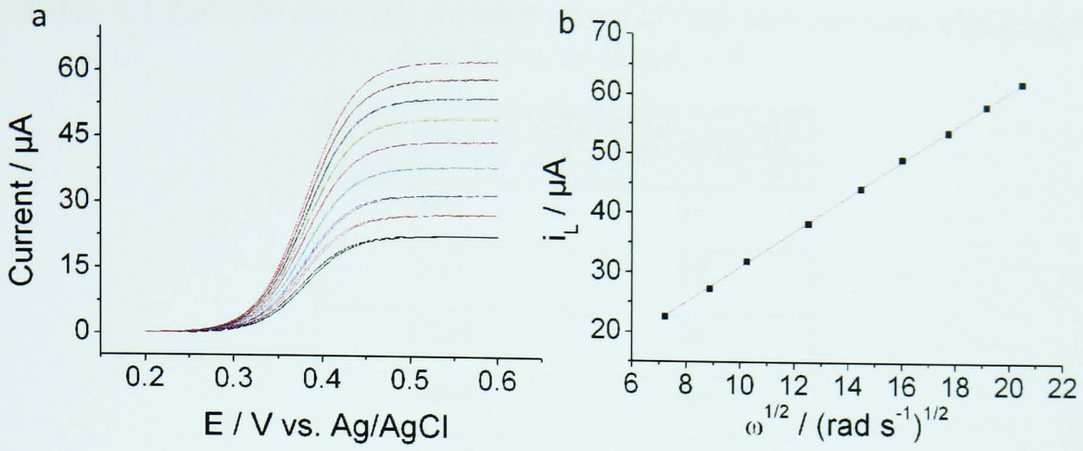

Figure 6.5 a) Example of the electrochemical response of PTFE sealed pBDD RDE showing the oxidation of 1 mM $FcTMA^+$ (10 mV /s) whilst varying the rotation speeds– 501 – 751 –1003 –1498 –2000 –2449 –3000 –3503 –4003 b) Levich plot to show the effect of limiting current with rotation speed, ω

The effect of compression on the PTFE shows a vast difference in the electrochemical response. For the oxidation of 1 mM $FcTMA^+$ the limiting currents are in accordance with the Levich equation, with $E_{3/4}$-$E_{1/4}$ (equivalent to ΔE_p for a purely diffusion limited process) showing reversible behaviour at various rotation speeds (Table 6.1) and there is also reduced hysteresis compared with the fabricated resin RDE. There is a clear linear relationship between the limiting current and the square root of the angular rotation speed, in correspondence with the Levich equation (Equation 6.2).

Table 6.1 Table to show the rotation speed (RPM) with the reversibility from data shown in Figure 6.5

RPM	$E_{3/4}$-$E_{1/4}$ (mV)
501	58
751	59
1003	59
1498	60
2000	60
2499	60
3000	60
3503	61
4003	61

6.3 FUNCTIONALISATION OF THE PBDD RDE

The ORR suffers from sluggish kinetics and requires significant overpotentials to take place, directly impacting the maximum power output from a PEMFC. On platinum[30] and platinum-based materials,[31,32] generally considered to be the most promising electrocatalytic materials, the ORR can occur through several pathways:

$$O_2 + 4H^+ + 4e^- \rightarrow 2H_2O \quad (6.4)$$

$$O_2 + 2H^+ + 2e^- \rightarrow H_2O_2 \quad (6.5)$$

$$H_2O_2 + 2H^+ + 2e^- \rightarrow 2H_2O \quad (6.6)$$

In the direct reaction pathway (Equation 6.4), oxygen is reduced to water via a four electron process. In the indirect pathway, oxygen is first reduced to hydrogen peroxide (Equation 6.5) in a two-electron process. The formed hydrogen peroxide produced in Equation 6.5 can either diffuse into the bulk of

the electrolyte, or be further reduced to water (Equation 6.6) in another two-electron process.[33-36] In PEMFC research, the desired product is water rather than hydrogen peroxide, as this not only maximises energy output, but hydrogen peroxide is also undesired as it can corrode the electrolyte or the membrane in a PEMFC.[37] Therefore, understanding of the factors influencing the reaction pathways and the electron transfer kinetics of the ORR is of utmost importance.

In order to study the oxygen reduction reaction, the pBDD-RDE was functionalised by electrodepositing Pt NPs from a solution of 1 mM K_2PtCl_6 in 0.1 M HCl with varying deposition parameters (*vide infra*). Typical voltammograms obtained on pBDD before and after functionalisation with Pt NPs are shown in Figure 6.6. As can be seen in Figure 6.6a, bare (non-functionalised) pBDD has very low background currents and there is no clear signal for the reduction of oxygen in the potential range from -1.5 V to 1.5 V - the signals at *ca.* 1.5 V and -1.5 V (vs. Ag/AgCl) can be attributed to the formation of oxygen and hydrogen, respectively. This is a further indication that the pBDD employed is of high quality, with little or no sp^2 carbon present, as discussed previously (Chapter 4). After functionalisation with Pt NPs (Figure 6.6b), a reduction wave with an onset potential at 0 V and a peak potential at *ca.* -0.2 V, related to the reduction of oxygen, can clearly be resolved. The feature can be assigned to the reduction of oxygen at the platinum NPs.[12]

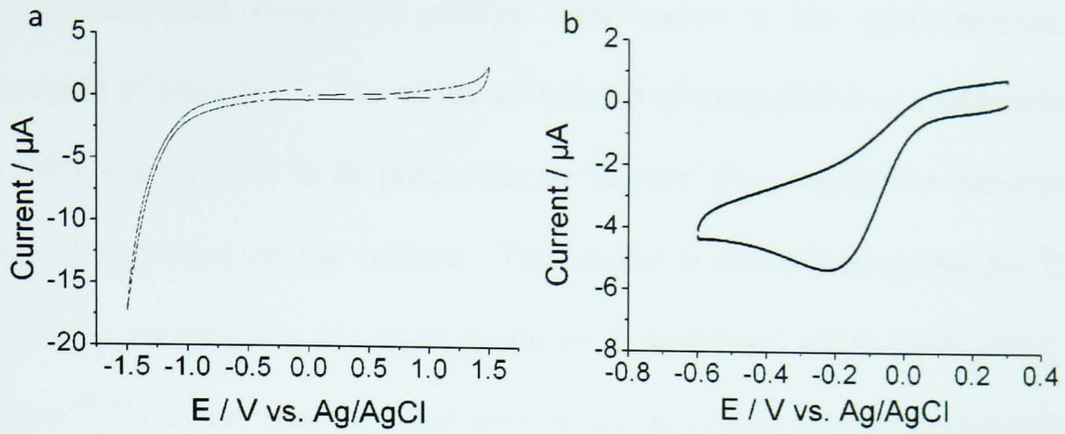

Figure 6.6 CV showing absence and presence of the ORR using 0.5 M H_2SO_4 on a) pBDD b) pBDD modified with Pt NPs using a scan rate of 0.1 V/s

6.3.1 Particle Deposition and Stability on pBDD

Platinum NPs were initially electrodeposited onto the substrate using a deposition potential of -1 V (vs. SCE) for 5 sec. The electrodeposited Pt NPs were characterized using peak force mode AFM. Typical AFM images are shown in Figure 6.7. The NPs have an average height of 16.3 ± 7.7 nm (determined using SPIP software, Image Metrology) and are dispersed uniformly on the pBDD, with a few agglomerates present.

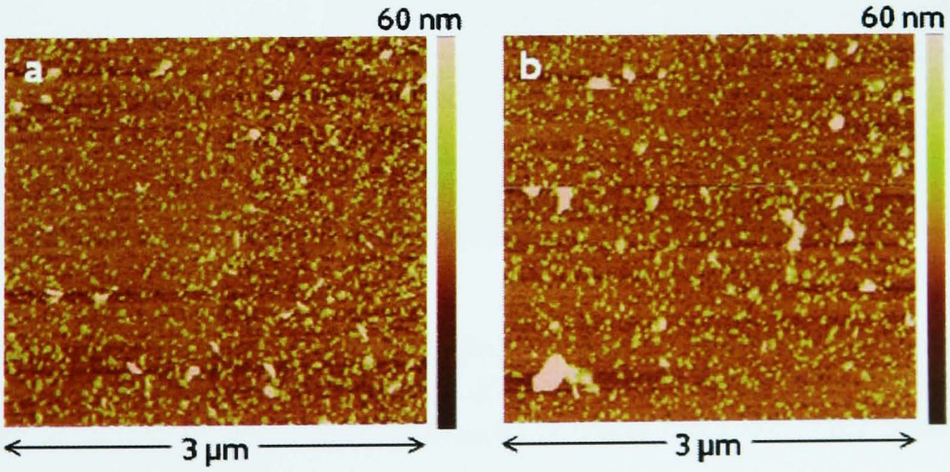

Figure 6.7 Images showing different areas of the pBDD disk of the RDE after deposition of particles a) middle of pBDD b) edge of pBDD. The average height of particles are 16.3 nm ± 7.7 nm

One of the main causes of catalyst deactivation is the agglomeration or dislodging of particles.[38] One of the advantages of using pBDD as a substrate for the ORR reaction lies in its propensity to 'anchor' Pt nanoparticles effectively, immobilising them on the surface. This ability is also advantageous for RDE studies, as rotating the electrode produces a significant shear force along the surface.[39] To ensure that extended rotation did not cause particle agglomeration or dislodging, the Pt NP functionalised pBDD RDE was rotated at 4000 RPM for 45 minutes. AFM images were taken before (Figure 6.8a) and after rotation (Figure 6.8b). It is evident that the particles are neither removed nor is there extensive aggregation upon rotation which could affect the catalytic activity and compromise results.[40,41]

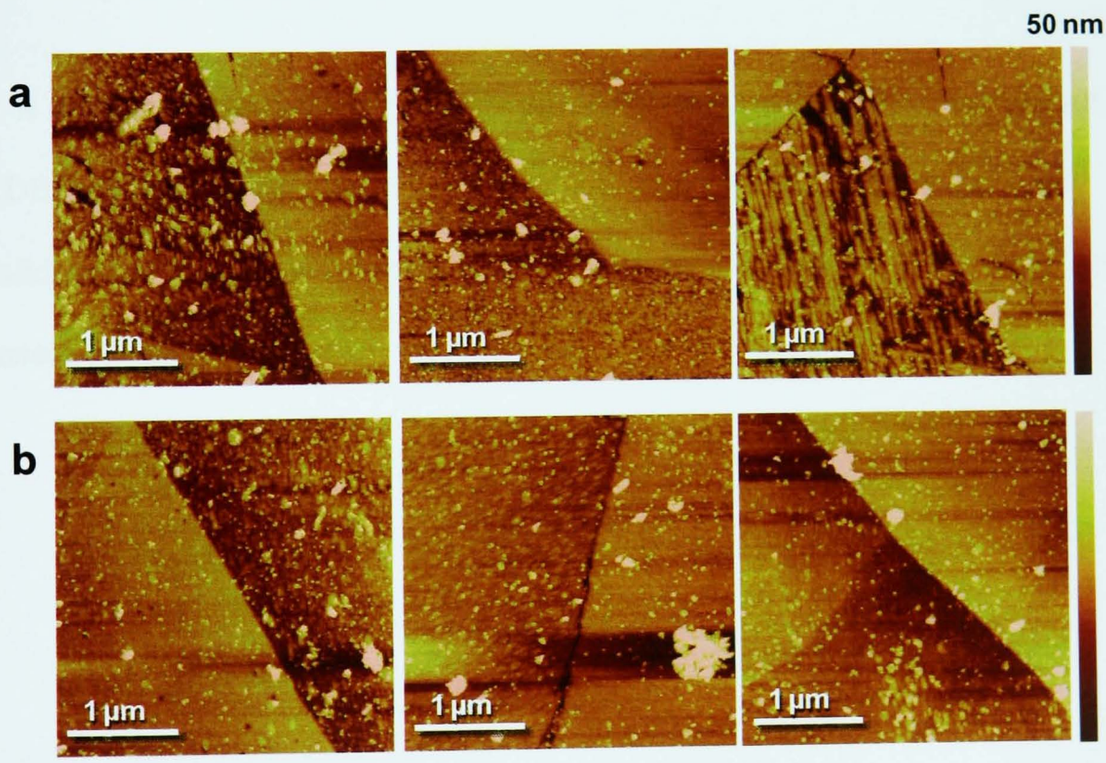

Figure 6.8 AFM images showing the effect of shear force on the electrodeposited particles a) before rotation of the RDE b) after rotation at 4000 RPM for 45 minutes. It should be noted that the images in a and b are not of the same areas.

As the pBDD-RDEs are time-consuming to fabricate, it was also important to verify that the deposited NPs could be stripped easily to ensure easy re-usability of the pBDD-RDE. A common cleaning method (both for RDEs and pBDD electrodes) is polishing the electrode surface with an alumina suspension. Therefore, the Pt NP functionalised pBDD-RDE was subjected to alumina polishing.[42] AFM images of the pBDD were taken before Pt-deposition, after deposition and after subsequent polishing. AFM images over extended areas (Figure 6.9ai and bi) and zoom-ins on grain boundaries (Figure 6.9aii and bii) show no evidence for residual Pt NPs once polishing was performed after the deposition of particles, indicating that the pBDD-RDE can be effectively cleaned by alumina polishing.

It is to be noted that the removal of particles by alumina polish, after the resin RDE had been heated and cooled to room temperature, was unsuccessful. A valid reason for this observation is that at high temperature the acidic conditions caused leaching of the resin, forming a thin layer over the NPs.

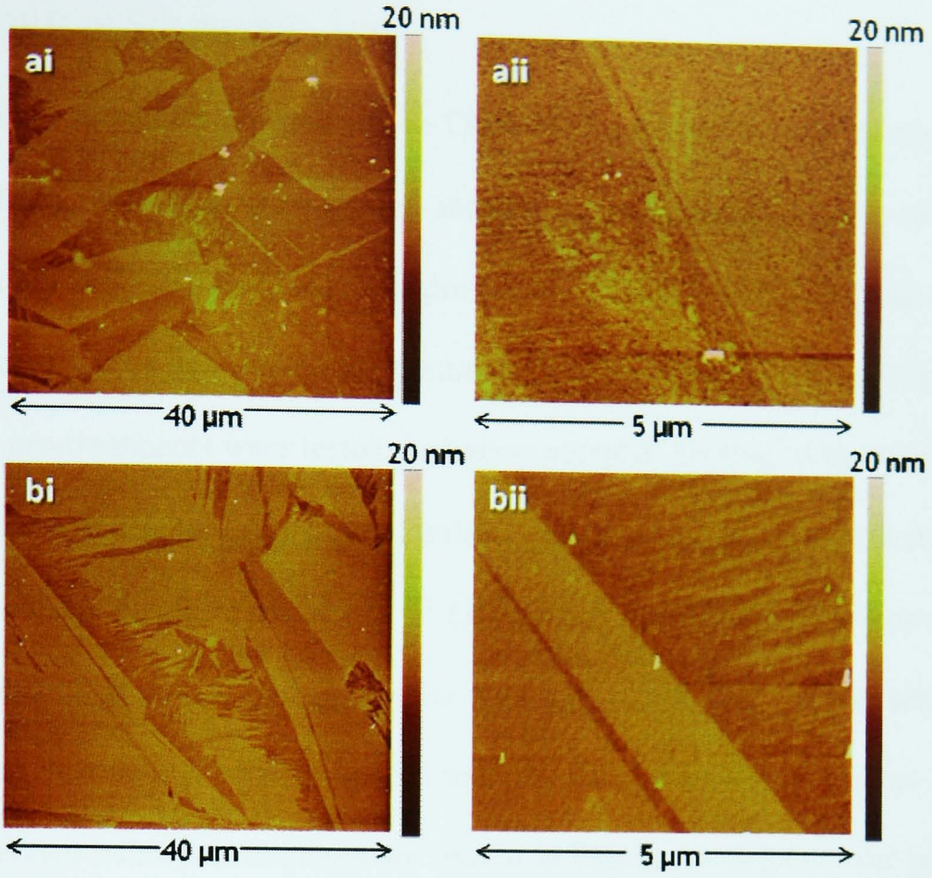

Figure 6.9 a) large areas ai) and smaller areas aii) of the pBDD before the electrodeposition of Pt NPs and b) large areas bi) and smaller areas bii) of the pBDD after alumina polishing the electrode

6.4 Oxygen reduction on a Pt NP functionalised pBDD RDE

Using the Pt NP functionalised pBDD-RDE we have investigated the ORR in a sulphuric acid solution, in which anion adsorption could play a role,[43] and in a perchloric acid solution, where anion adsorption is negligible. Anions adsorbed onto the surface of Pt can decrease the overall fuel cell performance.[44-46] Results obtained on the Pt NP functionalised pBDD-RDE with various NP sizes will be compared with results on a (bulk) platinum RDE, illustrating the effect of electrode morphology in studying the ORR.

6.4.1 ORR IN SULPHURIC ACID

In order to provide a comparison to ORR results on the Pt NP functionalised pBDD-RDE, the ORR was studied initially in an aerated solution of 0.5 M H_2SO_4 on a Pt RDE. As platinum is prone to adsorbing ambient organic species, the electrode was pre-treated to ensure consistent initial working conditions. Several pre-treatments were tested, including potential cycling[5] with various scan rates, potential limits, and potential pulses. The optimal conditions were found to be holding the electrode at 1.8 V (10 sec) to oxidatively strip any organic contaminants, followed by holding the potential at 0.2 V (5 sec) to reduce the produced Pt oxide. Voltammograms recorded at various rotation rates directly after this two pulse pre-treatment are shown in Figure 6.10a (Note: the reference electrode employed from here on was a SCE). From the Levich equation, a Levich plot (Figure 6.10b) can be constructed. Values of i_{lim} were taken from the reverse scan (anodic) at 0.3 V. From the plot, the effective number of electrons (n_{eff}) transferred can be derived from the slope to be 2.5 per oxygen molecule, indicating the main reaction product is hydrogen peroxide (2 electrons) rather than water (4 electrons).[43] This finding may be attributed to the binding of (bi-) sulphate to extended platinum surfaces (terraces with long-range order),[47] which steers the ORR product towards hydrogen peroxide.[48,49] This may be attributed to a blocking of sites on the platinum surface, which may either inhibit the direct pathway to water (Equation 6.1) or reduced re-adsorption and further reduction of produced hydrogen peroxide (Equation 6.3).[50]

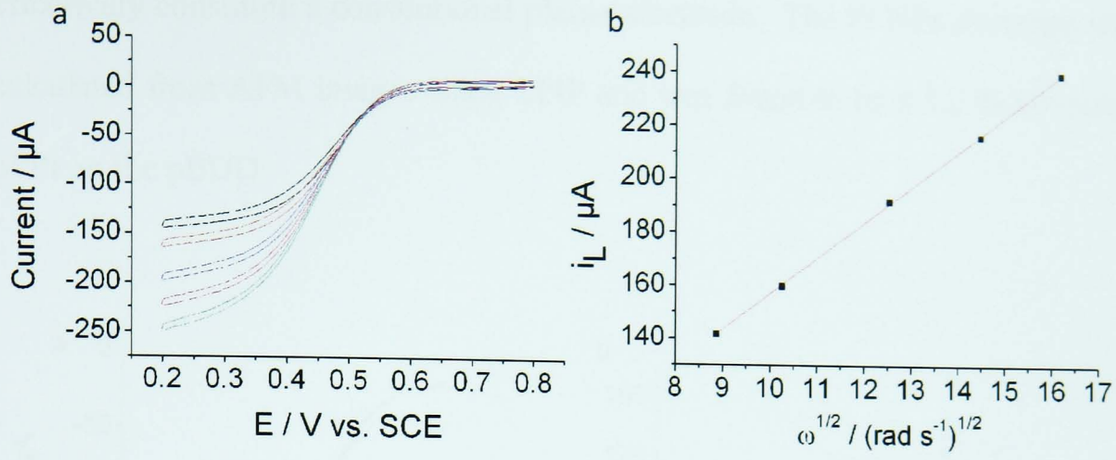

Figure 6.10 a) CV showing the ORR at a Pt RDE taken at different rotation speeds – 753 – 1005 –1499 –2002 –2501 b) A Levich plot showing the limiting current as a function of rotation speed

Voltammetric curves of the ORR on a Pt NP functionalised pBDD-RDE (Pt deposited at -0.6V for 20 s from 1 mM K_2PtCl_6 in 0.1 M HCl) are shown in Figure 6.11a. Comparing these curves with those on bulk Pt, it is evident that the current shows the same general potential dependence. However, from the Levich plot (Figure 6.11b) the apparent number of electrons transferred in this reaction was 4, indicating the main reaction product to be water rather than hydrogen peroxide. However, the ORR curves in Figure 6.11a do have an interesting wave shape. This could indicate that at potentials from *ca.* 0.4 V to 0 V the ORR reaction occurs via a four electron pathway, with contribution from the 2 electron pathway at potentials *ca.* 0 V to -0.2 V. Beyond this, hydrogen adsorption occurs. This difference with bulk platinum can again be attributed to (bi-sulphate) adsorption, as NPs of this size contain a very small amount of extended terraces available for sulphate adsorption. Additionally, when the area of the electrode was calculated using the Levich equation it was equal to the size of the pBDD disk. This implies that the NPs electrodeposited onto the pBDD must have been of a high enough density for diffusional overlap, where the NPs together

effectively constitute a conventional planar electrode. The Pt NPs coverage was calculated from AFM images using SPIP and was found to be a 1.2 % coverage of Pt on the pBDD.

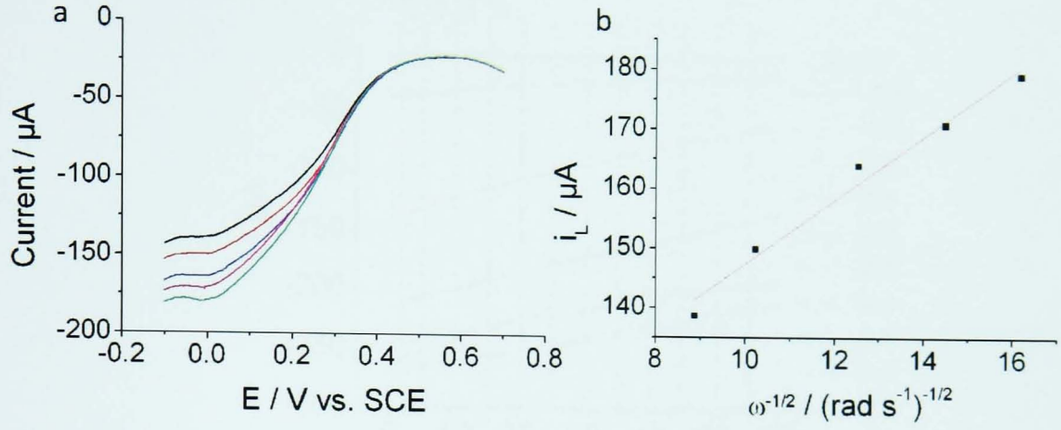

Figure 6.11 a) CV showing the ORR at the pBDD RDE taken at different rotation speeds – 752 – 1000 –1502 –2005 –2505 b) A Levich plot showing the limiting current as a function of rotation speed

As mentioned above, platinum is quite prone to deactivation, for example due to the adsorption of trace amounts of organic species which may be present in solution. As a result, repeating ORR voltammograms at the Pt NPs showed a decrease in currents, even when the electrode is pre-treated. In order to study the timescales involved in this deactivation process under increased mass transport (due to convection), chronoamperometry was employed to investigate the ORR on both the bulk Pt electrode and the functionalised pBDD electrode.

The experiments were set up as follows: the potential was initially stepped from 0.6 V (vs. SCE) to a final potential between -0.3 V and -0.6 V (vs. SCE) while the electrode was rotated at 3000 RPM. From the resulting current-time transients, current-potential relationships at different time points were

constructed by taking the currents at a given time on the various transients (Figure 6.12 Chronoamperometric curves showing the corresponding potentials applied at the substrate. Data at various time points t1, t2...tx were taken to construct graphs showing current-potential relationships (vide infra)Figure 6.12).

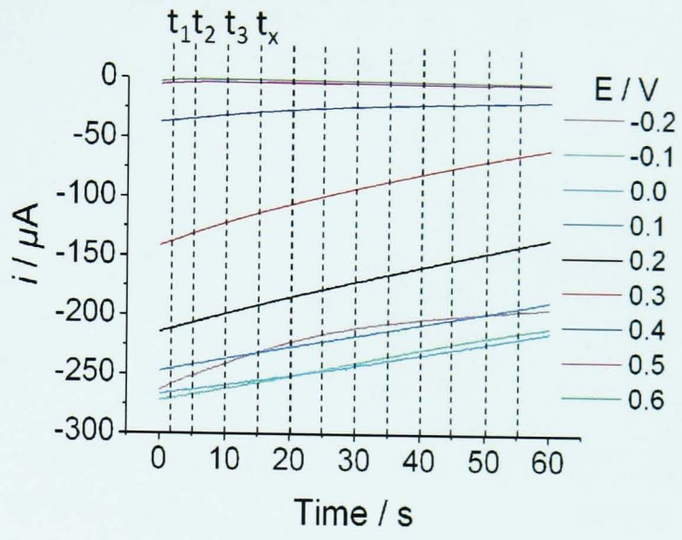

Figure 6.12 Chronoamperometric curves showing the corresponding potentials applied at the substrate. Data at various time points t_1, t_2...t_x were taken to construct graphs showing current-potential relationships (*vide infra*)

The resulting time-dependent current-potential plots can be seen in Figure 6.13. The response for the ORR on the bulk Pt RDE is similar to that observed when CVs were recorded directly after a cleaning pre-treatment. Considering the number of electrons transferred (see above), this indicates that the main reaction product on the bulk Pt RDE over the entire potential range is hydrogen peroxide, with a minimal deactivation on this timescale. On the Pt NPs functionalised pBDD-RDE, however, a potential dependence that is very different to the first few CVs can be observed, which is most likely indicative of hydrogen peroxide formation. However, some previous literature demonstrates that the same mechanism for the reduction of O_2 occurs on both bulk Pt and Pt NPs.[49]

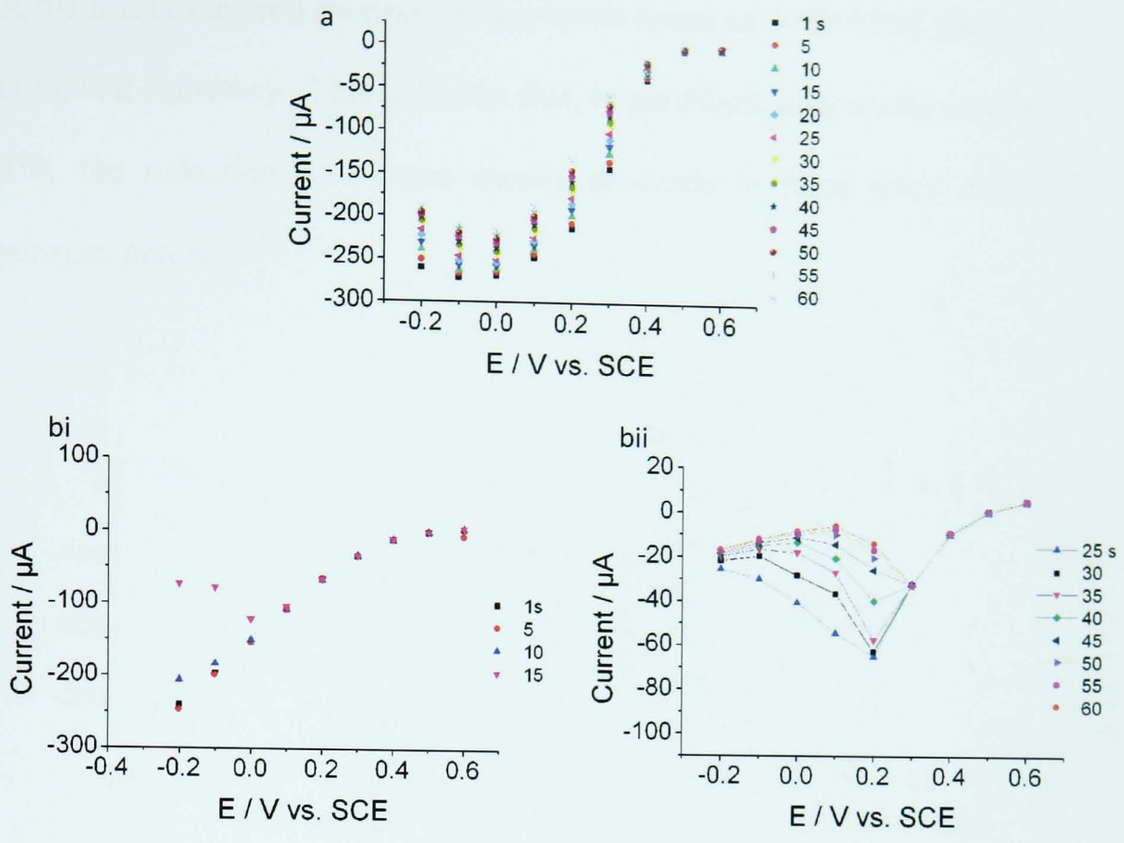

Figure 6.13 Current response at various times from chronoamperometry for the ORR on a) bare Pt RDE b) Pt NPs on pBDD RDE i) short timescales ii) longer timescales

6.4.2 ORR IN PERCHLORIC ACID

As (bi-) sulphate is known to adsorb strongly on (extended) platinum surfaces, particularly at higher flux, the same experiments were performed using perchloric acid as supporting electrolyte to study the effects of anion adsorption on the ORR on a Pt NP functionalised pBDD-RDE. Current-potential plots derived from chronoamperometric measurements (see previous section) employing an aerated 0.1 M $HClO_4$ solution are shown in (Figure 6.14). On the bulk Pt RDE (Figure 6.14a), the shape of the current-potential curve is similar to those in obtained in sulphuric acid. The currents are, however, roughly twice the magnitude, with a small decay over this timescale. Particularly, the limiting currents on the bulk Pt RDE correspond closely to the theoretical value of 343

μA for a four electron process for a rotation speed of 3000 RPM (derived from the Levich equation). This indicates that, in perchloric acid media on a bulk Pt-RDE, the reduction of oxygen mostly proceeds to form water rather than hydrogen peroxide.[51]

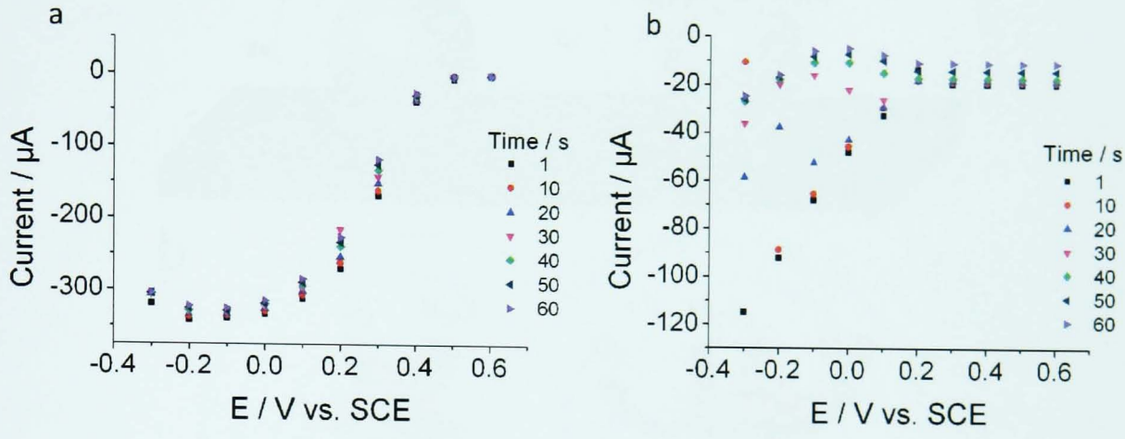

Figure 6.14 Current response at various times from chronoamperometry for the ORR using 0.1 M $HClO_4$ on a) bare Pt RDE b) Pt NPs on pBDD RDE

The time-dependent current-potential curves on the Pt NP functionalised pBDD-RDE shows very different behaviour. Initially, the currents increase with increasing overpotential. However, the currents decrease rapidly within 60 seconds, similar to the behaviour seen in sulphuric acid. As NPs of this size are very sensitive to poisoning, this deactivation is most likely related to the rapid blocking of active sites on the NP surface by impurities in solution due to the increased mass transport towards the electrode surface,[52] as no physical changes of the NPs were observed by AFM before and after ORR measurement. This idea is depicted in Figure 6.15 showing how on a 'clean' Pt surface, at short timescales, the ORR reaction pathway can occur via the four electron mechanism, although there will be some contribution from the two electron transfer mechanism. However on longer timescales where the Pt NPs become

poisoned, the two electron transfer mechanism starts to play a larger role at longer timescales, observed in the electrochemistry.

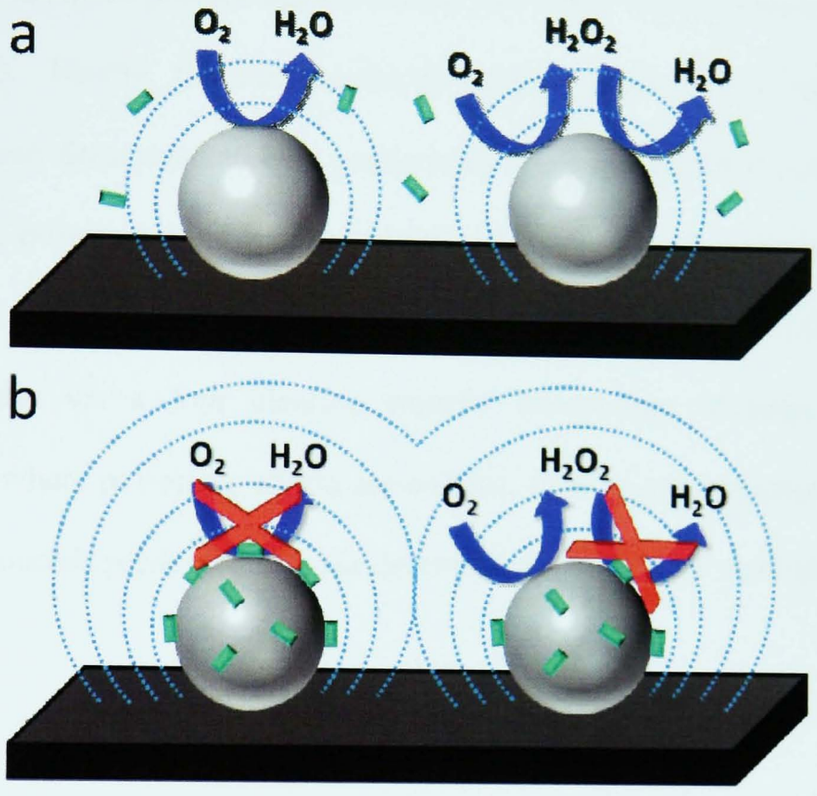

Figure 6.15 A schematic to show the two ORR pathways on Pt NPs electrodeposited onto pBDD where a) shows short time scales and b) shows longer timescales where blocking has become significant

6.5 Conclusions

In this chapter, we have demonstrated the fabrication of a RDE from 'pristine' pBDD (minimal sp^2 carbon content) which has the potential to operate at elevated temperature. The fabricated pBDD-RDE has been tested electrochemically to ensure an ohmic contact and to verify an adequate seal between the electrode and the insulating sheath. Furthermore, unlike many commercially available pBDD-RDEs, the fabricated pBDD-RDE is sufficiently flat to allow AFM measurements to be performed, making it the ideal substrate for nanoparticulate catalytic systems as it allows full quantification of the particle

sizes. Moreover, with the AFM instrument employed in these experiments, the actual RDE can be imaged. In addition, it has been shown that the pBDD-RDE can be readily functionalised with (platinum) nanoparticles which are bound sufficiently strong to prevent agglomeration due to the shear forces involved in a RDE set-up. Finally, the electrocatalytic activity of the Pt NP functionalised RDE has been demonstrated by a preliminary study on the ORR and compared with a bulk polycrystalline platinum RDE. From these measurements we can conclude that on shorter timescales (a 'clean' Pt surface) the ORR occurs predominantly via a four electron transfer mechanism whereas on longer timescales, where poisoning effects are evident, sites become blocked and hence the ORR proceeds predominantly via the two electron transfer mechanism.

6.6 REFERENCES

(1) Litster, S.; McLean, G. *J. Power Sources* **2004**, *130*, 61.

(2) Dyer, C. K. *J. Power Sources* **2002**, *106*, 31.

(3) Wilson, M. S.; Garzon, F. H.; Sickafus, K. E.; Gottesfeld, S. *J. Electrochem. Soc.* **1993**, *140*, 2872.

(4) Darling, R. M.; Meyers, J. P. *J. Electrochem. Soc.* **2003**, *150*, A1523.

(5) Merzougui, B.; Swathirajan, S. *J. Electrochem. Soc.* **2006**, *153*, A2220.

(6) Acharya, C. K.; Turner, C. H. *J. Phys. Chem. B* **2006**, *110*, 17706.

(7) Matter, P. H.; Zhang, L.; Ozkan, U. S. *J. Catal.* **2006**, *239*, 83.

(8) Ferreira-Aparicio, P.; Folgado, M. A.; Daza, L. *J. Power Sources* **2009**, *192*, 57.

(9) Wang, M.-x.; Xu, F.; Sun, H.-f.; Liu, Q.; Artyushkova, K.; Stach, E. A.; Xie, J. *Electrochim. Acta* **2011**, *56*, 2566.

(10) Xu, W.; Zhou, X.; Liu, C.; Xing, W.; Lu, T. *Electrochem. Commun.* **2007**, *9*, 1002.

(11) Ye, F.; Wang, T.; Li, J.; Wang, Y.; Li, J.; Wang, X. *J. Electrochem. Soc.* **2009**, *156*, B981.

(12) Hutton, L.; Newton, M. E.; Unwin, P. R.; Macpherson, J. V. *Anal. Chem.* **2008**, *81*, 1023.

(13) Compton, R. G.; Foord, J. S.; Marken, F. *Electroanalysis* **2003**, *15*, 1349.

(14) Pleskov, Y. V. *Russ. J. Electrochem.* **2002**, *38*, 1275.

(15) Xu, J.; Granger, M. C.; Chen, Q.; Strojek, J. W.; Lister, T. E.; Swain, G. M. *Anal. Chem.* **1997**, *69*, 591A.

(16) Yano, T.; Tryk, D. A.; Hashimoto, K.; Fujishima, A. *J. Electrochem. Soc.* **1998**, *145*, 1870.

(17) Garsany, Y.; Baturina, O. A.; Swider-Lyons, K. E.; Kocha, S. S. *Anal. Chem.* **2010**, *82*, 6321.

(18) van der Vliet, D.; Wang, C.; Debe, M.; Atanasoski, R.; Markovic, N. M.; Stamenkovic, V. R. *Electrochim. Acta* **2011**, *56*, 8695.

(19) Kumar, S. M. S.; Hidyatai, N.; Herrero, J. S.; Irusta, S.; Scott, K. *Int. J. Hydrogen Energy* **2011**, *36*, 5453.

(20) Genorio, B.; Subbaraman, R.; Strmcnik, D.; Tripkovic, D.; Stamenkovic, V. R.; Markovic, N. M. *Angew. Chem.* **2011**, *123*, 5582.

(21) El Roustom, B.; Siné, G.; Fóti, G.; Comninellis, C. *J. Appl. Electrochem.* **2007**, *37*, 1227.

(22) Sarapuu, A.; Helstein, K.; Schiffrin, D. J.; Tammeveski, K. *Electrochem. Solid-State Lett.* **2005**, *8*, E30.

(23) Fischer, A. E.; Lowe, M. A.; Swain, G. M. *J. Electrochem. Soc.* **2007**, *154*, K61.

(24) Ghodbane, S.; Ballutaud, D.; Omnès, F.; Agnès, C. *Diamond Relat. Mater.*, *19*, 630.

(25) Martin, H. B.; Argoitia, A.; Landau, U.; Anderson, A. B.; Angus, J. C. *J. Electrochem. Soc.* **1996**, *143*, L133.

(26) Bennett, J. A.; Wang, J.; Show, Y.; Swain, G. M. *J. Electrochem. Soc.* **2004**, *151*, E306.

(27) Song, C.; Tang, Y.; Zhang, J. L.; Zhang, J.; Wang, H.; Shen, J.; McDermid, S.; Li, J.; Kozak, P. *Electrochim. Acta* **2007**, *52*, 2552.

(28) Yang, C.; Costamagna, P.; Srinivasan, S.; Benziger, J.; Bocarsly, A. B. *J. Power Sources* **2001**, *103*, 1.

(29) *http://www.vp-scientific.com/Chemical_Resistance_Chart.htm Accessed 21-09-11 at 16.15.*

(30) Mayrhofer, K. J. J.; Hanzlik, M.; Arenz, M. *Electrochim. Acta* **2009**, *54*, 5018.

(31) Min, M.-k.; Cho, J.; Cho, K.; Kim, H. *Electrochim. Acta* **2000**, *45*, 4211.

(32) Mukerjee, S.; Srinivasan, S.; Soriaga, M. P.; McBreen, J. *J. Electrochem. Soc.* **1995**, *142*, 1409.

(33) Pletcher, D.; Sotiropoulos, S. *J. Electroanal. Chem.* **1993**, *356*, 109.

(34) Marković, N. M.; Schmidt, T. J.; Stamenković, V.; Ross, P. N. *Fuel Cells* **2001**, *1*, 105.

(35) Wroblowa, H. S.; Yen Chi, P.; Razumney, G. *Journal of Electroanalytical Chemistry and Interfacial Electrochemistry* **1976**, *69*, 195.

(36) Fischer, P.; Heitbaum, J. *Journal of Electroanalytical Chemistry and Interfacial Electrochemistry* **1980**, *112*, 231.

(37) Collier, A.; Wang, H.; Zi Yuan, X.; Zhang, J.; Wilkinson, D. P. *Int. J. Hydrogen Energy* **2006**, *31*, 1838.

(38) Maillard, F.; Bonnefont, A.; Micoud, F. *Electrochem. Commun.* **2011**, *13*, 1109.

(39) Stappers, L.; Fransaer, J. *J. Electrochem. Soc.* **2005**, *152*, C392.

(40) Cherstiouk, O. V.; Simonov, P. A.; Savinova, E. R. *Electrochim. Acta* **2003**, *48*, 3851.

(41) Maillard, F.; Schreier, S.; Hanzlik, M.; Savinova, E. R.; Weinkauf, S.; Stimming, U. *Phys. Chem. Chem. Phys.* **2005**, *7*, 385.

(42) Kamau, G. N.; Willis, W. S.; Rusling, J. F. *Anal. Chem.* **1985**, *57*, 545.

(43) Strbac, S. *Electrochim. Acta* **2011**, *56*, 1597.

(44) St-Pierre, J. *J. Power Sources* **2010**, *195*, 6379.

(45) Markovic, N. M.; Ross, P. N. *Surf. Sci. Rep.* **2002**, *45*, 117.

(46) Sayed, S. M.; Jüttner, K. *Electrochim. Acta* **1983**, *28*, 1635.

(47) Herrero, E.; Mostany, J.; Feliu, J. M.; Lipkowski, J. *J. Electroanal. Chem.* **2002**, *534*, 79.

(48) Awad, M. I.; Saleh, M. M.; Ohsaka, T. *J. Power Sources* **2011**, *196*, 3722.

(49) Sarapuu, A.; Kasikov, A.; Laaksonen, T.; Kontturi, K.; Tammeveski, K. *Electrochim. Acta* **2008**, *53*, 5873.

(50) Seidel, Y. E.; Schneider, A.; Jusys, Z.; Wickman, B.; Kasemo, B.; Behm, R. J. *Faraday Discuss.* **2009**, *140*, 167.

(51) Schmidt, T. J.; Paulus, U. A.; Gasteiger, H. A.; Behm, R. J. *J. Electroanal. Chem.* **2001**, *508*, 41.

(52) Mo, Y.; Sarangapani, S.; Le, A.; Scherson, D. A. *J. Electroanal. Chem.* **2002**, *538-539*, 35.

CHAPTER 7

CONCLUSIONS

The improvement of fuel cell (FC) technology requires continual research, particularly concerning the electrocatalyst and support material which are paramount in determining the overall durability and efficiency of the cell. The aim of this thesis was to provide insight into electrocatalysis at composite materials and also explore alternative electrocatalyst support materials.

Bare highly oriented pyrolytic graphite (HOPG) and poly-(3,4-ethylenedioxythiophene) (PEDOT) coated HOPG were employed as support materials for the electrodeposition of Pt nanoparticles (NPs). The formation of these NPs on the two substrates were characterised by employing tapping mode – atomic force microscopy (TM-AFM) and Pt oxide stripping voltammetry. For similarly prepared Pt NPs electrodeposited onto the two substrates, NPs on PEDOT coated HOPG showed no preferential deposition at step edges and a high density of smaller nanoparticles was observed. Methanol oxidation and formic acid oxidation were two electrocatalytic processes investigated. When PEDOT was employed as the electrocatalyst support material, a higher rate by a factor of ten was recorded for methanol oxidation. Similarly, formic acid oxidation was enhanced at higher potentials. We attribute these findings to an enhanced rate of oxidation of adsorbed CO in the presence of PEDOT. To fully elucidate reasons for the increased rate, further investigation which focuses on the intermediates

formed is required. This could involve techniques such as *in-situ* mass spectrometry.

The investigation of an alternative electrocatalyst support, polycrystalline boron doped diamond (pBDD), a main focus of this thesis. Prior to being used as a catalyst support, new fundamental information about this substrate was obtained. pBBD is known to be an excellent electrode material owing to the many advantageous properties compared with other materials. During the growth process, boron uptake varies across the sample mainly due to the crystallographic plane, leading to a heterogeneous surface. pBDD is usually employed as a macro electrode where the current response would arise from the surface as a whole, however, in reality, this substrate consists of many areas with varied boron concentration and, in principle, a range of electron transfer rates could occur. If the properties of the material were well understood then it would be possible to re-engineer it to optimise performance. Two new electrochemical imaging techniques, intermittent contact - scanning electrochemical microscopy (IC-SECM) and scanning electrochemical cell microscopy (SECCM) were used to probe the surface reactivity.

IC-SECM was employed in Chapter 4. Electrochemical images revealed heterogeneities on the sample and also proved that the entire surface of the pBDD was active. Raman spectroscopy and field emission – scanning electron microscopy (FE-SEM) were two methods employed to determine the levels of boron and surface conductivity. Micro-Raman maps and SEM images were directly compared with the IC-SECM images which revealed a very good correlation between boron dopant levels and activity. Furthermore, the Raman

spectroscopy for all areas of the pBDD proved that the boron dopant level was > 1 x 10^{20} atoms cm^{-3}, indicated by the presence of a Fano resonance. Using simulations, the standard rate constant, k^0, was determined for the oxidation of $FcTMA^+$ and the reduction of $Ru(NH_3)_6^{3+}$. A particularly interesting result revealed that as the concentration of mediator was increased for the reduction of $Ru(NH_3)_6^{3+}$, the highly doped grains possessed metallic-like behaviour, however, the lower doped regions showed a charge carrier depletion effect. We propose that the conductivity at the lower doped regions occurs via a hopping mechanism previously reported to occur at a boron concentration of 1 x 10^{19} cm^{-3} to 3 x 10^{20} cm^{-3}. A comparison between the oxidation of 1 mM $FcTMA^+$ and 1mM $Ru(NH_3)_6^{3+}$ at the highly doped regions suggest fifty times slower electron transfer kinetics however this value can be related to differences in the self exchange rate constant, k_{exc}.

SECCM also revealed that the entire surface of boron doped diamond was active with no evidence of increased activity at grain boundaries. In some cases, current maps for simple outer sphere redox mediators were converted to k^0. In other cases, a semi-quantitative comparison was made by analysis of current maps. A depletion of charge carriers for the regions of lower boron content was found as the bulk concentration of $Ru(NH_3)_6^{3+}$ was increased from 5 mM to 10 mM. A major advantage of SECCM over conventional imaging methods is the ability to probe a new area of sample with fresh solution at every point forming the image. This was clearly demonstrated using a 'complex' inner sphere electron transfer mediator, serotonin. Imaging revealed the heterogeneous structure of the pBDD electrode. However when a second image for the oxidation of serotonin was collected over the same region, a conducting film or

porous membrane was evident, with no indication of the underlying pBDD grain structure.

The final results chapter in this thesis has been concerned with the fabrication of a pBDD rotating disk electrode (RDE). This was successfully characterised using two redox mediators. To investigate the oxygen reduction reaction (ORR) (which occurs at the cathode in FC), the pBDD RDE was functionalised with Pt NPs via electrodeposition. The response from pBDD was compared to a bulk Pt RDE in sulphuric acid and perchloric acid. From these experiments we conclude that, at short timescales, the ORR occurs predominantly via the four electron transfer process, forming water as the product, however, on longer timescales the two electron transfer mechanism dominates, forming hydrogen peroxide. In future work it would be interesting to use the RDE to elucidate ORR electron transfer kinetics.